Predicting Atmospheric Icing and its Impact on Overhead Contact Wires

A CFD Study and a Proposed Method of Predicting Ice Accretion

Axel Flygare & Linus Ferngren

LUND UNIVERSITY

LTH FACULTY OF ENGINEERING

TRAFIKVERKET SWEDISH TRANSPORT ADMINISTRATION

This thesis was carried out during the spring of 2026 at the Department of Energy Sciences, Lund University. The work was carried out in collaboration with the Swedish Transport Administration, Trafikverket.

University Supervisor: Johan Revstedt
Supervisor at Trafikverket: Hanna Närhi
University Examiner: Marcus Thern

MSc Thesis
ISRN LUTMDN/TMHP-26/5676-SE
ISSN 0282-1990
Ärendenummer UHte 26-029

Department of Energy Sciences
Factulty of Engineering
Lund University
223 63 LUND
Sweden

Acknowledgements

We would like to thank our supervisors Johan Revstedt at Lund University (LTH) department of Fluid Mechanics and Hanna Närhi at Trafikverket for contious guidance througout the entire process of this thesis. We would also like to thank Robert-Zoltán Szász at the LTH department of Fluid Mechanics and Lei Wang at the LTH department Heat Transfer for lending us key knowledge and equipment throughout the duration of our project, especially for our experimental work.

We would also like to thank Ahmet Devlet Özçelik and Arman Ahamed Subash at the LTH School of Aviation for letting us use their wind tunnel in Ljungbyhed as well as helping us to set up the experiments and providing necessary tools.

Axel Flygare & Linus Ferngren

Abstract

Ice accretion on overhead contact lines poses a significant challenge in the dimensioning of the railway system. The accreted ice will impose an additional vertical load from its self-weight and affect the wind loads by changing the wires cross-sectional area and shape. The current dimensioning methods, used by Trafikverket, often rely on simplified approximations and constant values when calculating the effects of wind and ice loads. While the approach has not led to any known issues, more accurate calculations are desired to not needlessly overdimension the system.

This thesis aims to, with the use of Computational Fluid Dynamics (CFD), evaluate the current way of calculating ice and wind loads. This is done by simulating in-cloud icing, more specifically rime ice, in the software *ANSYS FENSAP-ICE* followed by flow simulations in *ANSYS FLUENT* for the drag coefficients.

A parametric study during the ice accretion simulations showed how different meteorological parameters will have a slight effect on the final ice shape. Thereafter the fluid simulations in *FLUENT* were conducted using both Unsteady Reynolds-Averaged Navier-Stokes (URANS) and Large Eddy Simulation (LES) to determine the drag coefficients for both non-iced and iced contact wires. The results were validated against experimental wind tunnel testing.

The results showed how the drag coefficients of the iced contact wires have a dependency on the meteorological parameters under which the ice was accreted. Additionally the flow simulations showed how the current assumptions, for both the clean and iced contact wire, may underestimate wind loads due to an underestimation of the drag coefficient. Furthurmore, the fluid simulations showed a strong dependency of the simulation setup, especially with regards to the chosen turbulence model, where LES provided substantially better force predictions.

From the gathered ice geometries and drag coefficients, as well as empirical formulas and correlations, a dynamic ice accretion model is presented. While the model contains rough approximations for geometric shapes and meteorological conditions, it demonstrates the benefit of using a dynamic model, as opposed to the today's static assumptions, during dimensioning of the overhead contact line system.

Contents

Nomenclature

Latin letters	Description	Unit
A	Cross section area	m^2
C_C	Drag factor	–
C_d	Drag coefficient	–
D	Diameter	m
E_s	Saturation vapor pressure	Pa
F_d	Drag force	N
G_C	Structural response factor	–
K	Droplet inertia parameter	–
L	Characteristic length	m
M_a	Molar mass of dry air	$kg\,mol^{-1}$
M_w	Molar mass of water vapor	$kg\,mol^{-1}$
N	Number of time steps	–
Q	Load	N
R	Universal Gas constant	$J\,mol^{-1}\,K^{-1}$
R_a	Arithmetic average of absolute values	m
R_{RMS}	Root mean square values	m
R_{zd}	Peak-to-Valley values	m
Re	Reynolds number	–
Re_d	Droplet Reynolds number	–
S	Sutherland's constant	K
St	Strouhal number	–
T	Absolute temperature	K
T_s	Surface Temperature	K
U_∞	Free stream velocity	$m\,s^{-1}$
V	Specific volume	m^3
c	Chord length	m
d	Diameter	m
d_m	Median volume droplet diameter	µm
f	Frequency	Hz
n	Amount of substance	mol
m	Specific characteristic ice load	$kg\,m^{-1}$
p	Pressure	Pa
P	Absolute pressure	Pa
p_w	Partial pressure of water vapor	Pa

p_{sat}	Saturation vapor pressure	Pa
q_p	Peak velocity pressure	$\mathrm{N\,m^{-2}}$
t	Glaze ice thickness	mm
v	Particle velocity	$\mathrm{m\,s^{-1}}$
v_0	Droplet impact velocity	$\mathrm{m\,s^{-1}}$
w	Mass concentration of particles in the air	$\mathrm{g\,m^{-3}}$
k_s	Sand-grain roughness height	m
k_0	Partial factor	–

Greek letters	**Description**	**Unit**
α_1	Collision efficiency	–
α_2	Striking efficiency	–
α_3	Freezing fraction	–
Δt	Time-step size	s
ϵ	Sand-grain diameter	m
ϕ	Relative humidity	–
Φ	Angle of incidence of the wind direction	–
Ψ_0	Probability reduction factor	–
μ	Dynamic viscosity	Pa s
ρ	Density	$\mathrm{kg\,m^{-3}}$

Abbreviation	**Description**
AoA	Angle of Attack
CFD	Computational Fluid Dynamics
CE	Collision Efficiency
DNS	Direct Numerical Simulation
EN	European Standard
FEM	Finite Element Method
FVM	Finite Volume Method
IC	Ice Class
ICG	Ice Class for Glaze
ICR	Ice Class for Rime
ISO	International Organization for Standardization
LES	Large Eddy Simulation
LWC	Liquid Water Content
MVD	Median Volume Diameter
OCL	Overhead Contact Line
OCS	Overhead Contact System
OLE	Overhead Line Equipment
PDE	Partial Differantial Equation
RANS	Reynolds-Averaged Navier-Stokes
SGS	Sub-Grid-Scale
SS	Swedish Standard
SST	Shear Stress Transport

TC	Terrain Category
URANS	Unsteady Reynolds-Averaged Navier-Stokes

English	**Svenska**
Cantilever	Utliggare
Catenary wire	Bärlina
Contact wire	Kontakttråd
Dropper	Bärtråd
Glaze ice	Glattis
Ice class	Isklass
Indentification grooves	Indentifikationsspår
Mast	Stolpe
Overhead contact line	Kontaktledning
Pantograph	Pantograf/Strömavtagare
Railway track	Järnvägsspår
Rime ice	Rimfrost
Swedish Transport Administration	Trafikverket
Swedish Transport Agency	Transportstyrelsen

1

Introduction

Transport by railway has been of key importance for societal development since its introduction in the early 19th century. Since the start of railway electrification in the later half of the 19th century, leading up to modern times it has also proven to be an energy efficient and generally non-polluting mode of passenger and freight traffic.

Looking forward, railway transport can be connected to multiple of the sustainable development goals. Partly because it can be one of the methods to shift transportation from fossil to renewable sources. But also because of its democratization of transport, where cost is generally lower than motoring, and where it has a central role in an expansion of public transport.

The *Overhead Contact System* (OCS) also known as the *Overhead Line Equipment* (OLE) or more generally the *Overhead Contact Lines* (OCL) is the system that is used to deliver electric power to trains, whether they are in transit or standing still, by physical contact between the systems contact wire and the on-roof power collection system, most commonly known as the pantograph [17].

As with all objects exposed to weather, the OCL will be subjected to wind loads. And in countries with a colder climate, the OCL will also be subjected to ice and snow formation. An extreme case of ice accretion can be seen in figure 1.1, which depicts a transmission line in a Norwegian alpine environment. These ice formations can be attributed to a couple of different phenomena but is usually grouped under the same term, atmospheric icing. Atmospheric icing includes the phenomena that occurs when supercooled water droplets, falling or drifting from eg. rain, drizzle or wet snow, in the air come into contact with a surface and freeze upon impact [39] [28]. Depending on the meteorological icing conditions the ice properties may however vary. Nevertheless, Lui et al. [20] explains that at least three conditions needs to be met for the ice to start growing. Firstly, the ambient and surface temperature has to be below 0 $^{\circ}C$. Secondly, the relative humidity has to be above 85 % and thirdly the wind velocity has to exceed at least 1 m/s. Additionally, it has also been found that the rate of ice accretion will be the most severe when an object is placed perpendicular to the wind direction and has a small cross-sectional shape [39].

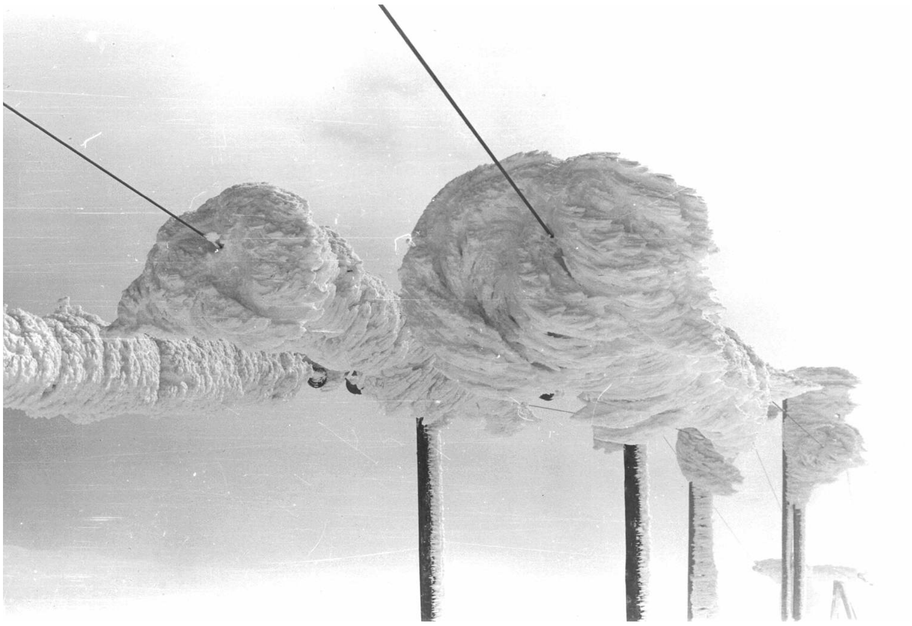

Figure 1.1 Extreme Icing on Power Lines on Lønahorgi. Photo: Olav Wist, Tron Horn AS, April 1961

Ice accretion will increase forces acting on the wire and the supporting masts, due to the added self-weight of the ice, the increase in wire diameter and the change in aerodynamic shape. Additionally, as the cross-sectional shape of the wire changes due to the accreted ice some dynamic properties may change as well. In the case of ice accretion on a wire, the new forces and natural frequency may cause problematic oscillations, also called galloping, due to aerodynamic instabilities [39]. For the sake of safety, reliability and economical reasons it is therefore necessary for the railway planers and constructors, like the Swedish Transport Administration (Trafikverket) to understand these forces and behaviors.

In today's railway system catastrophic failures caused by combined wind and ice loads are extremely rare, but as the OLE is constructed based on tacit knowledge and empirical approximations. Thus, there exists an interest to better understand the system as they could unwittingly be over dimensioned. In addition to older in-house standards the dimensioning of the Swedish railway today uses relevant national and international standards like the *Swedish Standard* (SS), *European Standard* (EN) and *International Organization for Standardization* (ISO).

While some studies exists on the topic of using Computational Fluid Dynamics (CFD) to predict ice accretion and its effect on conductors and contact wires there is still a need for further studies. For example, Liu et al. [20], Xu et al. [45] and Lotfi et al. [21] all studied the ice accretion phenomenon for varying meteorological parameters. Chen et al. [7] studied the galloping effects of a contact wire for a predetermined iced profile. Zhang et al. [46] conducted a similar study where the aerodynamic performance of two iced contact wires was evaluated. Where the ice shapes was defined from measurements of real ice accretions. Zhang additionally studied how the galloping effect behaved with the iced geometries by using both CFD and wind tunnel experiments.

This masters thesis aims to, with the use of Computational Fluid Dynamics and experimental verification, evaluate the current proceedings at Trafikverket for the calculations of combined wind and ice loads in the case of contact wires. Additionally the study aims to evaluate how CFD can be used as an additional tool to assist relevant national and international standards. More specifically, the aim is to evaluate how the icing of contact wires occur under different atmospheric conditions, and how it changes the aerodynamic shape and properties of the wire. The aim is then to use the results, and examine how the forces on contact wires can differ geographically across Sweden.

To accomplish the studies, the commercially available softwares *ANSYS FLUENT* and *ANSYS FENSAP-ICE* will be used. *ANSYS FLUENT* will be the software used for the aerodynamic calculations as Martini et al. [27] found in a comparison of experimental and numerical studies that *FLUENT* was more precise in estimating aerodynamic parameters than the flow solver module *FENSAP* in the *FENSAP-ICE* package. The software *FENSAP-ICE* was initially developed for the aeronautics industry to simulate in-flight aircraft icing [27]. This differs from ground level icing which is present in applications like wind turbines or electrical conductors due to the different weather conditions that are experienced. Fu et al. [10] confirmed this and developed a new 2-D icing model for overhead power line cables. With this said, the *FENSAP-ICE* software is still one of the most commonly used programs to predict ice accretion even at ground level, as is the case for contact wires, and will therefore be used in this study.

Lastly, this study aims to propose an ice accreton prediction model based on the CFD results, empirical formulas and measured data. The model aims to predict how ice accretion and the resulting forces can vary over time for a limited set of forecasted parameters.

2

Theory

2.1 Overhead Contact Lines

The OCL system, simplified, consists of supporting masts, cantilevers, catenary wires, droppers and contact wires. The supporting masts are placed in the ground with sufficient spacing to hold up the system and transfer the resulting forces and moments to the ground. On top of the masts, cantilevers are mounted to hold the catenary and contact wire over the railway track in a zig-zag pattern and at the desired height. Along the catenary, droppers (vertical wires) are placed vertically down to hold the contact wire at the desired height and tension i between cantilevers as can be seen in figure 2.1.

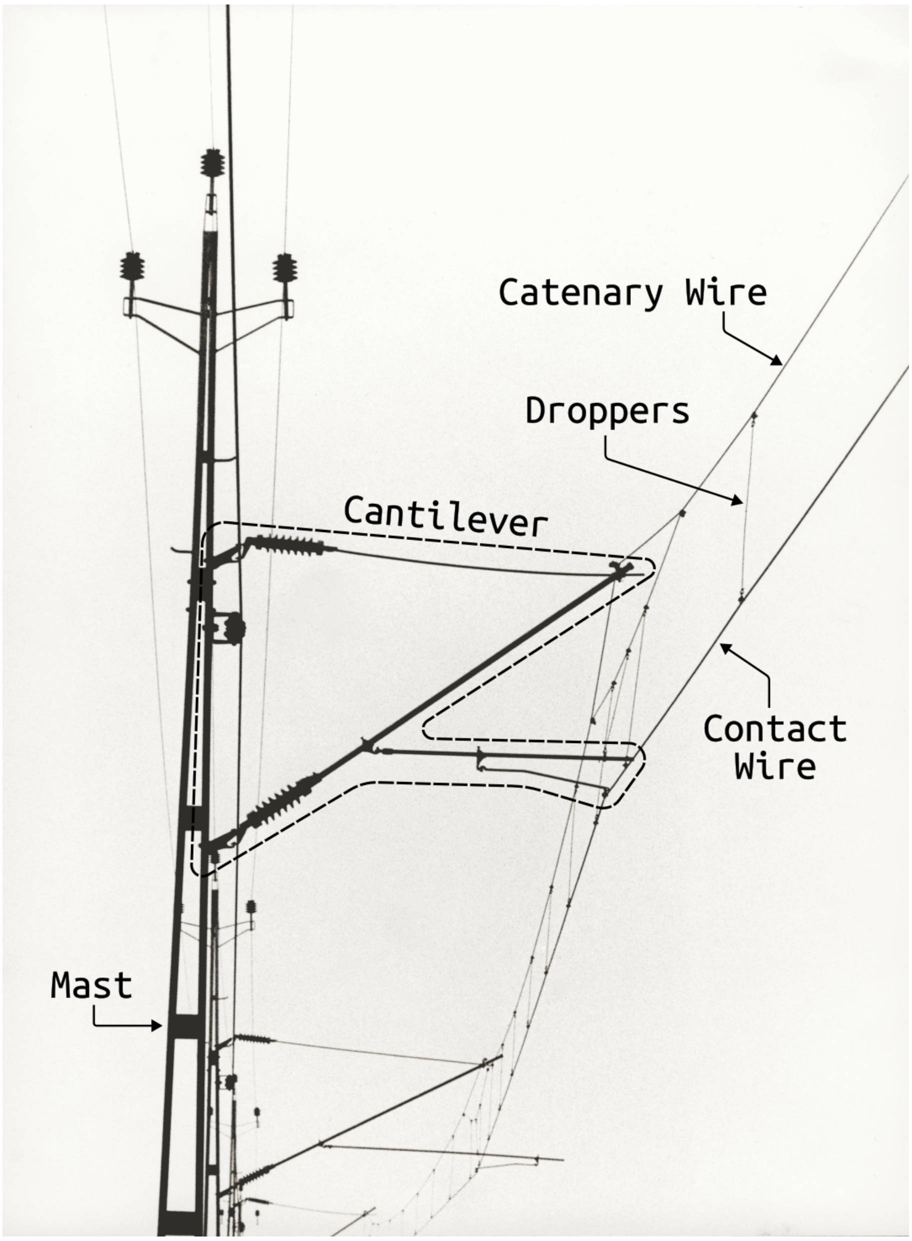

Figure 2.1 Overhead Contact Line. Photo: Kjell Andersson, Swedish Railway Museum (archives) / SMMTF

The electric power in the OCL is transferred to the trains through physical contact between the train's pantograph, and the contact wire. For the droppers to grip onto the contact wire without disrupting the physical connection or destroying the pantograph's carbon strip, the geometry of the wire needs clamping grooves [17]. A typical cross-section of a contact wire, with the characteristic clamping grooves can be seen in figure 2.2.

While the general cross-sectional shape of the contact wire remains constant, the size, bottom shape, clamping grooves and material alloy (together with identification grooves) may vary.

All variations of the contact wire can be found in the Swedish Standard SS-EN 50149

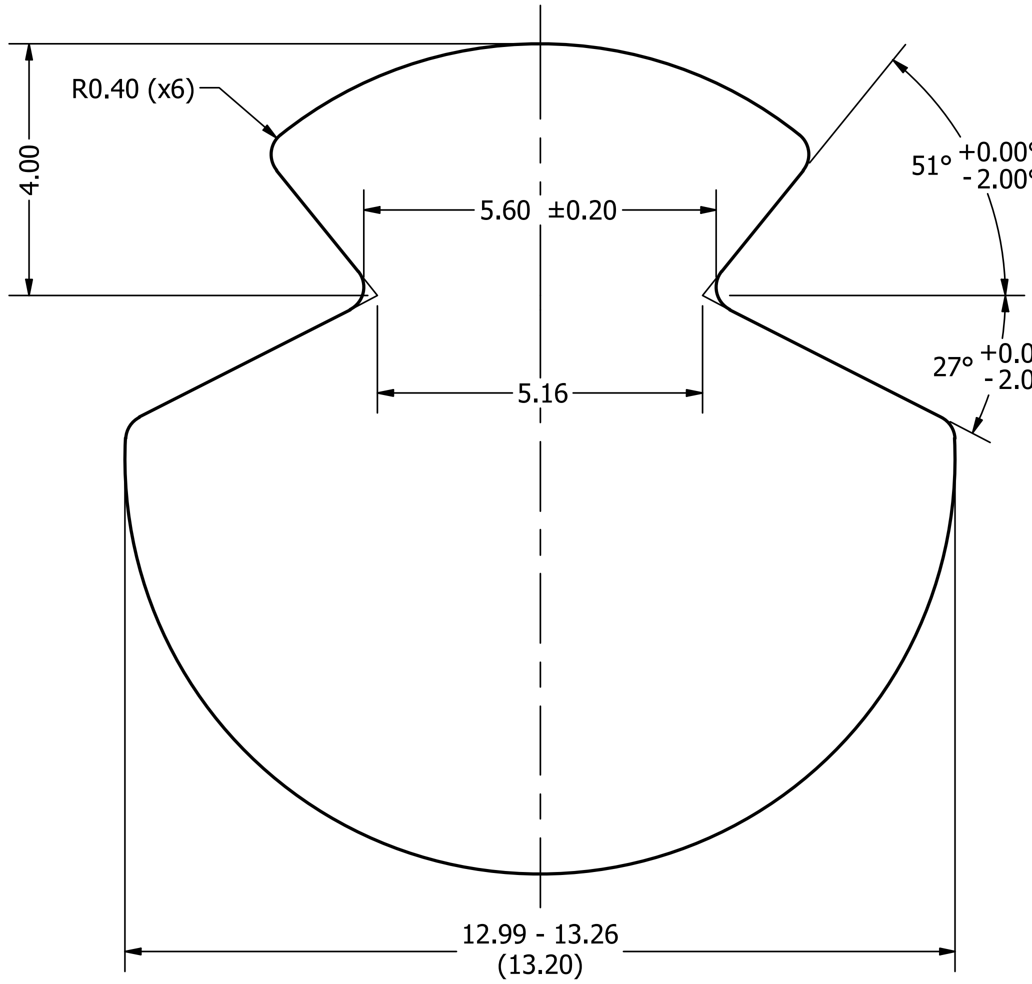

Figure 2.2 Contact Wire type AC-120 CuETP Drawing [32]

[32]. But in short, the size is of the contact wire is denoted by the nominal cross-sectional area and exists in the sizes: 80, 100, 107, 120 and 150 mm^2. The bottom can take the form as completely circular or with a more flattened bottom. The clamping grooves are divided into two categories, A and B, which vary by angles and depth. The material may vary between pure, high strength copper (eg. CuETP), a copper-silver alloy (CuAg0.1) or a copper-magnesium alloy (eg. CuMg0.5) among others. To ensure that all wires are manufactured with easily identifiable alloys, identification grooves are placed on top of the wire where the number of grooves and their placement is unique for each alloy.

For this study, a contact wire with the denotation *AC-120 CuETP* as seen in figure 2.2 will be used, which indicates that the cross-sectional area is 120 mm^2, with a circular bottom (C), clamping grooves of variation "A", a material of high strength copper and with no identification grooves in accordance with the norm for pure copper wires. The aforementioned type of wire is commonly used for high speed trains which do not allow for the wire to sag, and thereby have strict mechanical requirements. This is why the understanding of wind and ice loads are especially important and why the *AC-120 CuETP* was chosen for this study.

Contact wires used by Trafikverket is furthermore engraved with the text "TRAFIKVERKET" as well as the manufacturing date on the top of the wire. While these indents may slightly alter the flow around the wire they are assumed to be negligible and will be left out of this study.

Finally, as a result of the physical contact between the pantograph and contact wire the underside of the wire will eventually get worn down. As the contact wire is worn down by abrasive forces the wider the contact area gets, and the rate of which the wire is worn down decreases. When the contact wire is worn down to a minimum specified height it is replaced. As a delimitation in this study the effect of wear and tear will not be considered.

2.2 Current Proceedings

In today's proceedings at Trafikverket, the work of calculating forces from contact wires are simplified by using a perfect cylinder as approximating of the contact wire, as presented in section 2.1. With this approximation the ice and wind loads are initially calculated separately. The resulting ice and wind loads are then added together after each load gets a partial factors and a probability factors (since maximal wind and ice load is statistically unlikely to overlap). The dimensioning case is hence determined by equation (2.1) or (2.2), whichever is larger. The ingoing loads Q_{wind} and Q_{ice} and how they are calculated will be covered later in this section.

$$Q_{tot} = k_{0,wind} \cdot Q_{wind} + k_{0,ice} \cdot \Psi_{0,ice} \cdot Q_{ice} \tag{2.1}$$

$$Q_{tot} = k_{0,wind} \cdot \Psi_{0,wind} \cdot Q_{wind} + k_{0,ice} \cdot Q_{ice} \tag{2.2}$$

where

Q_{tot} is the total resulting load [N]

Q_{wind} is the wind load [N]

Q_{ice} is the ice self load [N]

and

Ψ_0 is the probability factor, $\Psi_0 = \begin{cases} 0.3 & \text{(wind)} \\ 0.5 & \text{(ice)} \end{cases}$ [-]

k_0 is the partial factor, $k_0 = \begin{cases} 1.5 & \text{(wind)} \\ 1.5 & \text{(ice)} \end{cases}$ [-]

To determine the wind speeds and amount of ice accretion that should be considered in the design stages of the railway system, Trafikverket, as recommended by the Swedish standard [39] , uses a 50-year return period for both the maximal wind speed and ice accretion. This corresponds to an annual exceedance probability of 0.02.

Finally, in the current Swedish norm that Trafikverket follows, it is stated that only glaze ice (see section 2.7 for more information) needs to be considered together with the standard SS-EN 50119 and the other relevant eurocodes from the EN 1990-series. Consequently, the calculations explained in the theory, method and result sections regarding rime ice, are not applied today by Trafikverket.

Ice Loads

The ice loads, given by the ice weight, can be approximated in two ways. The older and current way, which is found in the Swedish standard SS-EN 50125-2 [31], is carried out by dividing geographical locations into four different Ice Classes (IC) and giving each one a dimensioning load as can be seen in table 2.1.

Table 2.1 Ice loads from SS-EN 50125-2 [31]

Class	**Iceload** N/m
I 0 (no ice)	0
I 1 (low)	3,5
I 2 (medium)	7
I 3 (heavy)	15

Today, ice class 1 (low) is used for all contact wires while other OCL conductors are assumed to be of ice class 3 (heavy). Geographical segmentation of the ice class within Sweden, depending on meteorological variations, are subsequently not implemented as of today.

A newer way of approximating the ice load was put forth in new Eurocode SS-EN 1991-1-9:2025[1] [40] where the load is dependent on the type of ice, *rime* or *glaze* (more on this in section 2.7), and a specified ice class. The Swedish standard SS-ISO 12494-2017 [39] specifies that the ice class is to be defined as the "characteristic value" (depends on ice type) of ice accretion on a reference collector for a 50 year return period. Then the IC can be determined either by using meteorological and topographical data with a ice accretion model or by in-situ measuring of the ice mass.

For glaze ice, the standard SS-EN 1991-1-9:2025 [40] describes how the ice thickness is approximated for an object of different Ice Classes of Glaze (ICGs) at 10 meters above ground level, as shown in table 2.2.

[1] The new Eurocode is part of the second generation Eurocodes. Because of the new addition the Swedish Transport Agency (Transportstyrelsen) has not yet advised how the new standards should be used by Trafikverket. Despite this it can still be used for guidance

Table 2.2 Ice Thicknesses for ICGs [40] [2]

Ice classes for glaze (ICG)	**G1**	**G2**	**G3**	**G4**	**G5**	**G6**
Characteristic ice thickness t (mm)	10	20	30	40	50	[a]

[a] To be used for extreme ice accretions.

With the characteristic ice thickness, the ice mass per meter cable can then be calculated by equation 2.3 [2] [40]

$$m = \pi \cdot \rho \cdot t(d + t) \tag{2.3}$$

where

t is the glaze ice thickness

d is the cylinder diameter

ρ is the glaze density, $\rho = 900$ kg/m^3

For rime ice, SS-EN 1991-1-9:2025 [40] instead gives a characteristic ice mass values per meter cable, similar to table 2.1, but for different Ice Classes of Rime (ICRs) at 10 meter above ground level. See table 2.3

Table 2.3 Ice masses for ICRs [40] [2]

Ice classes for rime	**R1**	**R2**	**R3**	**R4**	**R5**	**R6**	**R7**	**R8**	**R9**	**R10**
Characteristic Ice mass m (kg/m)	0,5	0,9	1,6	2,8	5,0	8,9	16,0	28,0	50,0	[a]

[a] To be used for extreme ice accretions.

Wind Loads

To calculate the wind load on a supporting mast, SS-EN 50119 [33] present equation (2.4).

$$Q_{WC} = q_p(z) \cdot G_C \cdot d \cdot C_C \cdot \frac{L_1 + L_2}{2} \cdot \cos^2 \Phi \quad [\mathrm{N}] \tag{2.4}$$

where

Q_{WC} is the wind load from two adjacent conductors spans on the supporting mast [N]

[2] The table/equation is reproduced from SS-EN 1991-1-9:2025/ SS-ISO 12494:2017 / SS:EN 1991-1-4:2005 with due permission from SIS, Swedish Institute for Standards who also offers the complete standard for purchase. Copyright SIS. www.sis.se

$q_p(z)$ is the peak velocity pressure at a height z [N/m^2]

G_C is the structural response factor. A widely accepted value would be $G_C = 0.75$ [-]

d is the diameter of the conductor [m]

C_C is the drag factor of the conductor. A value of 1.0 is recommended [3]

L_1, L_2 are the wire spans of the two adjacent sections [m]

Φ is the angle of incidence of the critical wind direction. In general its assumed to be zero [degrees]

The peak velocity pressure $q_p(z)$ is given by a tabulated value in *Transportstyrelsens* guidelines TSFS 2018:57 [43] where it depends on the height above ground level, maximum wind velocity for a 50 year return period and a Terrain Category (TC) which is defined by SS:EN 1991-1-4:2005 [41], see table 2.4.

Table 2.4 Terrain categories and terrain parameters [41] [4]

	Terrain category	z_0 m	z_{min} m
0	Sea or coastal area exposed to the open sea	0,003	1
I	Lakes or flat and horizontal area with negligible vegetation and without obstacles	0,01	1
II	Area with low vegetation such as grass and isolated obstacles (trees, buildings) with separations of at least 20 obstacle heights	0,05	2
III	Area with regular cover of vegetation or buildings or with isolated obstacles with separations of maximum 20 obstacle heights (such as villages, suburban terrain, permanent forest)	0,3	5
IV	Area in which at least 15 % of the surface is covered with buildings and their average height exceeds 15 m	1,0	10

NOTE: The terrain categories are illustrated in A.1 in [41].

An important note, which is mentioned in the standards SS-EN 1991-1-4:2005 [41] and SS-ISO 12494:2017 [39] is that if the accreted ice changes the geometry of the object in a way that alters the reference area and shape, then these changes shall be taken into account as the wind drag might increase.

[3] The standard SS-EN 50119 recommends the value of 1.0 while the standard SS-EN 1991-1-4:2005 recommends a value of $1.2 \cdot \Psi_\lambda$ where Ψ_λ is the end-effect factor. This correlates better with the usually accepted drag coefficient value for a cylinder as presented by Lienhard [19]. This is also confirmed by Anderson [2]

[4] The table/equation is reproduced from SS-EN 1991-1-9:2025/ SS-ISO 12494:2017 / SS:EN 1991-1-4:2005 with due permission from SIS, Swedish Institute for Standards who also offers the complete standard for purchase. Copyright SIS. www.sis.se

Diameter correction. To account for the increase in conductor diameter for a certain ice class, SS-EN 1991-1-9:2025 [40] [5] suggests using equation (2.5) to find the new diameter perpendicular to the wind direction.

$$D = \sqrt{d^2 + \frac{4 \cdot m}{\pi \cdot \rho_{ice}}} \tag{2.5}$$

where

D is the total width of the object including ice [m]

d is the conductor diameter without ice measured in meters [m]

m is the specific characteristic ice load measured, taken from Table 2.3 [kg/m]

ρ_{ice} is the ice density [kg/m^3]

To account for the diameter increase with glaze ice two different methods can be used:

With the current procedure, the diameter is approximated though calculations by using table 2.1 with the assumption that the ice thickness is constant around the wire. Then with an ice density assumption of $\rho_{ice} = 900 kg/m^3$ the final diameter is calculated.

In the newer presented method, from the standard SS-EN 1991-1-9-2025, the new diameter when glaze ice is present will be two ice thicknesses, taken from table 2.2, added to the original diameter of the wire.

Drag coefficient correction. The change in shape of the contact wire, with regards to the aerodynamic flow, is something Trafikverket does not consider in their current calculations. However, the Swedish standard SS-ISO 12494:2017 [39] presents tables for how the drag coefficient (C_d) should be altered depending on whether glaze or rime ice is considered. Table 2.5 shows how the coefficient should be changed, dependent on the originally assumed value for glaze ice. In table 2.5 & 2.6 C_i is the equivalent of C_C in equation 2.4 and the otherwise used C_d.

Table 2.5 C_i coefficients for glaze on bars [39][5]

Ice class (IC)	**Ice thickness [mm]**	C_i coefficients for glaze on bars						
		Drag coefficients without ice, C_0						
		0,50	0,75	1,00	1,25	1,50	1,75	2,00
G1	10	0,68	0,88	1,08	1,28	1,48	1,68	1,88
G2	20	0,86	1,01	1,16	1,31	1,46	1,61	1,76
G3	30	1,04	1,14	1,24	1,34	1,44	1,54	1,64
G4	40	1,22	1,27	1,32	1,37	1,42	1,47	1,52
G5	50	1,40	1,40	1,40	1,40	1,40	1,40	1,40
G6	To be used for extreme ice accretions							

In a similar fashion SS-ISO 12494:2017 [39] presents a table for when rime ice is considered, see table 2.6.

Table 2.6 C_i coefficients for rime on bars [39][6]

IC	Ice mass m kg/m	C_i coefficients for rime on bars						
		Drag coefficient without ice, C_0						
		0,50	0,75	1,00	1,25	1,50	1,75	2,00
R1	0,5	0,62	0,84	1,07	1,29	1,51	1,73	1,96
R2	0,9	0,74	0,94	1,13	1,33	1,52	1,72	1,91
R3	1,6	0,87	1,03	1,20	1,37	1,53	1,70	1,87
R4	2,8	0,99	1,13	1,27	1,41	1,54	1,68	1,82
R5	5,0	1,11	1,22	1,33	1,44	1,56	1,67	1,78
R6	8,9	1,23	1,32	1,40	1,48	1,57	1,65	1,73
R7	16,0	1,36	1,41	1,47	1,52	1,58	1,63	1,69
R8	28,0	1,48	1,51	1,53	1,56	1,59	1,62	1,64
R9	50,0	1,60	1,60	1,60	1,60	1,60	1,60	1,60
R10	To be used for extreme ice accretions							

It is important to mention that glaze ice is assumed to accrete uniformly around the entire surface of the object, subsequently the wind direction does not matter. However in the case of rime ice, the wind direction is taken into account in SS-ISO 12494:2017 which only provides corrected drag coefficient values for wind which is perpendicular to the accreted ice vane and to the length of the cable, which can seen in table 2.6. No values for drag coefficients exists in the case where the wind is parallel to the ice vane or at any other angle of attack (AoA).

2.3 Governing Equations

In computational fluid dynamics the governing equations are the core principles that determine the outcome of a fluid flow simulation. These equations are ruled by the the conservation laws of physics which states that:

- The mass is conserved.
- The momentum change is equal to the net force acting on the liquid according to Newtons second law.
- Energy is conserved according to the first law of thermodynamics.

These rules are described in more detail below according to Versteeg & Malalasekera [44]. The equations are described on the non-conserved form for an incompressible fluid.

[6] The table/equation is reproduced from SS-EN 1991-1-9:2025/ SS-ISO 12494:2017 / SS:EN 1991-1-4:2005 with due permission from SIS, Swedish Institute for Standards who also offers the complete standard for purchase. Copyright SIS. www.sis.se

Continuity equation

The continuity equation (2.6) states that the rate of increase of mass in a fluid element equals the net rate of flow of mass into a fluid element. In an incompressible liquid this equation equals zero, which gives:

$$\nabla \cdot \mathbf{u} = 0 \tag{2.6}$$

Momentum equation

The momentum equation (2.7) states that, in accordance with Newtons second law, that the rate of increase of momentum in a finite fluid volume equals the sum of forces acting on that same volume. This gives:

$$\frac{D\mathbf{u}}{Dt} = -\frac{1}{\rho}\nabla p + \nu\nabla^2\mathbf{u} \tag{2.7}$$

Energy equation

Finally, the first law of thermodynamics states that the rate of change of energy in a finite fluid volume equals the net rate of heat summed with the net rate of work exercised on the same volume, resulting in equation (2.8).

$$\rho c_v \frac{DT}{Dt} = k\nabla^2 T + (\boldsymbol{\tau} \cdot \nabla^T)\mathbf{u} \tag{2.8}$$

2.4 Spatial Discretization

As the Navier-Stokes equations are of continuous nature, they must be approximated by some form of discretization method. This converts the Partial Differential Equations (PDEs) into a system of algebraic equations which may later be solved iteratively. Two commonly used discretization methods includes the Finite Volume Method (FVM) and the Finite Element Method (FEM).

Finite Volume Method

The FVM is commonly used in CFD applications. It is based on dividing the computational domain into finite control volumes, for which all the governing equations will be solved for by applying the divergence theorem which transforms the volume integrals into surface integrals of fluxes. This approach has an advantage as it keeps the mass, momentum and energy conserved in each control volume. The FVM is the chosen type of discretization in both *ANSYS FLUENT* and in the *FENSAP-ICE* ice accretion & water runback module (*ICE3D*).

Finite Element Method

The FEM is another discretization method more commonly associated with solid mechanics, but may also be used in fluid mechanical problems as well. Here the continuum problem is divided into a finite number of elements and the equations are solved in the nodes between connecting elements. By the use of shape functions the solutions is then approximated in the cells between nodes. The FEM discretization model is used in the flow solver module (*FENSAP*) & Eulerian water droplet impingement solver module (*DROP3D*) in *FENSAP-ICE*.

2.5 Turbulence modeling

Turbulence physics is one of the most important unsolved problems in flow simulations today. The term turbulence is used to describe flow characteristics that have a highly unpredictable chaotic motion with swirls, and a wide range of eddy scales. While the Navier-Stokes equations describe both laminar and turbulent flows it is today impossible to predict its exact behavior. Instead some type of turbulence modeling is often needed. The most common types of methods of handeling turbulence includes: Reynolds Averaged Navier-Stokes (RANS), Large Eddy Simulations (LES) and Direct Numerical Simulations (DNS) where the computational cost is increased in the same order as presented above.

Reynolds Averaged Navier-Stokes

In RANS simulations focus lies on the average flow and how turbulence is best modeled to approximate the real behavior. By time-averaging the flow equations extra terms descendent from interactions between turbulent fluctuations appear. Versteeg and Malalasekera [44] explains more specifically, that when the momentum equation is time-averaged, six extra turbulent stresses, three normal and three shear, appear and are refereed to as the Reynolds stresses. Furthermore three extra terms also appear in the scalar transport equations. To accurately predict these new terms, turbulence closure models has to be used by setting up one, or more transport equations often together with the Boussinesq assumption (eg. Spalart-Allmaras, $k - \epsilon$, Reynolds stress model).

In many engineering applications of CFD, the focus lies on the averaged flow and its effect on the specified geometry (eg. velocities, pressures and shear stresses). Additionally, because of the acceptable computation costs, RANS simulations are often used.

Large Eddy Simulation

Large eddy simulations builds on the knowledge that large and small eddies behave differently. The smaller ones can often be seen as isotropic and having a universal behavior in the flow. Large eddies on the other hand interacts with the energy in the flow and will therefore be anisotropic and their behavior will be influenced by the geometry in the studied domain together with the boundary conditions and acting body forces [44].

The drawback with RANS is that it does not take these differences into considerations as all eddies needs to be modeled the same way. LES on the other hand uses a spatial filtering operation, that builds upon a filtering function and an eddy cutoff width, to separate the smaller eddies from the larger ones. It then uses transient simulations to calculate and resolve all the larger eddies while smaller ones below a certain threshold are left out. The small eddies, and how they interact with each other and around large eddies, are grouped together and is described by the sub-grid-scale (SGS) stresses which in turn needs to be modeled [44].

2.6 Multi-Phase Flow

To simulate ice accretion a multi-phase flow has to be used to account for the water droplets in the airstream. More precisely the droplet trajectories has to be calculated from the airstream, where either a Lagrangian or an Eulerian approach is used. While older programs usually favors the Lagrangian approach, newer ones like *ANSYS FENSAP-ICE*, implements the Eulerian approach [27]. The Lagrangian approach follows a single particle in both time and space throughout the flow, while the Eulerian approach describes how the flow properties vary over time for a fixed region of space [44].

The Eulerian droplet impingement solver module *DROP3D* in *FENSAP-ICE*, solves the flow as a continuum. The Navier-Stokes equations are then augmented with the droplets own continuity and momentum equations which results in the final dimensionless equations (2.9) and (2.10) [3].

$$\frac{\partial \alpha}{\partial t} + \vec{\nabla} \cdot (\alpha \vec{V}_d) = 0 \tag{2.9}$$

$$\frac{\partial (\alpha \vec{V}_d)}{\partial t} + \vec{\nabla}[\alpha \vec{V}_d \otimes \vec{V}_d] = \frac{C_D \mathrm{Re}_d}{24K} \alpha (\vec{V}_a - \vec{V}_d) + \alpha \left(1 - \frac{\rho_a}{\rho_d}\right) \frac{1}{Fr^2} \tag{2.10}$$

where

- α is the mean field value of the particle concentration
- V_d is the dimensoinless mean field of the particle velocity
- V_a is the dimensoinless air velocity
- C_d is the particle drag coefficient
- ρ_d is the droplet density
- Re_d is the particle Reynolds number as defined by (2.11)
- K is an inertial parameter as defined by (2.12)
- Fr is the Froude number which is proportional to the buoyancy and gravitational forces as defined by (2.13)

$$\mathrm{Re}_d = \frac{\rho_a d V_{a,\infty} \|\vec{V}_a - \vec{V}_d\|}{\mu_a} \tag{2.11}$$

$$K = \frac{\rho_d d^2 V_{a,\infty}}{18 L_\infty \mu_a} \tag{2.12}$$

$$Fr = \frac{\|V_{a,\infty}\|}{\sqrt{L_\infty g_\infty}} \tag{2.13}$$

The droplet drag coefficient can be modeled in *DROP3D* in various ways. For this study the "*Water - default*" correlation was chosen, which models the drag for spherical droplets as shown in equation (2.14) [3].

$$C_D = \begin{cases} (24/\mathrm{Re}_d)(1 + 0.15\mathrm{Re}_d^{0.687}) & \text{for } \mathrm{Re}_d \leq 1300 \\ 0.4 & \text{for } \mathrm{Re}_d > 1300 \end{cases} \tag{2.14}$$

Droplet dynamics

When the flow of a single droplet is considered, its trajectory will be defined by the drag and inertia acting on the volume and mass, when gravity and buoyancy forces are neglected. A higher inertia is defined by the droplet having a higher kinematic energy or a larger mass (larger size) [45]. Droplets are usually assumed to deform at higher Reynolds numbers. Thus an customized drag coefficient dependent on Reynolds number is often used.

If drag dominates the drag-inertia relationship the droplet will follow the streamline more closely, and as the streamlines are redirected around the body, smaller droplets are more likely not to make contact with the flow obstructing object. This is especially true for small droplets traveling at low velocities. If instead the inertia dominates the relationship (high velocities and large droplet size), the droplet will to a greater degree deviate from the flow path, and instead follow a more straight trajectory. This in turn make it more likely to collide with the object, as can be seen in figure 2.3. How the relationship between drag and inertia is divided, will have a great impact on the overall droplet Collision Efficiency (CE) [11] [16] [21] [24]. The collision efficiency is a percentual value calculated by taking the amount of droplets hitting the object in an obstructed flow and devising it by the amount of droplet that would collide with the object, if the flow is unaffected.

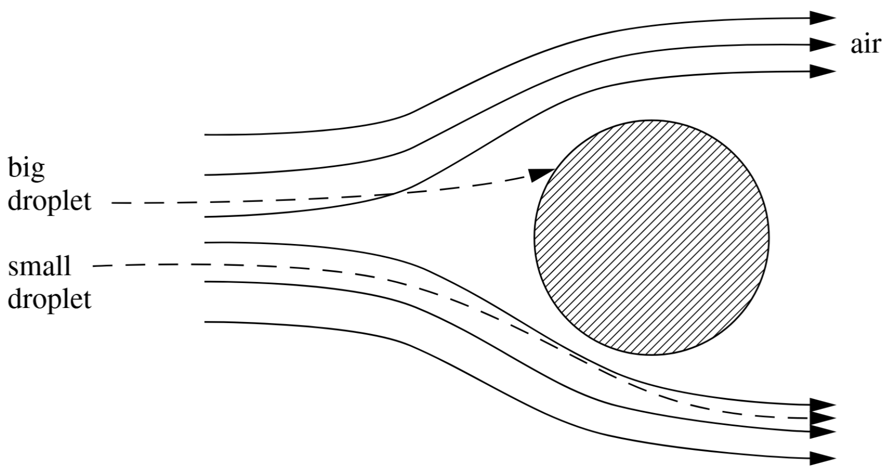

Figure 2.3 "Air streamlines and droplet trajectories around a cylindrical object." [24]. Used with permission.

2.7 Ice Accretion

As mentioned briefly in the introduction this study will focus on the ice accretion from atmospheric icing, which is the phenomenon where supercooled water droplets in the air freeze on impact with a solid surface [28]. Atmospheric icing may however be classified into two different processes, namely precipitation icing and in-cloud icing where the latter will be the target for this study.

During the literature review numerous of studies was found to have been conducted on in-cloud ice accretion. Especially in the fields of aeronautics and wind turbines (airfoils) but also on circular conductors and a few recent studies on contact wires.

Ice types

Depending on the weather conditions the structure of the accreted ice may vary. For warmer temperatures the formation of a solid and clear glaze ice (wet icing) will be dominant, while at colder temperatures and at lower wind velocities rime ice (dry icing) will be dominant instead [39]. The transition between the different ice types can be seen in figure 2.4 below.

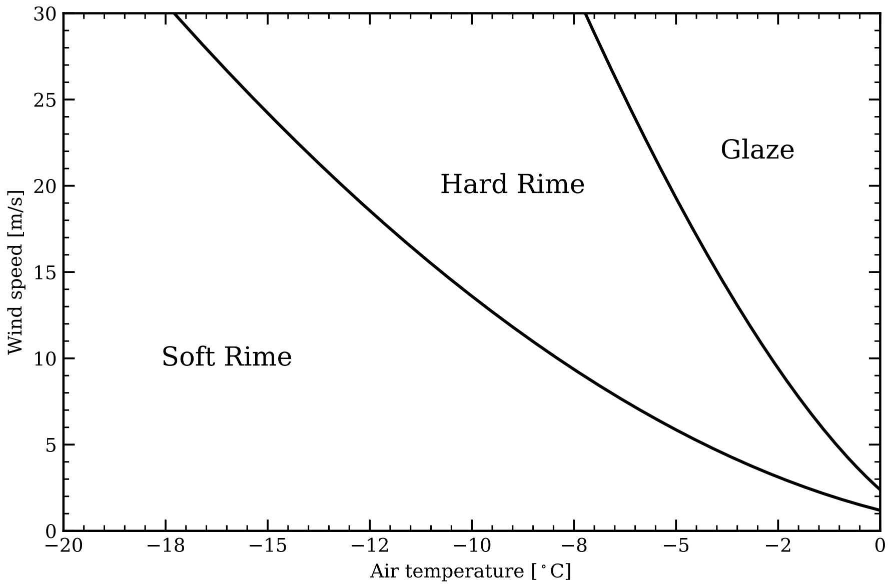

Figure 2.4 Icing regime classification as function of temperature and wind speed according to SS-ISO 12494:2017 [39]

Glaze ice - Wet growth.

Apart from the temperature and velocity dependency, glaze ice tend to form from freezing rain/drizzle or wet in-cloud icing and may result in accretion of asymmetric shapes and, or icicles [39]. The process is as follows: As the water droplets hit the object a liquid water film will spread out over the surface. Some of the liquid will run across the surface (runback) and some will drop of the surface (runoff). The ice accretion then develops from the freezing of the water closest to the surface, which may also entrap small deposits of liquid water [24], as can be seen in figure 2.5.

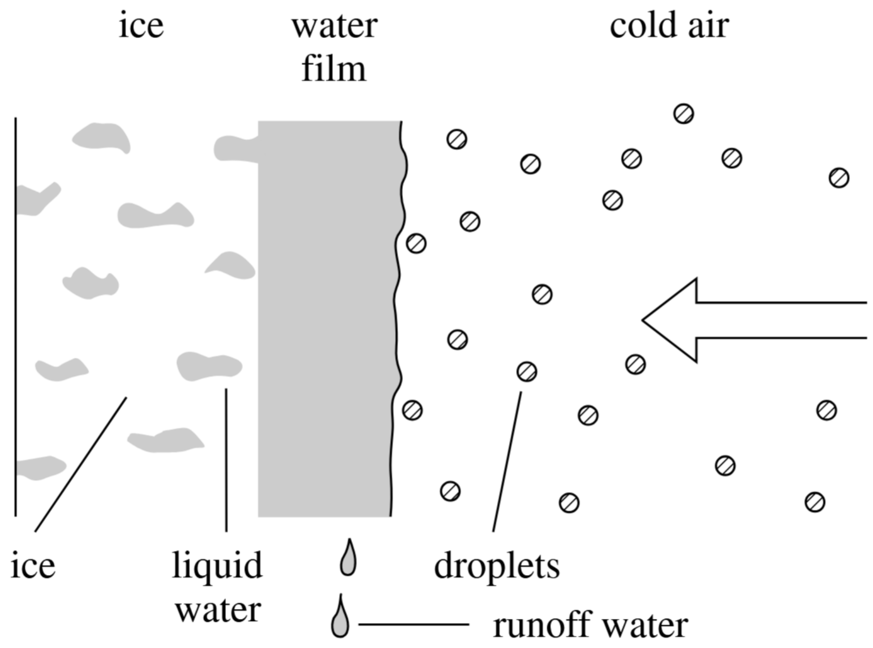

Figure 2.5 "Growth of glaze ice (wet growth)." [24]. Used with permission.

Rime ice - Dry growth.

For colder temperatures, accreted ice will instead be of a rime type, where all colliding droplets instantaneously freeze upon impact [24]. The freezing phenomenon will also trap air between the ice crystals [15] resulting in a less dense ice. This behavior can be seen in figure 2.6.

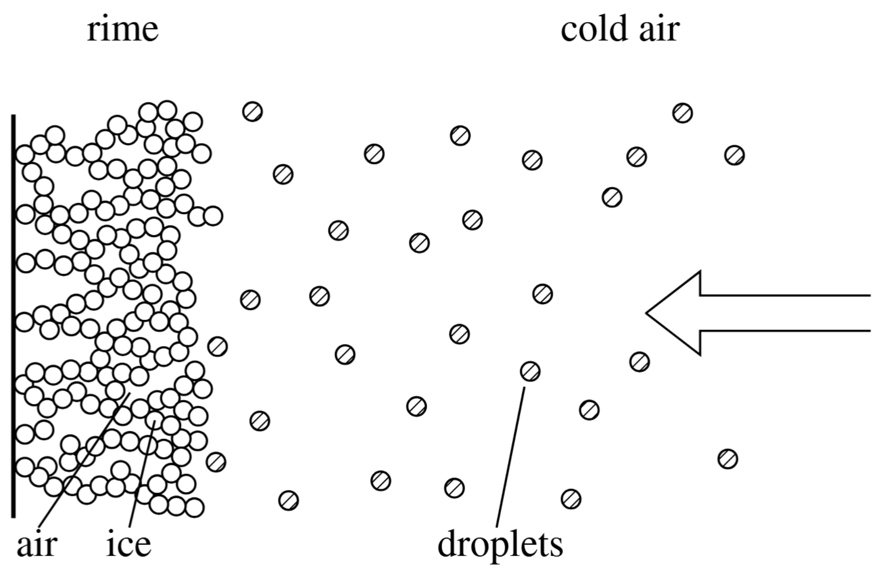

Figure 2.6 "Growth of rime ice (dry growth)." [24]. Used with permission.

Generally, rime ice has the highest likelihood of forming during in-cloud icing conditions and always forms in the windward direction from the geometry. It is even more likely to form for non-rotating geometries [39] like a contact wire.

Delimitation.

While Homola et al. [13] showed from their work on wind turbine airfoils that the shape from glace ice, a more asymmetric "horn shape", resulted in the highest drag increase. As well as fact that a real scenario might include a mix of the two ice types, especially in the ambient temperature ranges of $-1.8°C < T < -15.3°C$ [15]. This study will be confined to the formation of rime ice, as the circular geometry will not form the afformentioned "horn shape" and it is therefore believed that rime ice will contribute to the largest change in cross-sectional area and shape that will influence the forces acting on the object the most.

Ice density

Depending on which type of ice that builds on the line the properties, like density, will vary. According to SS-ISO 12494:2017 [39] it usually follows the properties as tabulated in table 2.7.

Table 2.7 Typical properties of accreted atmospheric ice [39] [7]

Type of ice	Density kg/m^3	Adhesion and cohesion	General appearance	
			Colour	Shape
Glaze	900	strong	transparent	evenly distributed/icicles
Wet snow	300 to 600	weak (forming) strong (frozen)	white	evenly distributed/eccentric
Hard rime	600 to 900	strong	opaque	eccentric, pointing windward
Soft rime	200 to 600	low to medium	white	eccentric, pointing windward

However in the case for numerical modeling of ice accretion, setting a single constant density is difficult. Instead the FENSAP-ICE User Manual [3] and SS-ISO 12494:2017 [39] recommends, for rime ice (dry growth), using the Macklin formula (2.15) that was put forth by Makkonen and Stallabrass [23].

$$\rho = 0.378 + 0.425 log_{10}(R_m) - 0.0823(log_{10}(R_m))^2 \tag{2.15}$$

where R_m is the Macklin's parameter defined by:

$$R_m = -\frac{v_0 d_m}{2T_s} \qquad \text{for } 0.2 < R_m < 170 \tag{2.16}$$

where

[7] The table/equation is reproduced from SS-EN 1991-1-9:2025/ SS-ISO 12494:2017 / SS:EN 1991-1-4:2005 with due permission from SIS, Swedish Institute for Standards who also offers the complete standard for purchase. Copyright SIS. www.sis.se

v_0 is the droplet impact velocity [m/s] [8]

d_m is the median volume droplet diameter [μm]

T_s is the mean surface temperature of the ice deposit [$°C$]

Influencing parameters

From the literature review it was found that the amount of ice accreted is dependent on numerous meteorological parameters including: wind velocity, atmospheric temperature, Liquid Water Content (LWC) and Median Volume Diameter (MVD) [39]. It was also found that a lower atmospheric temperature as well as a higher wind velocity, LWC and MVD results in larger amounts of accreted ice [16] [20] [21] [45]. However, Makkonen [24] explains that the most important factor for estimating iceloads may be the duration of the icing event itself.

Wind velocity.

As described in section 2.6 the ratio between the droplet inertia and drag is dependent on the wind velocity. Jin and Virk [16] showed that if the velocity increases, the inertia will as a result dominate and the droplet collision efficiency will increase. This will in turn leads to an increase in the amount of accreted ice. Xu et al. [45] reached a similar conclusion from their work on circular conductors. More specifically, that a higher wind velocity mainly affects the droplet collision efficiency by increasing the droplet kinematic energy. Thus, the trajectory of the droplet will be less disturbed by the diverging air flow which leads to an increased collision rate.

Atmospheric temperature.

The atmospheric temperature may affect the amount of accreted ice in three different ways. Firstly, it may affect the airflow around the geometry as the fluid temperature will impact the density and viscosity of said fluid. In the case of a fixed contact wire this dependency may be small as the temperature variations are minor, but for aeronautic applications, where large temperature ranges are present impact can be noticeable. Secondly, the temperature will affect the amount of water droplets that freeze upon impact, as a larger fraction of droplets are super cooled. Lotfi et al. [21] came to this conclusion with their numerical experiments, as the droplet collision efficiency stayed constant at varying temperatures but the shape of the accreted ice varied. They further explain that a temperature of $-25°C$, which is well within the range of rime ice accretion, the droplet freezing fraction is close to 100%. This is also described by Makkonen [24]. Thirdly, as the temperature drops so will the ice density as shown in table 2.7. As the accreted ice mass is independent on temperature and must stay constant, the accreted ice volume will increase.

LWC & MVD.

The LWC and MVD are measurements of the water content in the air [g/m^3], and the median droplet diameter [μm]. Both of which have a direct correlation to the ice growth. Once more, as described in section 2.6 the droplet behavior in the flow is dependent on

[8] The droplet impact velocity can in turn be described by equations derived by Blodgett & Langmuir [18]. To connect this more with the method, this relationship will be described in detail in Section 3.9.

the droplets inertia, where an increase in droplet size also will result in a higher droplet collision efficiency and therefore more ice accretion [16] [20] [21].

Lotfi et al. [21] as well as Jin and Virk [16] analyzed and further developed the impact of the droplet size distribution. The results showed that the choice of distribution, either monodispersed distribution (constant droplet diameter) or a *Langmuir B* to *Langmuir E* distribution, will affect the droplet collision efficiency as well as the rate, and shape of the ice accretion. The Langmuir droplet distribution, which was put forth by Langmuir and Blodgett in 1944 [18], can be described as a family of theoretical distributions based on the percentages of LWC for each droplet size. The distributions can be seen in table 2.8.

Table 2.8 Langmuir droplet diameter distribution vs. liquid water content. Where a is the droplet radius and a_0 is the radius of the volume median [18].

Liquid Water Content (%)	**B** a/a_0	**C** $(a/a_0)^{1.5}$	**D** $(a/a_0)^{2.0}$	**E** $(a/a_0)^{2.5}$
5	0.56	0.42	0.31	0.23
10	0.72	0.61	0.52	0.44
20	0.84	0.77	0.71	0.65
30	1.00	1.00	1.00	1.00
20	1.17	1.26	1.37	1.48
10	1.32	1.51	1.74	2.00
5	1.49	1.81	2.22	2.71

The distributions in figure 2.8 has been directly implemented in the *DROP3D* program. However, it is worth mentioning that for distribution B the ratio 1.49, at 5% LWC, is automatically set to 1.40 in *DROP3D*.

Bjørn Emil Nygaard, Ph.D. in Meteorology, when consulted on this topic explained that the Langmuir D distribution is an effective first guess when more information about the distribution is unavailable. This is also backed by numerous studies using the Langmuir D distribution for validation and testing [10] [11] [16] [20] [21].

Combining parameters.

In a real scenario. All of the meteorological parameters will statistically not likely experience their extreme value simultaneously. For example, Gent et al. [11] describes that an decrease in temperature also decreases the amount of LWC. This is also confirmed by SS-ISO 12494:2017 [39] which states that at ambient temperatures below $-20°C$ the LWC becomes so small that close to no in-cloud icing is present. As a result, a statistically likely but still extreme combination of all meteorological parameters is challenging to find.

Additional influences.

Apart from the meteorological parameters it is important to note that icing in general is highly dependent on the properties of the exposed objects. For instance the size, shape, flexibility, orientation, material and surface structure, are all parameters influencing the ice accretion [39].

2.8 Surface Roughness

An important parameter for accurate modeling of ice accretion and drag forces is the surface roughness. Martini et al. [27] showed from their study, that the choice of surface roughness can have a large impact on the ice accretion of an airfoil. This shows that not considering any roughness, can heavily impact the simulation results. Not considering roughness can also underestimate the impact on the aerodynamic drag with ice accretion present.

In both *ANSYS FLUENT* and *FENSAP-ICE* the surface roughness is modeled with so called sand-grain roughness. The roughness can either be set directly to a constant value (roughness height and roughness constant) or be calculated with the use of a model. Sand-grain roughness is often used in CFD applications where it describes a monolayer of sand, with the sand grain size (diameter) ϵ (also denoted k_s). In contrast the standard measure of surface roughness in tribology is the *arithmetic average of absolute values* or R_a-value, which is calculated as shown in equation (2.17).

$$R_a = \frac{1}{n}\sum_{i=1}^{n}|y_i| \tag{2.17}$$

To convert R_a to an equivalent sand-grain height, Adams et al [1] presented the following conversion table 2.9, resulting in more accurate results:

Table 2.9 Conversion Between Varoius Roughness Parameters to Sand-grain Roughness Height [1]

Roughness parameter	Estimated sand-grain roughness, ε
R_a	$\varepsilon = 5.863\, R_a$
R_{RMS}	$\varepsilon = 3.100\, R_{RMS}$
R_{zd}	$\varepsilon = 0.978\, R_{zd}$

With what is described above together with expected surface roughness found in literature, the surface roughness of the clean contact wire (a wire with no accreted ice) can be estimated. To find the surface roughness of the accreted ice, a number of existing methods can be used. Both *FLUENT* and *FENSAP* has integrated icing models that estimate the roughness based on varying input parameters.

The easiest way to model the surface roughness of ice is by using a specified constant sand-grain roughness height value, k_s [m]. Otherwise, the first model to consider is the *NASA roughness model*, where the equivalent sand-grain height is a product of the coefficients shown in equations (2.18), (2.19) and (2.20) that depend on the free stream velocity (V_∞), LWC and surface temperature (T_s) [3].

$$\left[\frac{k_s/c}{(k_s/c)_{\text{base}}}\right]_{V_\infty} = 0.4286 + 0.0044139V_\infty \tag{2.18}$$

$$\left[\frac{k_s/c}{(k_s/c)_{\text{base}}}\right]_{LWC} = 0.5714 + 0.2457(LWC) + 1.2571(LWC)^2 \tag{2.19}$$

$$\left[\frac{k_s/c}{(k_s/c)_{\text{base}}}\right]_{T_s} = 0.047T_s - 11.27 \tag{2.20}$$

The final equation can be seen in (2.21) where c is the chord of an airfoil, and $(k_s/c)_{base} = 0.001177$ [34] [3].

$$k_s = 0.6839\left[\frac{k_s/c}{(k_s/c)_{\text{base}}}\right]_{T_s}\left[\frac{k_s/c}{(k_s/c)_{\text{base}}}\right]_{LWC}\left[\frac{k_s/c}{(k_s/c)_{\text{base}}}\right]_{V_\infty}(k_s/c)_{\text{base}}\,c \tag{2.21}$$

Another model that can be used is the *Shin and Bond formula*, also known as the Shin et al. model, as presented by Shin et al [34]. This model is based upon the NASA correlation, but introduces the factor as seen in equation (2.22). This as they realized that the equivalent sand grain roughness is independent of the free stream velocity as described by Shin and Bond [35].

$$\left[\frac{k_s/c}{(k_s/c)_{\text{base}}}\right]_{\text{MVD}} = \begin{cases} 1, & \text{MVD} \leq 20 \\ 1.667 - 0.0333\,\text{MVD}, & \text{MVD} > 20 \end{cases} \tag{2.22}$$

In equation (2.22), MVD is the droplet mean diameter [3]. With this adaptation, the empirical correlation of the surface sand-grain roughness results in equation (2.23).

$$k_s = 0.6839\left[\frac{k_s/c}{(k_s/c)_{\text{base}}}\right]_{\text{LWC}}\left[\frac{k_s/c}{(k_s/c)_{\text{base}}}\right]_{T_s}\left[\frac{k_s/c}{(k_s/c)_{\text{base}}}\right]_{\text{MVD}}(k_s/c)_{\text{base}}\,c \tag{2.23}$$

While more advanced models, like roughness from beading (which is beneficial in multi-shot simulations [26]), are possible to use, a standard model choice in ice simulation studies seem to fall on the Shin et al. formula. Shin et al. is for instance the choice of Homola et al. [13] in their studies on wind turbine airfoil profiles, and the choice of Lotfi et. al. [21] in their study on circular and grooved conductors (contact wire). Martini et al. [27] concurs and explain how almost all CFD studies on iced wind turbines depend on the Shin et al. roughness model. When Martini et al. [26] conducted a research survey on the icing of wind turbine blades, they showed how a majority, 12 out of 22 studies that disclosed the model used, in fact uses the Shin et al. model.

2.9 Formulas

This section presents formulas and a quick explanation of its apllications. The formulas will later be used in the method section.

Drag coefficient

The drag coefficient represents the non-dimensional drag force acting upon a surface and is defined by formula (2.24).

$$C_d = \frac{2F_d}{\rho u^2 A} \tag{2.24}$$

where

F_d is the force in the flow direction $[N]$
ρ is the fluid density $[kg/m^3]$
u is the free stream velocity $[m/s]$
A is the reference area $[m^2]$

Strouhal number

The Strouhal number is a dimensionless number that is used to analyze oscillating flows. It is used together with the Reynolds number to predict forces, friction and heat transfer of oscillating flows. The Strouhal number is defined as shown in equation (2.25) [36].

$$St = \frac{f \cdot D}{U_\infty} \tag{2.25}$$

where

f is the vortex shedding frequency $[Hz]$
D is the characteristic length $[m]$
U_∞ is the free stream velocity $[m/s]$

Lienhard [19] showed that for a flow over a typical cylinder, especially within the Reynolds number range of $10^3 < Re < 10^5$, the Strouhal number will remain constant at $St = 0.2$. This is confirmed by the wind tunnel tests done by Delany and Sorensen [8].

Sutherland's law

The viscosity of a fluid is dependent on its temperature. A common way to model a fluids viscosity is through Sutherland's law [38], that relates the dynamic viscosity to temperature by equation (2.26).

$$\mu = \mu_0 \left(\frac{T}{T_0}\right)^{\frac{3}{2}} \frac{T_0 + S}{T + S} \tag{2.26}$$

where

μ is the dynamic viscosity $[Pa \cdot s]$

μ_0 is the reference viscosity value $[Pa \cdot s]$
T is the static temperature $[K]$
T_0 is the reference temperature in $[K]$
S is Sutherland constant $[K]$

For air at moderate temperatures and pressures, the following values are commonly used [3]:

$$\mu_0 = 1.716 \cdot 10^{-5} \; [kg/m \cdot s]$$
$$T = 273.11 \; [K]$$
$$S = 110.56 \; [K]$$

Ideal gas law

The ideal gas law is the relation between a gas pressure and volume against its temperature for ideal gases at low densities and is shown in equation (2.27) [6].

$$PV = nRT \tag{2.27}$$

where

P is the absolute pressure $[Pa]$
V is the specific volume $[m^3]$
n is the amount of substance $[mol]$
R is the universal gas constant $[J/mol \cdot K]$
T is the absolute temperature $[K]$

Dalton's law

Dalton's law states that in a mixture of non reactive gasses, the total pressure is equal to the sum of partial pressures exerted by the individual gasses. As shown in equation (2.28).

$$p_{\text{tot}} = \sum_{i=1}^{n} p_i = p_1 + p_2 + p_3 + \cdots + p_n \tag{2.28}$$

Teten's equation

Theten's equation is an empirical formula used to describe the temperature dependence of the saturation vapor pressure in the atmosphere, as seen in equation (2.29) [29]. This can then be used to calculate the air density for humid air.

$$E_s = 6.1078 \exp \frac{a(T - 273.16)}{T - b} \tag{2.29}$$

where

E_s is the saturation vapor pressure $[hPa]$

T is the temperature $[K]$

and

For T $\geq$ 0°C	For T < 0 °C
$a = 17.2693882$ $b = 35.86$	$a = 21.8745584$ $b = 7.66$

Makkonen's formula

Makkonen's formula is an empirical formula used to estimate the accumulation of ice mass during an ice accretion event for a certain object. [24] The formula consists of meteorological parameters, but also includes parameters connected to the cross section, and the turbulence it induces.

$$\frac{dM}{dt} = \alpha_1 \cdot \alpha_2 \cdot \alpha_3 \cdot w \cdot v \cdot A \tag{2.30}$$

where

$\frac{dM}{dt}$ is the mass accretion rate $[kg/s]$

α_1 is the collision / collection efficiency $[-]$

α_2 is the striking efficiency $[-]$

α_3 is the accretion efficiency / freezing fraction $[-]$

w is the mass concentration of particles in the air $[kg/m^3]$

v is the particle velocity $[m/s]$

A is the cross-sectional area $[m^2]$

Bernoulli's equation

For an inviscid and incompressible flow, where the density is constant, Bernoulli's equation states that the total pressure, given by the sum of the static and dynamic pressure, stays constant throughout the flow as presented in equation (2.31) [2].

$$p + \frac{1}{2}\rho V^2 = \text{const} \tag{2.31}$$

where

p is the static pressure $[Pa]$

ρ is the density of the fluid $[kg/m^3]$

V is the flow velocity $[m/s]$

Bernoulli's equation may be used to calculate the static pressure or velocity at any point in a flow if the other parameter is known. This principle is commonly used when the free stream velocity is to be determined with a pitot tube.

2.10 Wind Tunnel

A wind tunnel is an experimental aerodynamics equipment used to study the effects of airflow around an object. The wind tunnel makes it possible to study the flow and forces (Lift and Drag) acting on an object in a controlled environment [30].

The tunnel itself can be either open circuit or closed circuit. A closed circuit wind tunnel, as the name suggests, is constructed so the same air is recirculated in the tunnel. An open circuit wind tunnel instead draws new air from its surroundings, through the test chamber, over the object to then let back out to its surroundings through the diffuser. Apart from its type, a wind tunnel is also usually classified by the velocity range that can be reached in the test section.

Figure 2.7 shows a schematic of an open circuit wind tunnel used for the experiments. The four main parts are the contraction section, test section, turbine and the diffuser.

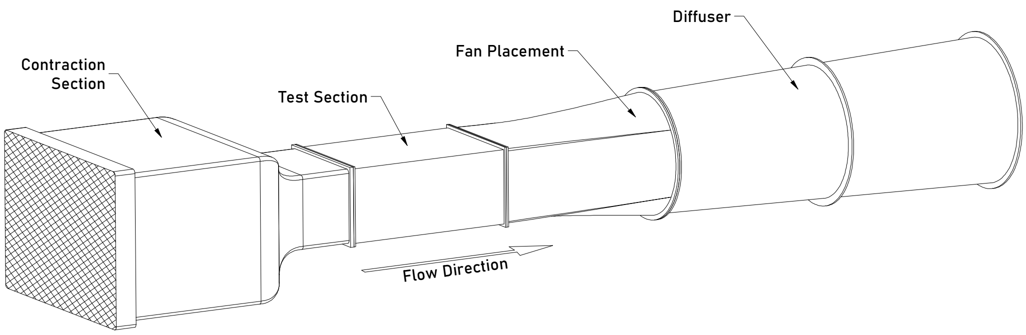

Figure 2.7 Schematic Open Circuit Wind Tunnel

In contrast to many real scenarios, the wind tunnels test section is confined in size. This can be problematic if the walls of the test section impacts the flow and subsequently the experimental readings. To ensure that this effect is negligible or to find a viable correction method, the blockage ratio needs to be determined for the specific experiment.

Al-Obaidi and Madivaanan [30] describes the blockage ratio as the ratio of the projected area of the model and the test section's cross-sectional area. Through experiments with airfoils and spheres in an open-circuit low speed wind tunnel, they found that a blockage ratio less that 16% had no significant impact on the results. It is however advantageous to keep this ratio as low as possible to minimize eventual disturbances.

3

Methodology

3.1 Drag Coefficient Pre-Study

To ensure that the numerical simulations produce reliable results, some form of validation is required. However, in the field of CFD simulations on contact wires, there exists only a limited amount of research providing results such as the drag coefficient for the contact wire. Therefore the validation will instead be carried out on the well-studied case of a cylinder, with a diameter of 12 mm.

Initially in the process of acquiring drag coefficients with RANS and Unsteady RANS (URANS) simulations, it was found that all simulated drag coefficient values deviated somewhat from the experimentally well established value of $C_d = 1.2$. The value of 1.2 is a well validated value for cylinders for Reynolds numbers around, $Re \approx 10^4$ [8] [19] [2]. As can be seen in figures 3.1-3.4, all transient simulations score high at around 1.5, while the steady simulations lay low around 0.8, giving an error of 25% and 33% respectively. It can be noted that there is rather few steady state simulations. Initially more of these were conducted, although this was so early in the process, that the results were not saved as it was thought that the deviation in C_d would not be so extensive after fine tuning.

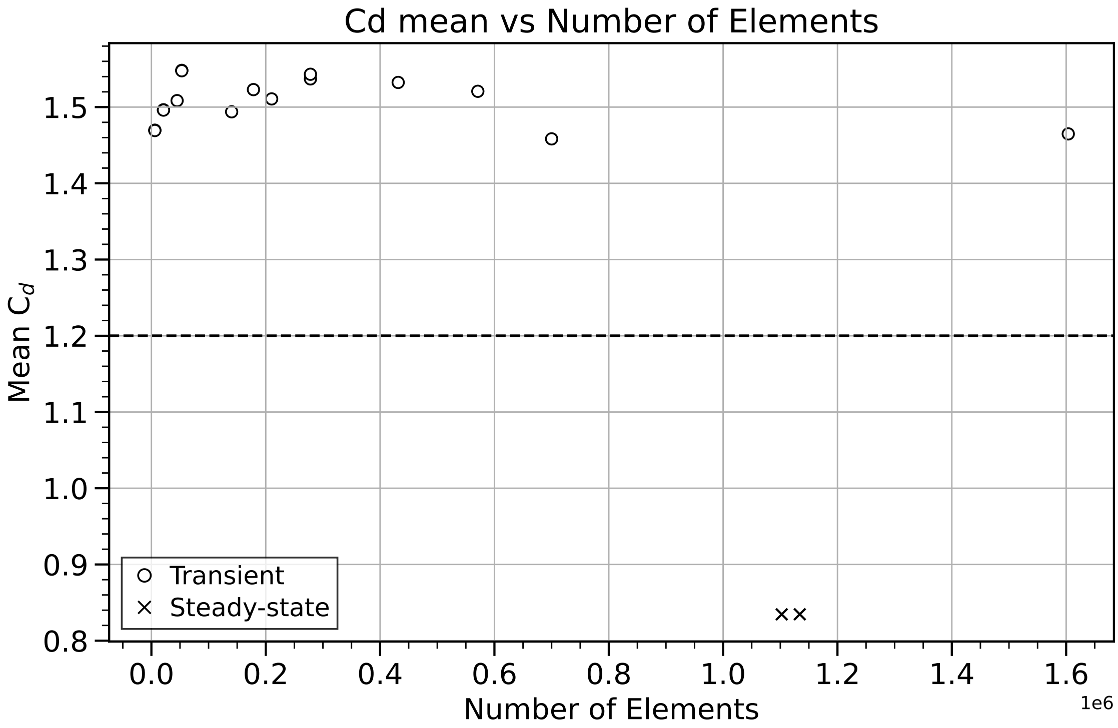

Figure 3.1 C_d as a Function of Element Count

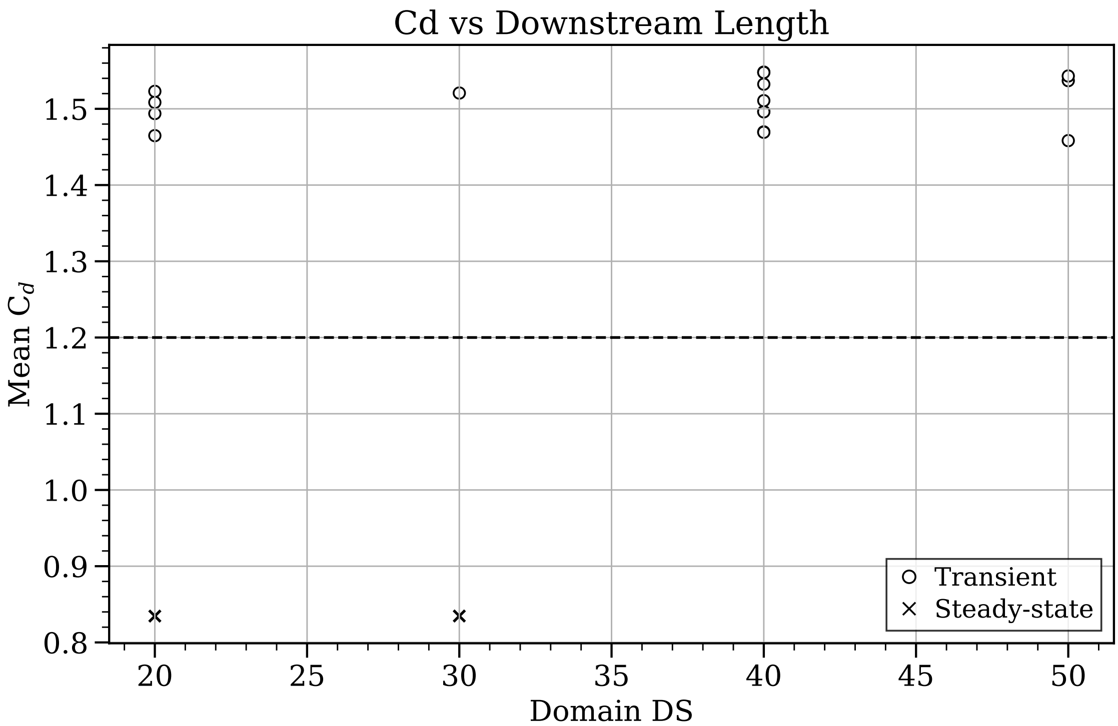

Figure 3.2 C_d as a Function of the Domain Length Downstream Measured in the Model Diameter

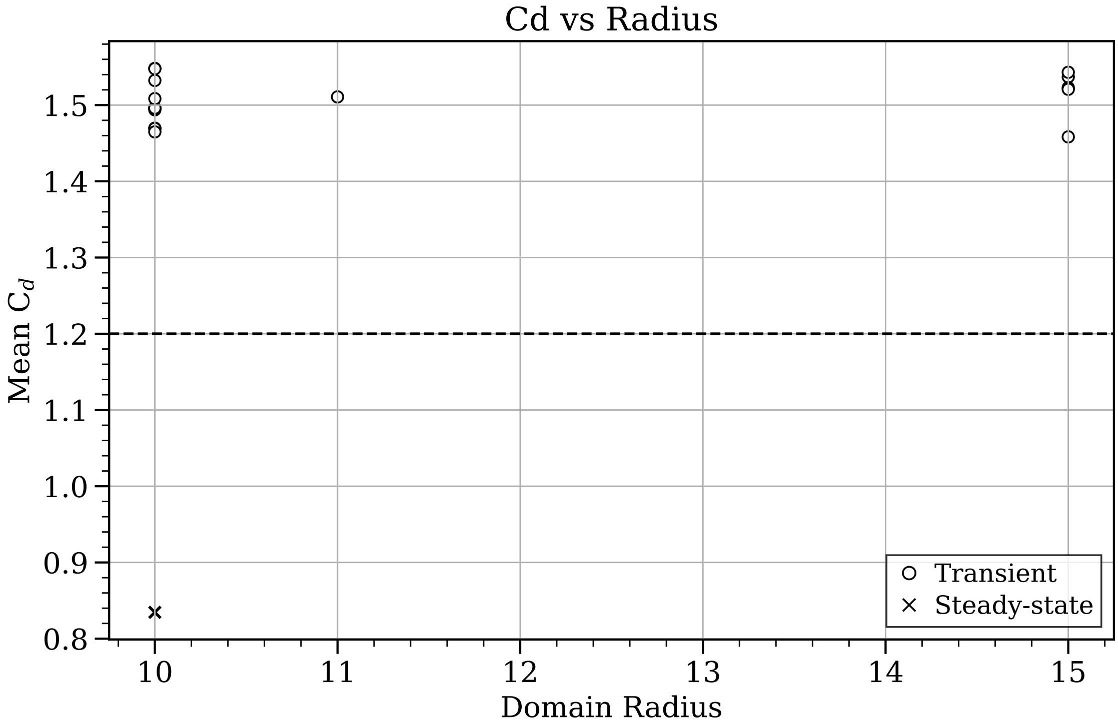

Figure 3.3 C_d as a Function of the Domain Inlet Radius Measured in the Model Diameter

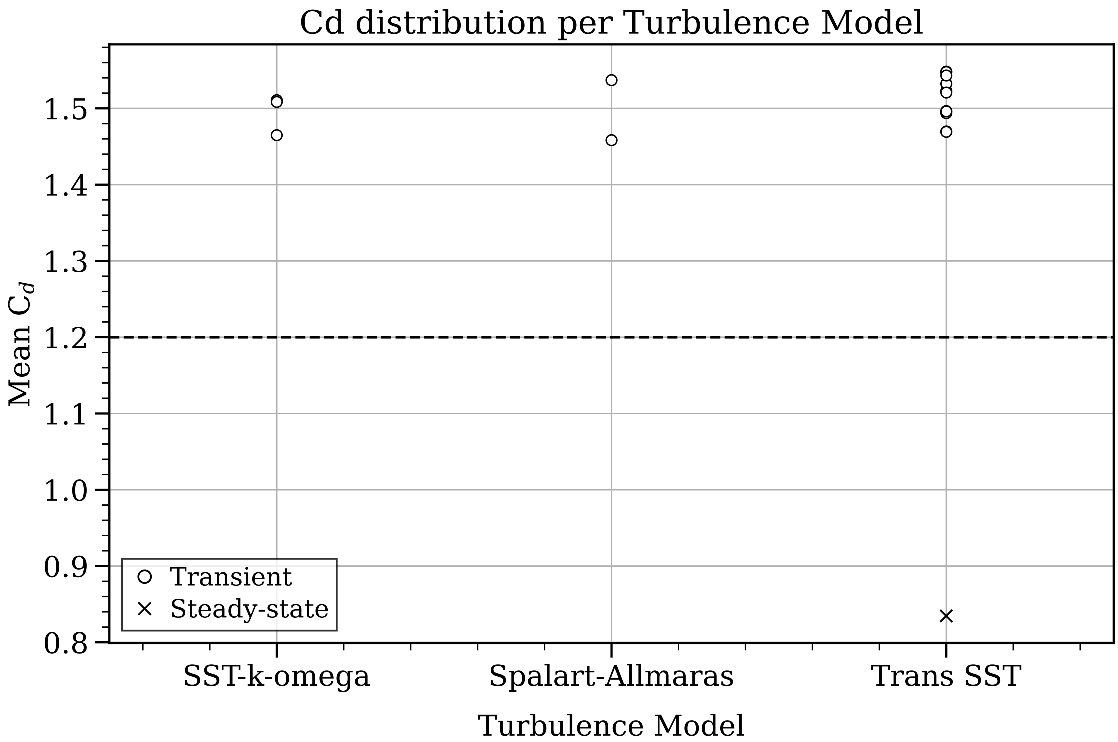

Figure 3.4 C_d for Different Turbulence Models

Despite these results it was decided to move on with the most promising setup, which can be seen in table 3.1.

The C-shaped polyhedral domain with a further C-shaped refinement section (see figure 3.5) was used. As this setup was computationally stable and in some tries provided values closer to 1.2, it was chosen for the domain study seen in section 3.2. Additionally, because the steady state simulation had worse results as well as convergence issues in three-dimensional simulations, it was decided that further work would be carried out with transient solutions only. This decision can also be motivated by the fact that the flow around a cylinder by nature is highly time dependent.

As a consequence of using transient simulations, a time-step had to be chosen. This time step was based on the Strouhal number for a cylinder as presented in section 2.9, which ensures sufficient resolution of the vortex shedding phenomenon. By using formula (2.25) the shedding frequency could be calculated to $f = 250Hz$ which makes the period for vortex shedding $T = 1/f = 0.004s$. To ensure proper resolution of the vortex cycle, each period should be divided in multiple time-steps to capture this physical phenomenon. Before a time-step sensitivity analysis could be conducted, see section 3.4, a fine resolution of 200 time-steps per vortex shedding period was chosen. This resulted in a times-step of $\Delta t = 0.004/200 = 2 \cdot 10^{-5}s$.

3.2 Domain Study

Domain configuration

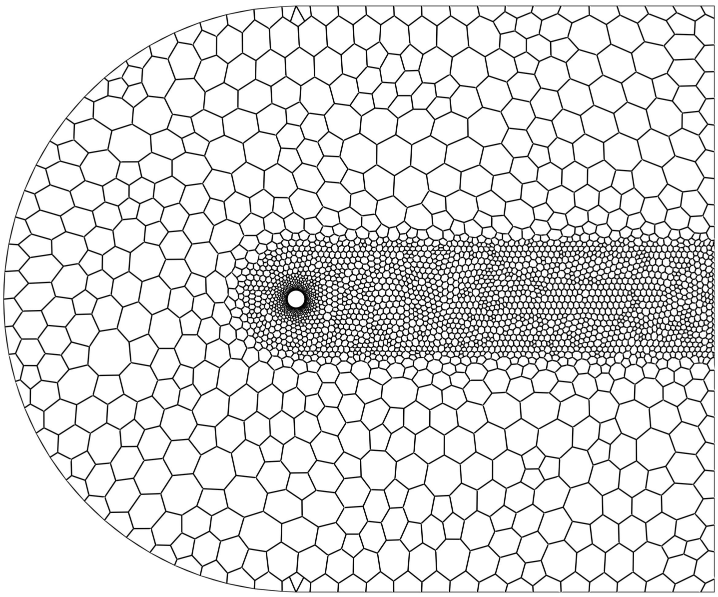

Figure 3.5 Domain Configuration - Overview

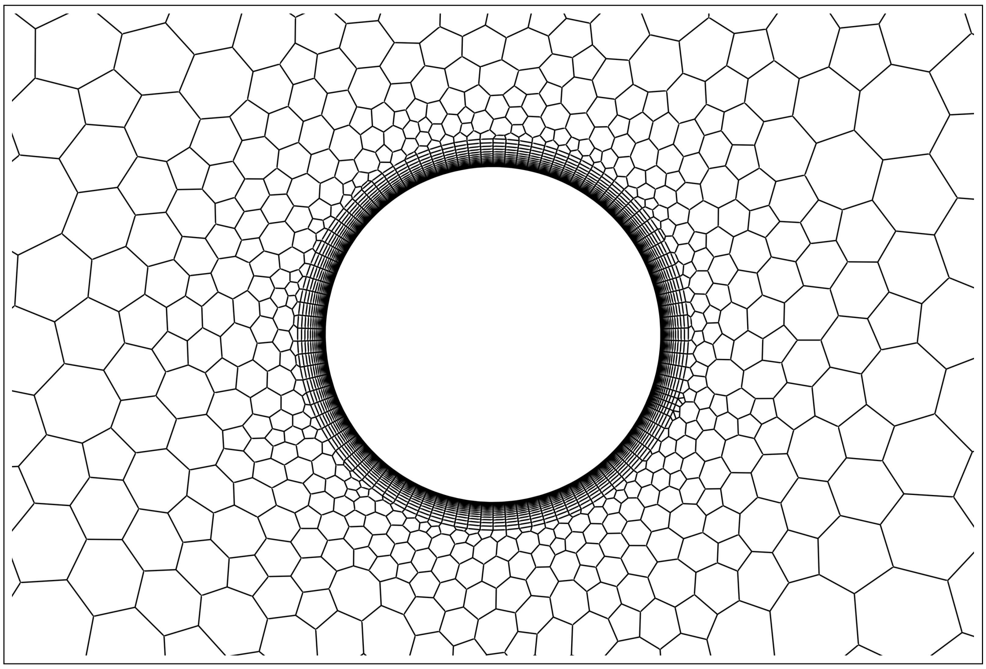

Figure 3.6 Domain Configuration - Refinement Region

In figure 3.5 the C-shaped domain including its refinement region can clearly be seen. 20 inflation layers, with a growth rate of 1.15, was added closest to the profile, as can be seen in figure 3.6. This ensures that the $y+$ value at 15 m/s is below 1.

As the *FENSAP-ICE* software does not allow 2D-meshes, the domain was extruded to a small depth of 10 mm to ensure that the necessary criteria were met while keeping the computational cost low.'

As for the boundary conditins the C-shape was defined as the velocity inlet, the end on the right hand side as a pressure outlet, the cylinder as a non slip wall with constant temperature and the y- and z-planes as symmetry planes.

For the domain study the parameters in table 3.1 was used.

Table 3.1 Chosen Input Parameters for the Domain Study

Domain Study Parameters		
Parameter	Value	Unit
Turbulence model	k-ω SST	–
Inlet Velocity	15	m/s
Velocity Direction	[1,0,0]	–
Turbulence Intensity	5	%
Turbulent Viscosity Ratio	10	–
Inlet Temperature	268.0	K
Cylinder Surface Temperature	280.0	K
Solver Scheme	SIMPLEC	–
Skeweness Correction	5	–
Discretization	Second-Order	–
Residual Limit [all]	1e-5	–
Time Step Size	2e-5	s
Total Flow-Time	≥ 0.1	s

Initially the radius of the C-domain was studied, a constant downstream length of 30 cylinder diameters was chosen. The results can be seen in figure 3.7.

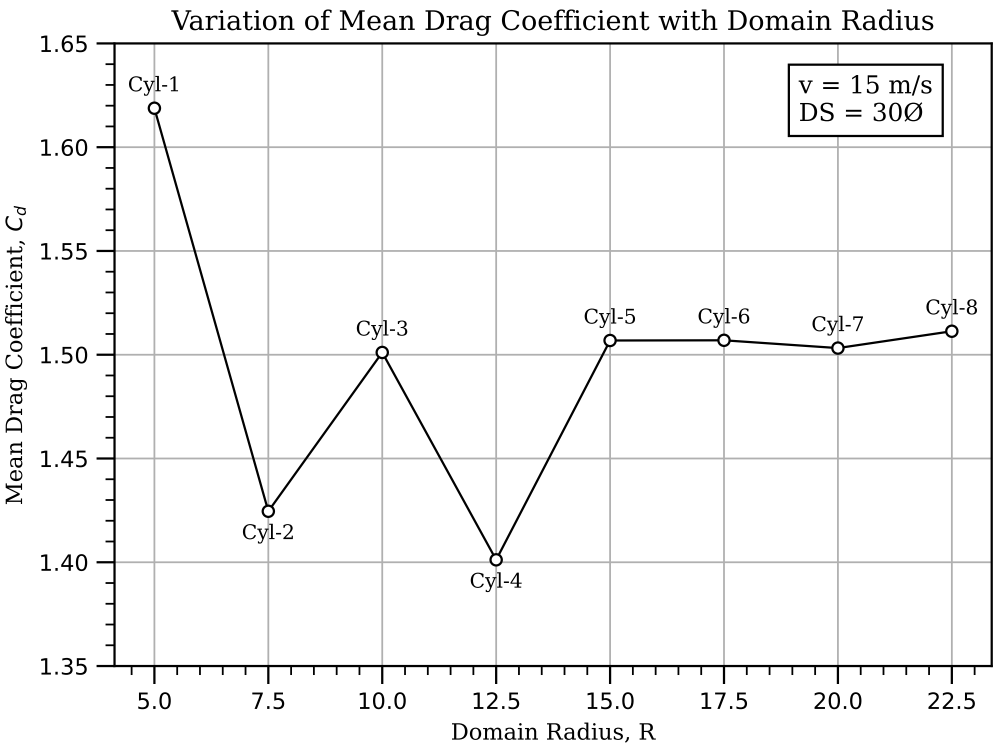

Figure 3.7 Domain Study for Varying Domain Radius

For the downstream study a constant radius of 15 cylinder diameters was picked. In hindsight a radius of 17.5 would have suited better, but at the time of simulation a typo in the plot-code showed the same C_d for *Cyl-4* and *Cyl-5* leading to 15 diameters downstream being a conservative value.

Next the downstream length was examined. It can be seen in figure 3.8 that the drag coefficient is rather stable for all dimensions. A value of 25 diameters was picked for the downstream length, mostly because it from experience and comparison to airfoil studies, gave a domain with a similar aspect ratio.

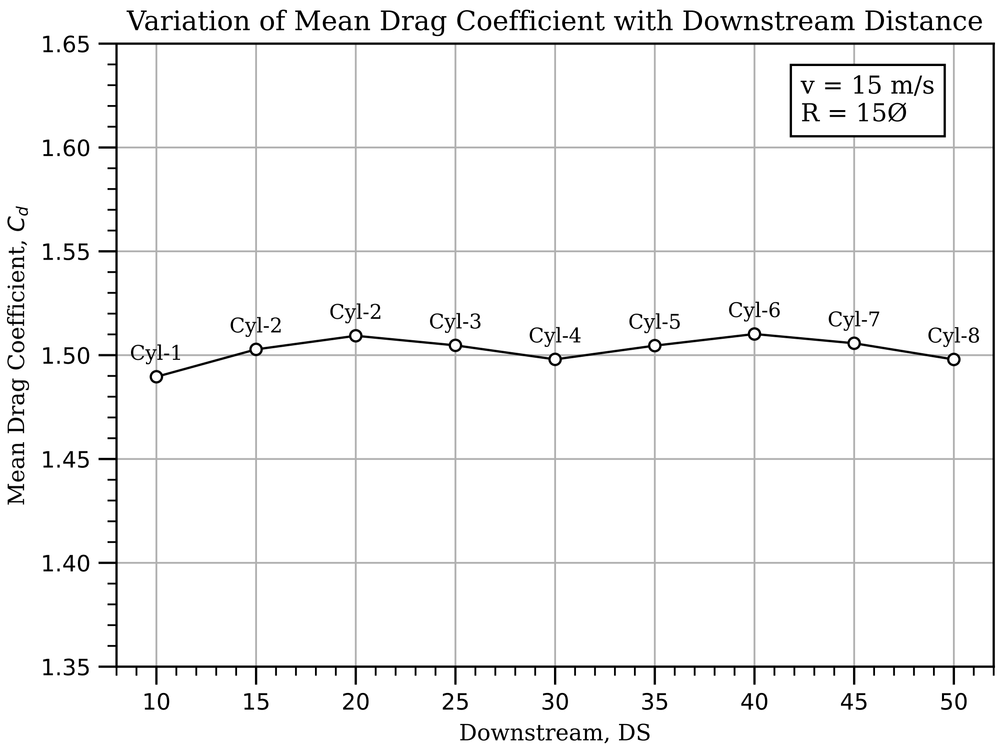

Figure 3.8 Domain study for Varying Domain Length Downstream

From the results in figure 3.7 and 3.8 a radius of 17.5 and downstream of 25 cylinder diameters was chosen for the remaining studies and simulations. This domain has a blockage ratio of 2.86%, which should not affect the results noticeably.

3.3 Mesh Sensitivity Analysis

To ensure that the solution is independent of the mesh size, a mesh sensitivity study was performed, as can be seen in figure 3.9.

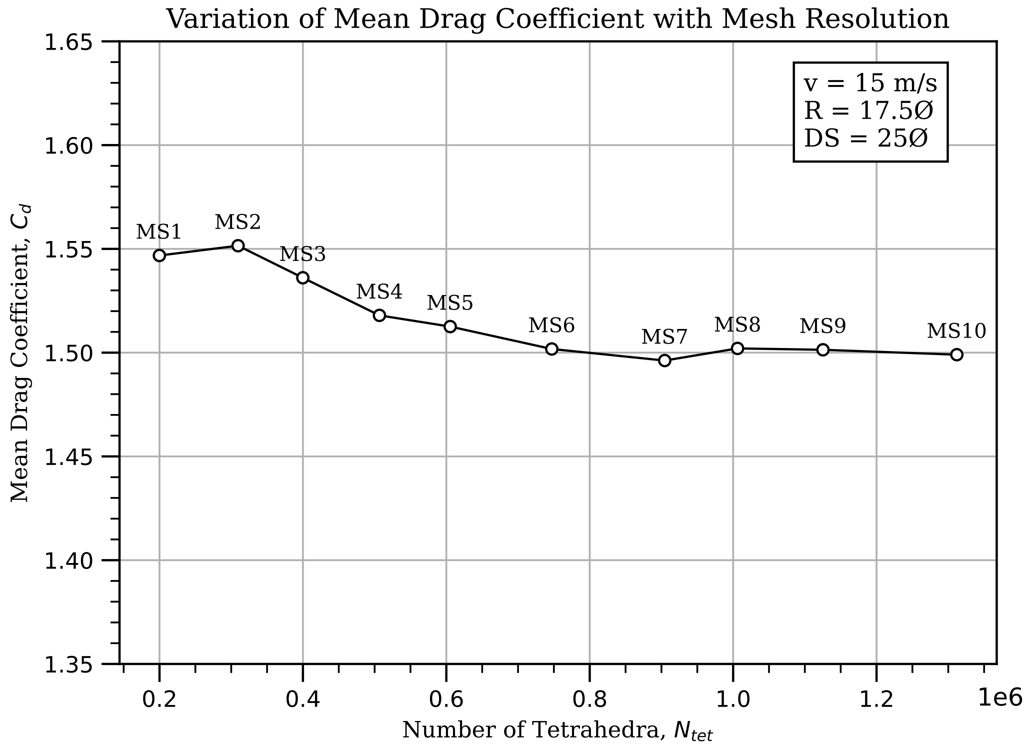

Figure 3.9 Mesh Sensitivity Study

With a change in drag coefficient of 0.371% comparing MS6 and MS7, MS6 was chosen for further studies, as further refinement of the mesh gave no better accuracy but added unnecessary computational cost.

3.4 Time-Step Sensitivity Analysis

A time-step analysis was carried out to ensure that a sufficient time resolution was acquired.

The time-steps examined were determined from the Strouhal number (see section 2.9) to include a certain amount of iterations N for each vortex shedding. The period for the vortex shedding was determined using equation (2.25), and the time step was subsequently calculated to fit N iterations as can be seen in table 3.2. The results from the simulations can be seen in figure 3.10.

$$T = \frac{1}{f} = \frac{D}{St \cdot U_\infty} = \frac{0.012}{0.2 \cdot 15.0} = 4.0 \cdot 10^{-3} s$$

Table 3.2 Time-Step Analysis

Time-Step Analysis		
Name	N	$\Delta t = T/N$ [s]
TS9	240	$1.67e{-5}$
TS8	200	$2.00e{-5}$
TS7	120	$3.33e{-5}$
TS6	60	$6.67e{-5}$
TS5	40	$1.00e{-4}$
TS4	30	$1.33e{-4}$
TS3	20	$2.00e{-4}$
TS2	10	$4.00e{-4}$
TS1	5	$8.00e{-4}$
TS0	3	$1.33e{-3}$

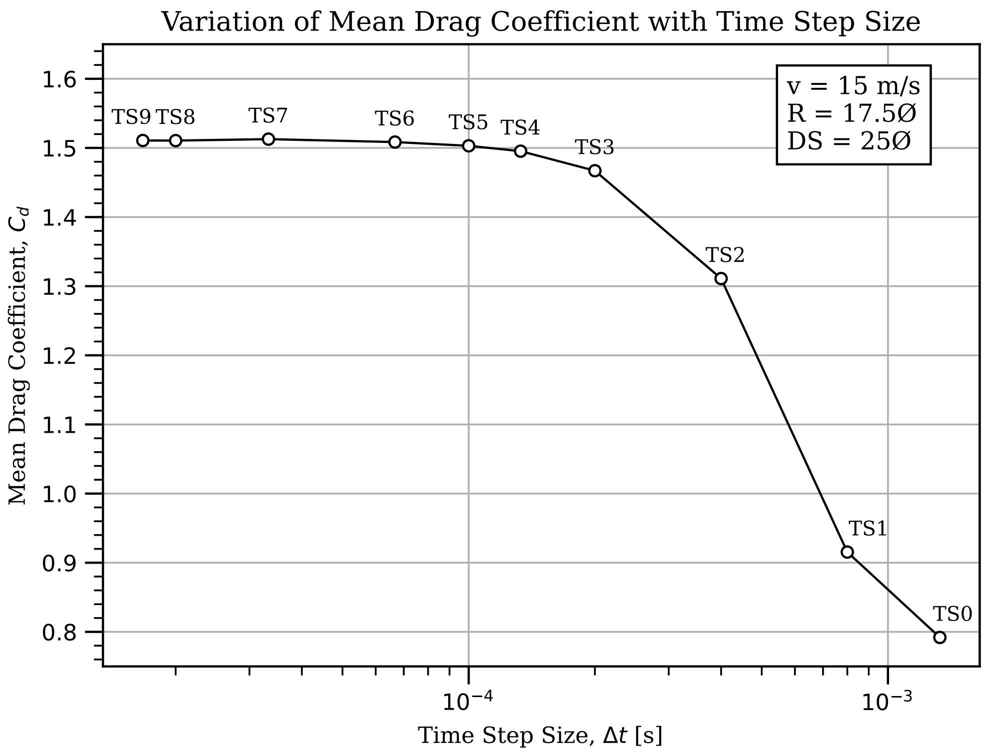

Figure 3.10 Time-Step Sensitivity Analysis

From figure 3.10 it can be seen that after TS4 the drag coefficient declines towards 0.8 at TS0, this is likely because a higher time-step results in a pseudo-steady state simulation. which from earlier results in drag coefficients around 0.8 (see figures 3.1 - 3.4) For the future studies and the remainder of this study TS5, with a time step of $\Delta t = 1e - 4s$, was used.

3.5 Turbulence Model Sensitivity Analysis

To ensure that the results are independent from the chosen turbulence model, simulations with different turbulence models was tested. The results are shown in figure 3.11.

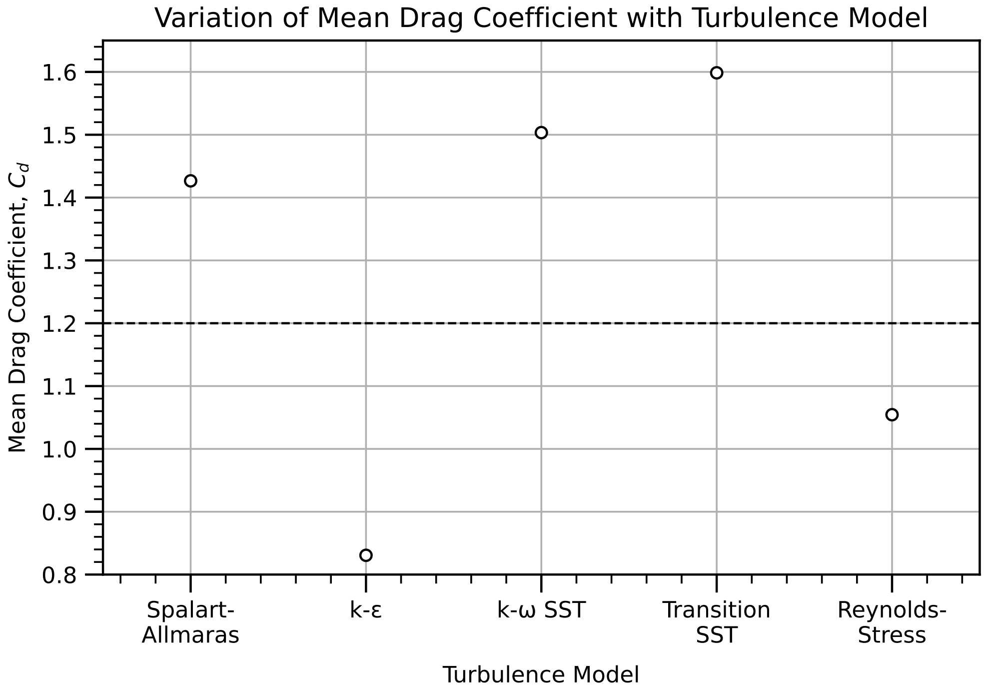

Figure 3.11 Turbulence Model Sensitivity Analysis

As can be seen from figure 3.11 the choice of turbulence model will have a major impact on the drag coefficient. For this study the choice stood between Spalart-Allmaras and the k-ω Shear Stress Transport (SST) model for a number of reasons. Firstly, these turbulence models are the ones, together with a model called *Low Reynolds* k-ω, that are implemented in the *FENSAP-ICE* code. Secondly, in *FLUENT* only these two models are implemented with more advanced surface roughness models to be used with icing [4], as the Shin et al. roughness model described in 2.8. Lastly, when Martini et al. [26] conducted a survey study on the icing of wind turbine blades, these two models were the most frequently used ones.

Spalart-Allmaras is a one-equation turbulence model that was developed specifically to be used in aeronautics. It is however also readily used in simulations on wind turbines [27]. Makkonen et al. [25] however explains that, for a 2D case, it is also suitable for modeling airflow during ice accretion on conductors.

The k-ω SST model is a two-equation turbulence model that combine, through a transformation, the strengths of both the classic k-ω in near wall regions, and the k-ϵ in the far field flow with fully developed turbulence [44].

Versteeg and Malalasekera explains how for external flows, both Spalart-Allmaras and k-ω SST are suitable models, but that k-ω SST is the most general and which shows the best results in tests for flows with zero or adverse pressure gradients. It is also mentioned how Spalart-Allmaras is not suitable for *General purpose CFD* while k-ω SST is. Additionally, the literature review on the area shows that all studies on icing of conductors or contact wires used the k-ω SST model [20] [7] [45] [21] [46]. Therefore the choice of turbulence model for the remainder of the study was the k-ω SST model, if not otherwise mentioned.

3.6 Surface Roughness Sensitivity Analysis

To analyze the impact of surface roughness, a parametric study was carried out with varying sand-grain roughness heights on the cylinder surface. Different sand-grain roughness between 1e-6 and 1e-3 was simulated, and the results can be seen in figure 3.12.

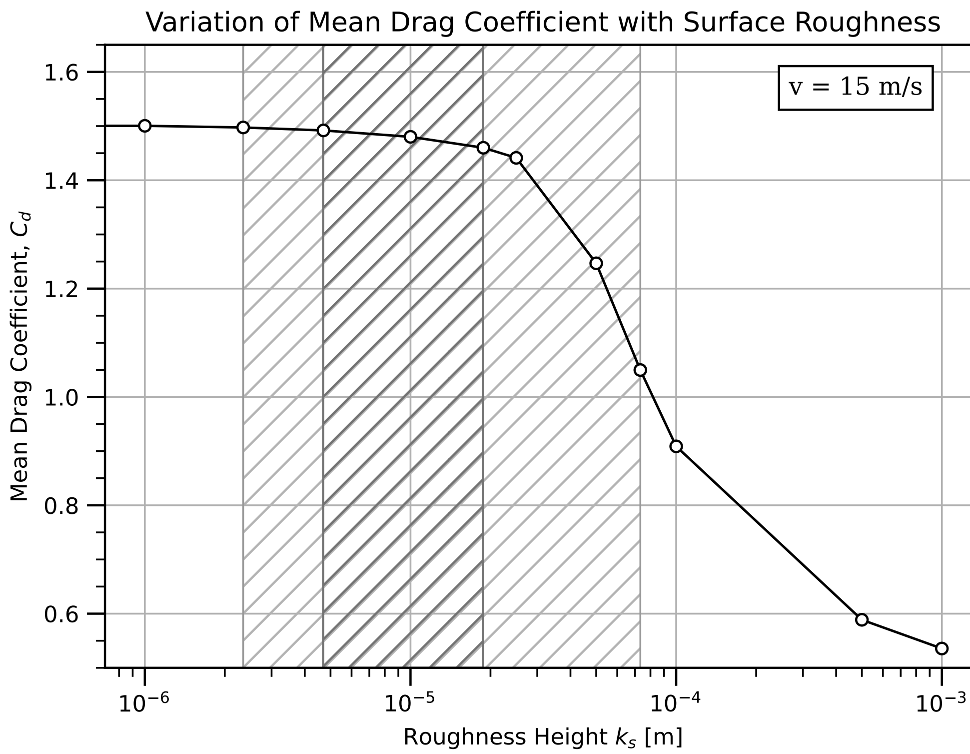

Figure 3.12 Surface Roughness Sensitivity Analysis

From figure 3.12 it can clearly be seen that there is a strong relationship between the roughness and the resulting drag coefficient, where a high roughness results in a low drag. This relationship is probably due to the slow introduction of the "drag crisis", where the flow stays attached for longer and in turn reduces the wake.

The dashed areas in 3.12 correlates to the "normal" (dark gray) and "less likely" (light gray) outcome of the extrusion process [22], used for making contact wires. The values used in Lundkvist [22] are given in R_a and are subsequently converted to sand-grain roughness by table 2.9.

A sand-grain roughness in the middle of the "normal" values of $k_s = 1e-5$ was chosen for future simulations of clean contact wires. The decision was made as it is in the middle of the "normal" section of contact wires. Additionally, a smaller roughness height will not impact the resulting drag. A larger value on the roughness height is also not desirable as the study wishes to see when the highest wind loads are present and therefore when the drag coefficient is at its maximum.

3.7 *FENSAP-ICE* - Parameter Study

FENSAP-ICE is constructed of three main modules. *FENSAP*, which is the flow solver. *DROP3D*, the Eulerian water droplet impingement solver and *ICE3D*, the ice accretion and water runback solver. Where the results from the earlier module are used as an input in following module.

To understand how the ice behaves for different parameters, a parameter study similar to earlier sections, but in *FENSAP-ICE* was conducted. The domain and mesh used is the same as was specified in the previous chapter, where a refined C-shape domain with a radius of 17.5 diameters and a downstream of 25 diameters was used. The time-step and mesh resolution etc. from previous studies are also transferred, if not otherwise stated.

The following parameters in table 3.3 was used for the base case. If not otherwise specified the default value was used.

Table 3.3 Initial *FENSAP-ICE* Parameters

***FENSAP-ICE* Parameters**

Parameters - *FENSAP*	Value	Unit
Turbulence model	k-ω SST	–
Turbulence Intensity	1	%
Turbulent Viscosity Ratio	1	–
Surface Roughness	–	–
Air Velocity	5	m/s
Velocity Direction	[1,0,0]	–
Air Static Pressure [altitude]	0	m
Air Static Temperature	238.15	K
Cylinder Surface Temperature	238.15	K
Time Integration	Unsteady - Constant Time Step	–
Time Step Size	1e-4	s
Total Time	≥ 0.3	s
Newton Iterations Per Time Step	75	–
Cross-Wind Dissipation	1e-7	–
Robustness Order	100	%
Convergence Level [all]	1e-5	–
Parameters - *DROP3D*		
Particle Type	Droplets	–
Droplet Drag Model	Water - Default	–
Liquid Water Content	1	g/m^3
Droplet Diameter	20	microns
Water Density	1000	kg/m^3
Droplet Distribution	Monodisperse	–
Parameters - *ICE3D*		
Ice - Water Model	Rime	–
Compute EID	Enabled	–
Relative Humidity	100	%
Ice Density Type	Constant	–
Constant Ice Density	917	kg/m^3
Total Time of Ice Accretion	3600	s

To evaluate the impact of different parameters on the ice accretion from the FENSAP-module, a parameter study was set up on the cylinder.

To evaluate the impact of velocity, multiple *FENSAP* runs was conducted. The resulting ice accretions can be seen in figure 3.13.

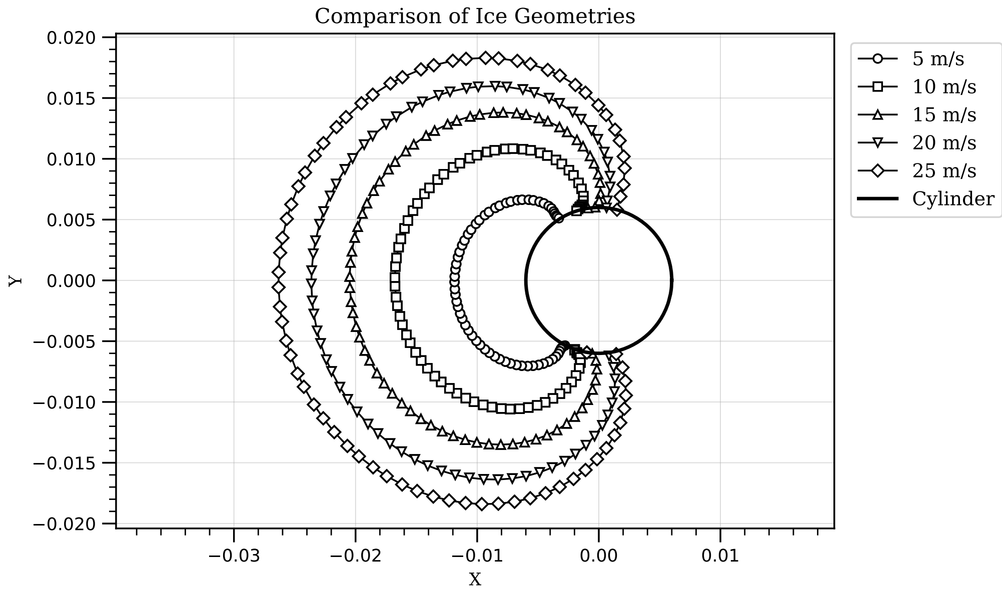

Figure 3.13 Impact of Velocity on Ice Accretion

It can be noted that the velocity greatly impacts the amount of ice growth, which is reasonable as a higher velocity allows more droplets to impact the cylinder.

The influence of varying ambient temperature on the ice accretion can be seen in figure 3.14.

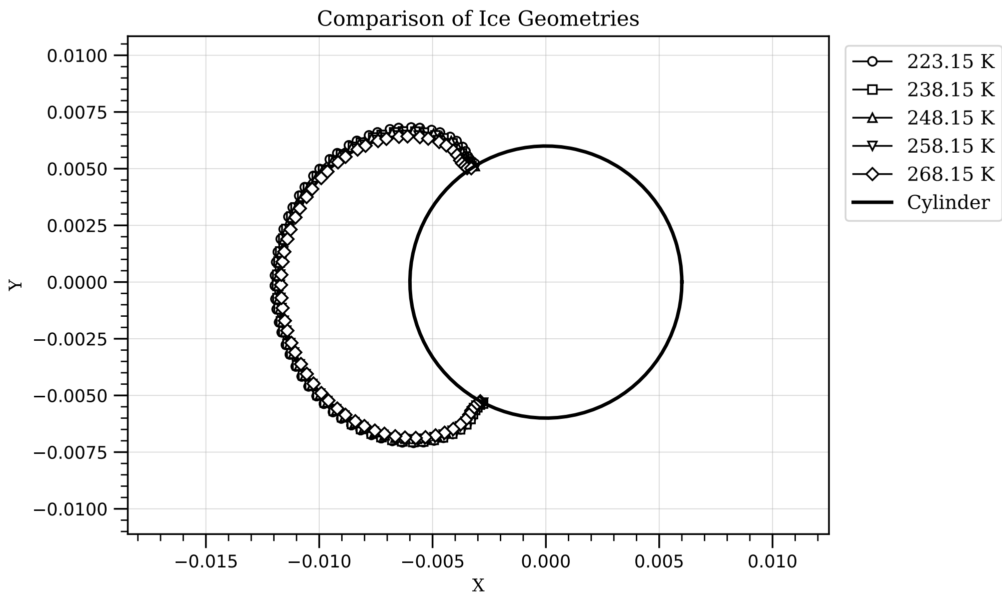

Figure 3.14 Impact of Ambient Temperature on Ice Accretion

As can be seen above, the temperature input in the *FENSAP* module has a negligible impact on the ice accretion. This is believed to be due to the flow only being affected by the temperature though a slight change in air density and viscosity. This impact is a however rather small as can be seen in figure 3.14. Note that this temperature is not linked to the ice density, which will be studied bellow.

The influence from different ice densities can be seen in figure 3.15.

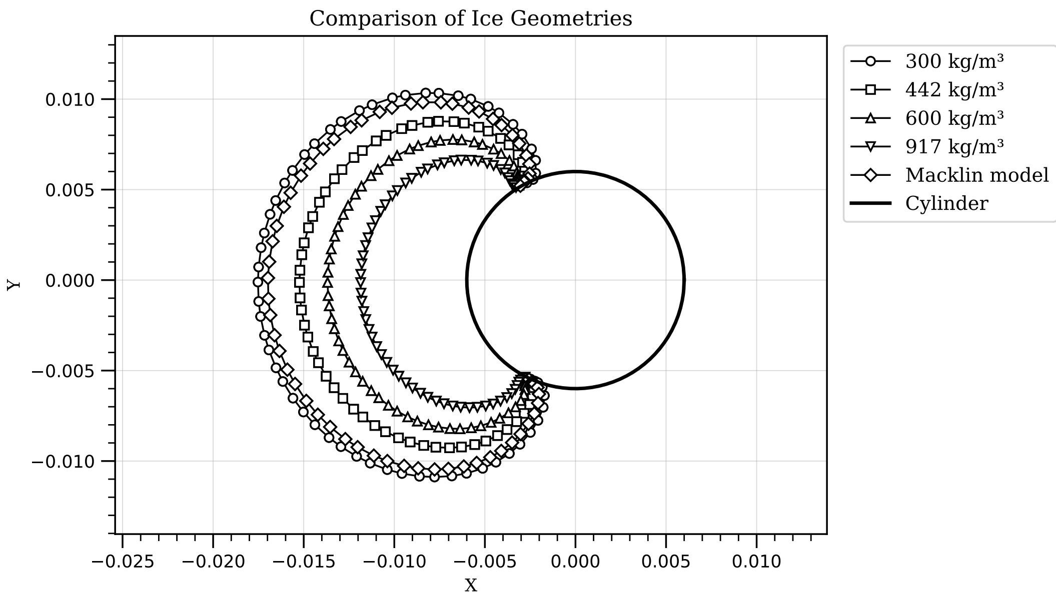

Figure 3.15 Impact of Density on Ice Accretion

As can be seen in figure 3.15, the ice density has a large impacts on the amount of accreted ice. This is reasonable as a low density and the same amount of caught mass the resulting volume has to be higher, than for a higher ice density. For the chosen wind velocity and temperature the Macklin's formula (2.15) also predicts a density in the range of soft rime according to figure 2.4, which can be seen follows the density pattern in 3.15.

The liquid water contents effect on ice accretion can be seen in figure 3.16.

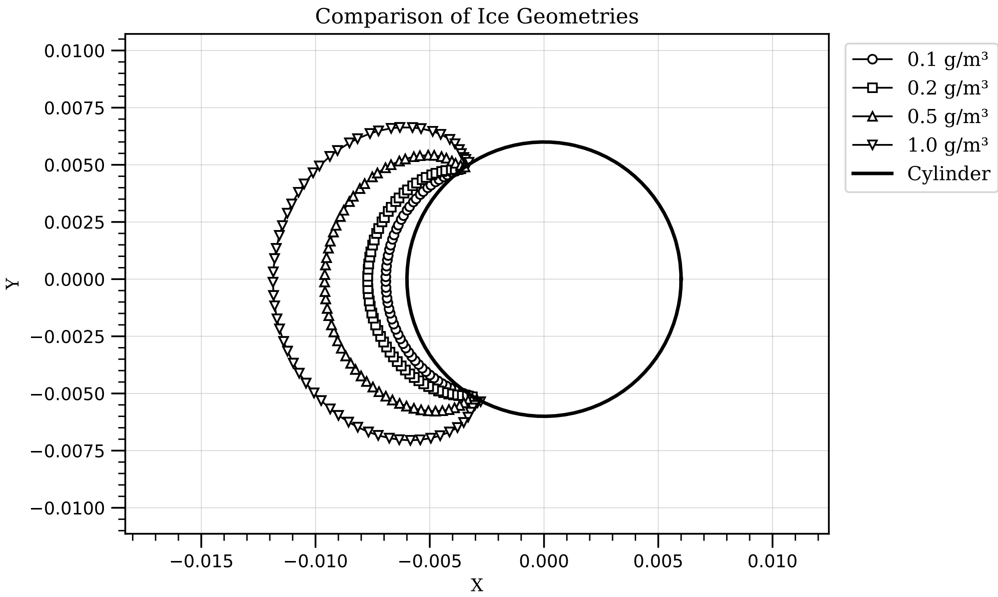

Figure 3.16 Impact of Liquid Water Content on Ice Accretion

in the figure above it can be seen that the LWC also has a significant impact on the ice volume for a LWC-range that would be reasonable at ground level in-cloud icing. The growth for larger LWC values is simply explained by a higher content of water in the air that can contribute to ice accretion.

The impact of varying median volume diameter of the droplets can be seen in figure 3.17 below.

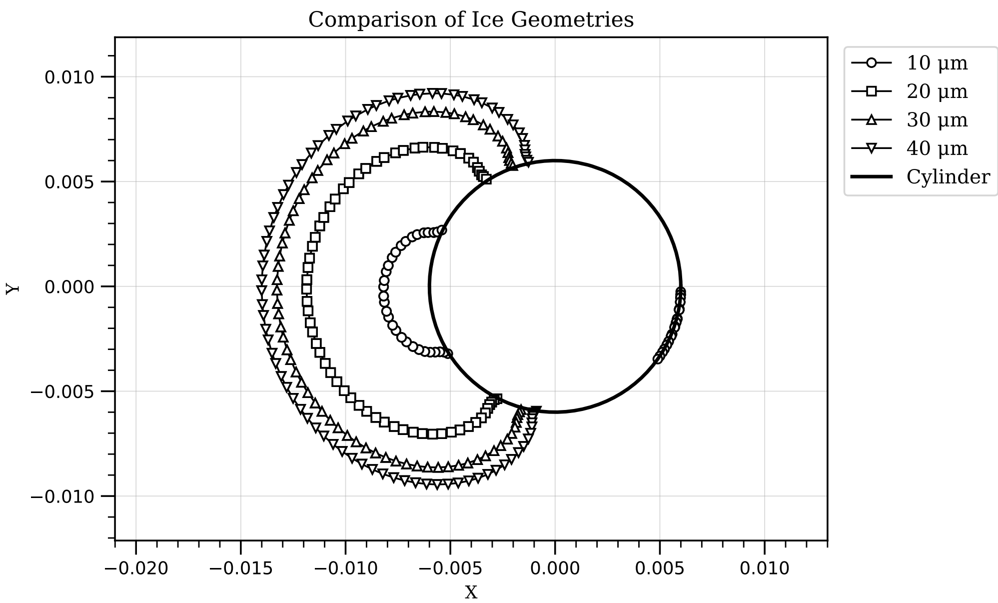

Figure 3.17 Impact of Median Volume Diameter on Ice Accretion

For the varying MVD a trend shift can be seen compared to the other tests. Similar to before a stepwise increase in volume can be noted, but for low MVDs a change in shape is also apparent on the downstream side of the cylinder. This is probably due to the fact that for 20 micron droplets, there is a probability that some droplets are able to follow the turbulent flow through the wake long enough to impact the rear of the cylinder. For larger droplets, the inertia of each particle is too large to follow the turbulent flow and show the downstream accretion.

3.8 Contact Wire Icing - Shape Study

Shape study & time dependency

To be able to construct drag coefficient plots for different iced contact wire profiles, it would be desirable if only the shape impacting parameters could be studied. For instance, if the shape of the ice only was a function of the accretion time, then it would only be necessary to calculate drag coefficients for a certain amount of accretion times independently of the chosen LWC, MVD etc. as a change of these parameters then, if independent of shape, simply could be compensated with more time.

In the following figures, the shape dependency will be examined by accreting the same volume of ice (< 0.5% deviation against the base case) for different values of the icing parameters. This, to study their impact of the ice shape.

In figure 3.18 the impact of velocity on the shape can be seen.

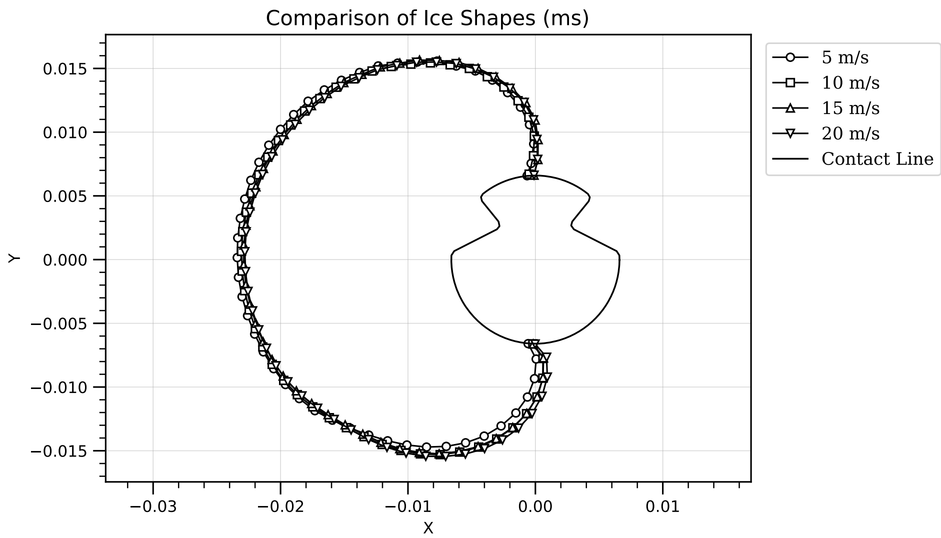

Figure 3.18 Impact of Velocity on Ice Shape

It can be noted in the figure above that the velocity has a small but not negligible effect on the shape, especially around the stagnation point and close to the point of flow separation. This is probably due to the change in turbulence at higher velocities, resulting in a different shapes.

In table 3.4, shape and icing parameters accompanying figure 3.18 can be seen. For this parameterization 20 m/s was chosen as a base case, as this velocity results in a high accretion rate.

Table 3.4 Comparison of Ice Geometry Shapes
The reference shape is indicated with bold text.

Constant parameters

Parameter	Value
Temperature	258.15 K
LWC	0.3 g/m^3
MVD	30 µm

Variable parameters

Velocity (m/s)	Area (mm^2)	ΔArea (%)	Accretion Time [s]
5	647.964	-0.341	29281
10	646.396	-0.115	14878
15	649.396	-0.121	9661
20	**650.183**	**0.000**	**7200**

Figure 3.19 shows the impact on the final shape with a varying temperature.

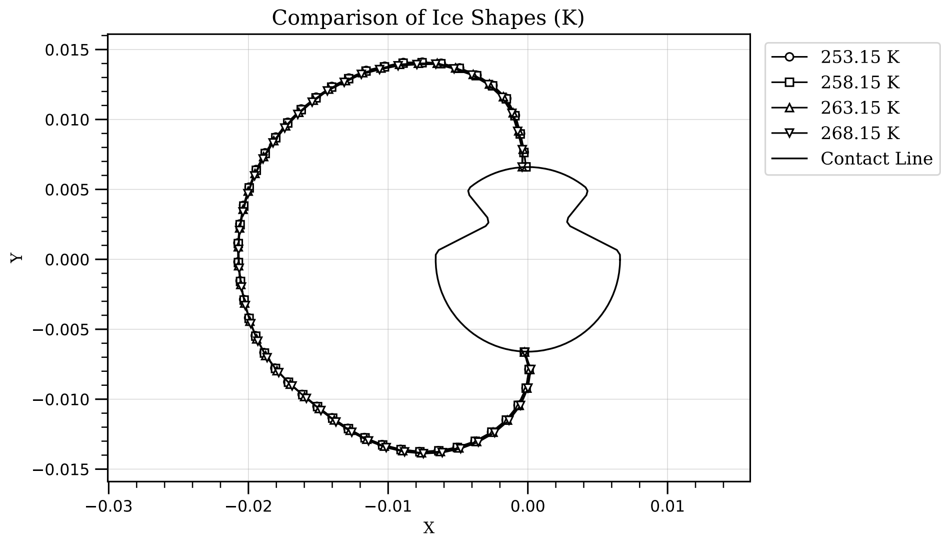

Figure 3.19 Impact of Temperature on Ice Shape

It can be seen that the temperature has an almost negligible impact on shape, probably as it only, and with a small amount impacts the density and dynamic viscosity resulting in other flow patterns. The Macklin ice density formula (2.15), was not used in the accretion found in figure 3.19.

In table 3.5 the accompanying parameters can be seen.

Table 3.5 Comparison of Ice Geometry Shapes
The reference shape is indicated with bold text.

Constant parameters

Parameter	Value
Velocity	15 m/s
LWC	0.3 g/m^3
MVD	30 μm

Variable parameters

Temperature (K)	Area (mm^2)	ΔArea (%)	Accretion Time
268.15	532.808	-0.304	8619
263.15	531.249	-0.142	7990
258.15	533.206	-0.230	7531
253.15	**534.433**	**0.000**	**7200**

Figure 3.20 shows the impact of varying LWC on the final shape.

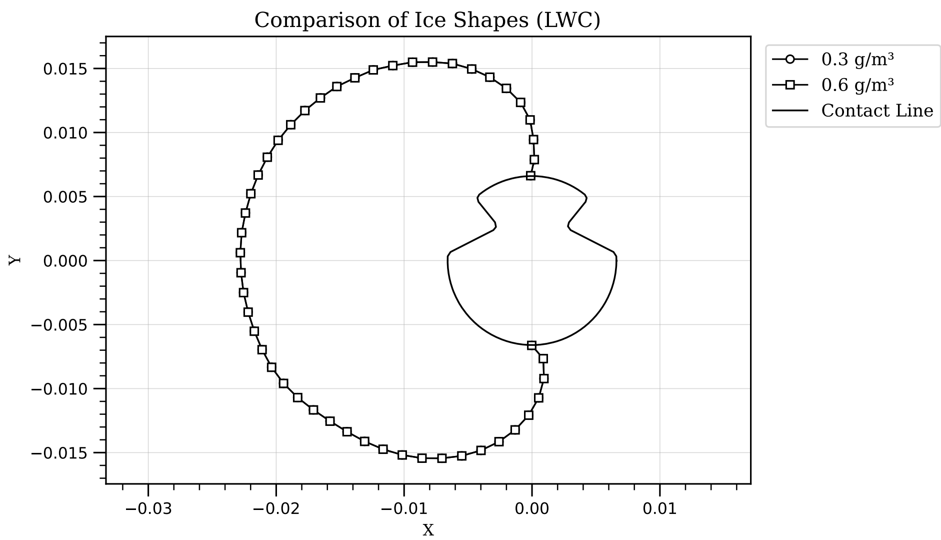

Figure 3.20 Impact of LWC on Ice Shape

It can be seen that the shapes are identical for the two LWC values, and it can therefore be concluded that LWC has no impact on the shape of the ice accretion as a halved LWC with a doubled time results in the same accretion. This is due to LWC not impacting the flow around the object, but rather only acts as a multiplier of the possible ice buildup.

In table 3.6 the accompanying parameters can be seen.

Table 3.6 Comparison of Ice Geometry Shapes
The reference shape is indicated with bold text.

Constant parameters

Parameter	Value
Velocity	20 m/s
Temperature	258.15 K
MVD	30 μm

Variable parameters

LWC (g/m^3)	Area (mm^2)	ΔArea (%)	Accretion Time
0.3	650.183	-0.000	7200
0.6	**650.183**	**0.000**	**3600**

Figure 3.21 shows the impact of a varying MVD on the final shape.

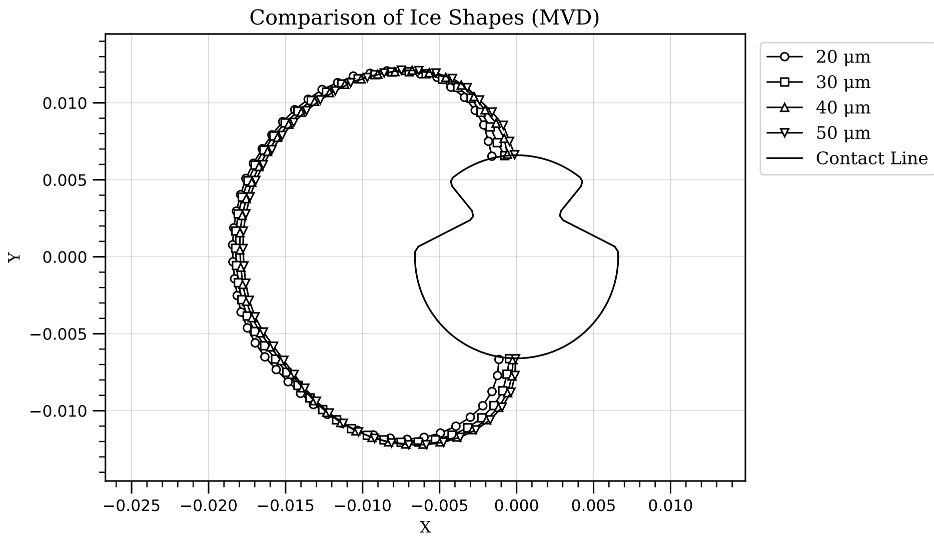

Figure 3.21 Impact of MVD on Ice Shape

It can be seen that a variation in MVD has the largest impact on the final ice shape of all the studied parameters. This was perhaps foreshadowed from figure 3.17, but is due to the same reason as described in chapter 2.6

In table 3.7 the accompanying parameters can be seen.

Table 3.7 Comparison of Ice Geometry Shapes
The reference shape is indicated with bold text.

Constant parameters

Parameter	Value
Velocity	10 m/s
Temperature	258.15 K
LWC	0.3 g/m^3

Variable parameters

MVD (μm)	Area (mm^2)	ΔArea (%)	Accretion Time
20	414.120	+0.395	9907
30	414.471	+0.480	8255
40	414.006	+0.368	7585
50	**412.490**	**0.000**	**7200**

It can now be concluded that some of the variables have a considerable impact on the ice shape. It was therefore decided that the impact of all of the variables above except LWC should be studied, as the shape could be impacted, and the drag coefficient of a certain ice volume could change. In figure 3.22 ice shapes for two different atmospheric conditions was simulated, one with moderate meteorological parameters, and one with more extreme values. Table 3.8 shows the exact parameters used in the study.

Table 3.8 Variables for Extreme and Moderate Icing Conditions

Variables	**Extreme Conditions**	**Moderate Conditions**
Velocity	25 m/s	10 m/s [1]
Temperature	248.15 K	268.15 K
LWC	1.0 g/m^3	1.0 g/m^3 [2]
MVD	40 μm	20 μm
Sand-Grain roughness [3]	1e-5 m	1e-5 m

[1] Initially 5 m/s was used, but this resulted in strange artifacts in the *ICE3D* module of *FENSAP-ICE*, which could not be used.
[2] Initially 0.1 g/m^3 was used, this however resulted in unreasonably long simulation times. To cut the time by a magnitude, the LWC was changed to 1.0 g/m^3.
[3] The surface sand grain roughness height of a clean contact wire.

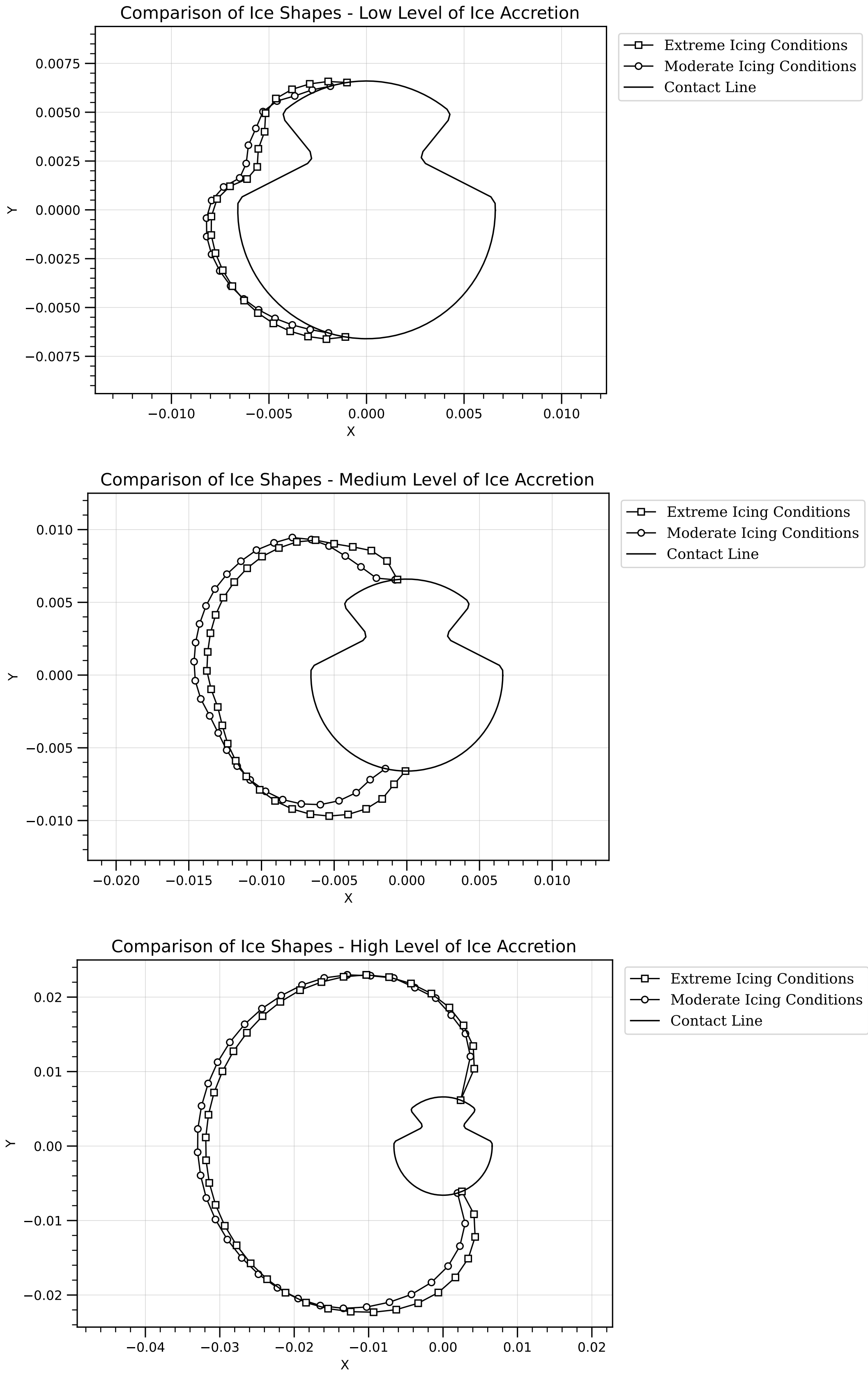

Figure 3.22 Impact of Varying Icing Conditions on Ice Shape for Small, Medium, and Large Ice Accretions.

In figure 3.22 it can be seen that depending on the icing conditions, the shape can vary quite a bit. It also seems that the difference in shape is largely dependent on the stage of accretion. That is if the level of ice accretion is low, medium or high. To further understand the impact of the different shapes, fluid simulations in *FLUENT* was conducted with the parameters as shown in table 3.9.

Table 3.9 Input parameters for *FLUENT* simulation

Input Parameter	Value
Inlet velocity [m/s]	25
Temperature [K]	258.15
Sand-grain roughness [m]	None

The drag coefficient was plotted for the different conditions and levels of ice accretion respectively, which can be seen in figure 3.23.

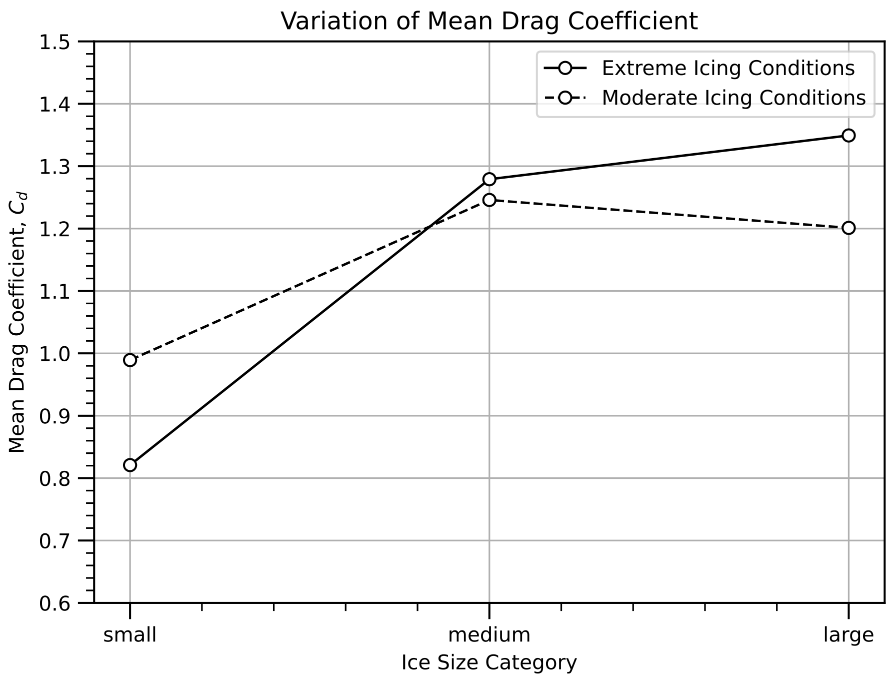

Figure 3.23 Impact of Ice Size, and Icing Conditions on the Drag Coefficient

From figure 3.23 it can be concluded that the conditions during which the ice was created has a noticeable impact on the forces acting on the iced contact wire. This means that C_d is weather dependent and therefore should be calculated for multiple icing conditions. Onward, it was decided that the "extreme" and "moderate" icing conditions gave a sufficient resolution in shape difference, and will both be used.

Contact wire surface roughness

In section 3.6 the variation of drag coefficient as a function of surface roughness was studied for a clean cylinder. How the choice of surface roughness impacts an iced (50mm^2, see figure 4.2) contact wire was also studied for different sand-grain roughnesses. The gray area marked in figure 3.24 is the possible roughness domain that can be acquired through the Shin et al. formula according to equation 2.23 with any combination for the given intervals in table 3.10.

Table 3.10 Range of varying icing parameters for surface roughness calculations

Variable	Range	Unit
Temperature (T)	$-5 > T > -30$	[°C]
Chord length (c)	$0,05 > c > 0,0182$	[m]
Liquid Water Content (LWC)	$1 > LWC > 0,1$	[g/m^3]
Median Volume Diameter (MVD)	$50 > MVD > 10$	[μm]

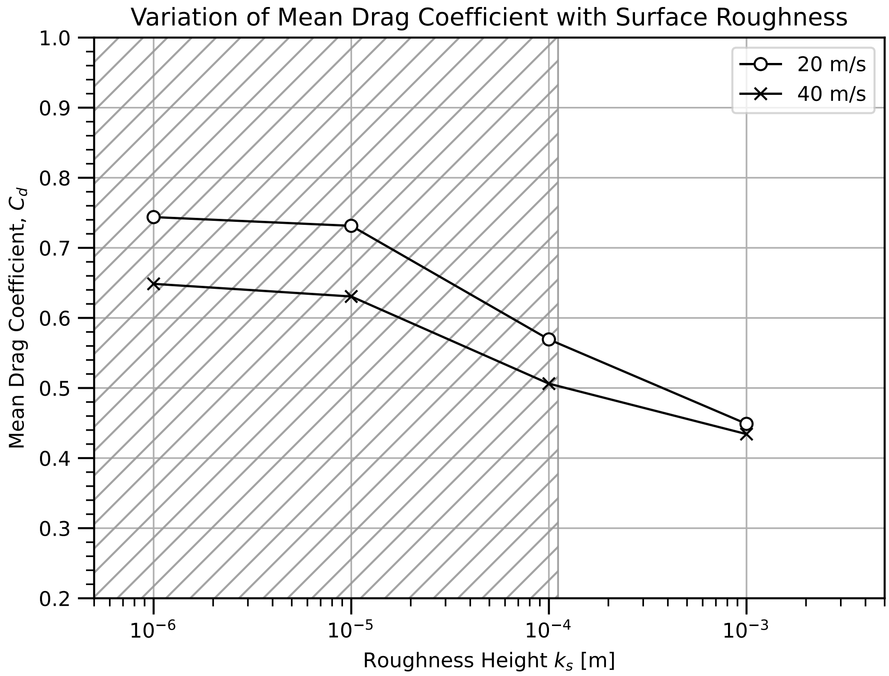

Figure 3.24 Impact of Surface Roughness on C_d for Contact Wire

It can be seen in figure 3.24 that, depending on which surface roughness is used, which in turn depends on the conditions under which the ice was created, has a large impact on the drag coefficient. The drag coefficient does not change for a smaller sand-grain roughness value of 10^{-5}. Therefore, in the final simulations of iced contact lines a constant surface sand-grain roughness value will be set to 10^{-5} for the iced wires.

Final simulations

With the sensitivity analyses complete the final simulations were conducted. At first the 12 mm cylinder case in *FLUENT* was once again examined to see whether the simulations converges to reasonable results. Two cases with URANS, where $k-\omega$ SST and Transitional SST was used as the turbulence models, and one case with LES (WALE as the SGS model) was studied. The results can be seen in figure 4.1.

Thereafter the final ice simulations in *FENSAP-ICE* was carried out. Both the extreme icing conditions and moderate icing conditions mentioned in table 3.8 was used to generate ice shapes of the same arbitrarily picked cross-sectional areas (20, 50, 100, 190 and 290 mm^2). The new ice diameters and cross-sections can be seen in the results section in the tables 4.1 & 4.2 and in the figures 4.2 & 4.4 respectively.

With the chosen iced contact wires, the geometries was transferred into *FLUENT* with the same meshing setup that was decided on during the domain analysis in section 3.2 and mesh sensitivity analysis in section 3.3.

Fluid simulations, with both URANS ($k - \omega$ SST as the turbulence model) and LES, was then carried out on the clean and iced profiles to measure the resulting drag coefficients at different velocities. The parameter setup was as shown in table 3.11.

Table 3.11 The final parameter setup used in *FLUENT*

Final *FLUENT* setup		
Parameter	Value	Unit
Turbulence model	k-ω SST / LES [1]	–
Inlet Velocity	{Varying}	m/s
Velocity Direction	[1,0,0]	–
Turbulence Intensity	5	%
Turbulent Viscosity Ratio	10	–
Inlet Temperature	258.15	K
Surface Temperature	258.15	K
Surface Roughness	1e-5 / N/A [2]	m
Solver Scheme	SIMPLEC	–
Skeweness Correction	5	–
Discretization	Second-Order	–
Residual Limit [all]	1e-5	–
Time Step Size	1e-4	s
Total Flow-Time	0.15 / 5 [3]	s
Max Iterations/Time Step	100 / 20	–

[1] Both URANS simulations and LES was used.
[2] *FLUENT* does not accept any input on surface roughness when LES is enabled, the value was therefore automatically put to zero.
[3] The flow time was 0.15 seconds for URANS and 5 seconds for LES for accurate readings of the drag coefficients.

The final results can be seen in figures 4.3a, 4.3b, 4.5a and 4.5b in the results section.

Wind Tunnel Validation

The wind tunnel used to validate the simulations is a retired "demonstrational" wind tunnel acquired from the Swedish *Armed Forces Technical School* (FMTS) but is currently owned by the *School of Aviation* at Lund University. The tunnel is an open-circuit wind tunnel and consists of an inlet section, a test section and a diffuser section as marked in figure 2.7. The turbine is powered by an frequency controlled 380/440 volts, 8 amperes, 3 phased 50 Hz motor. The test section is dimensioned $600\,mm \times 450\,mm \times 1000\,mm$. The measurements are acquired through a set of levers in the test section connected to K-25 load cells. The load cells are in turn connected to an *ALMEMO 2590-9* data logger, which also is connected to a pitot tube capable of measuring static and dynamic pressures. The setup as a whole can be seen in figure 3.25

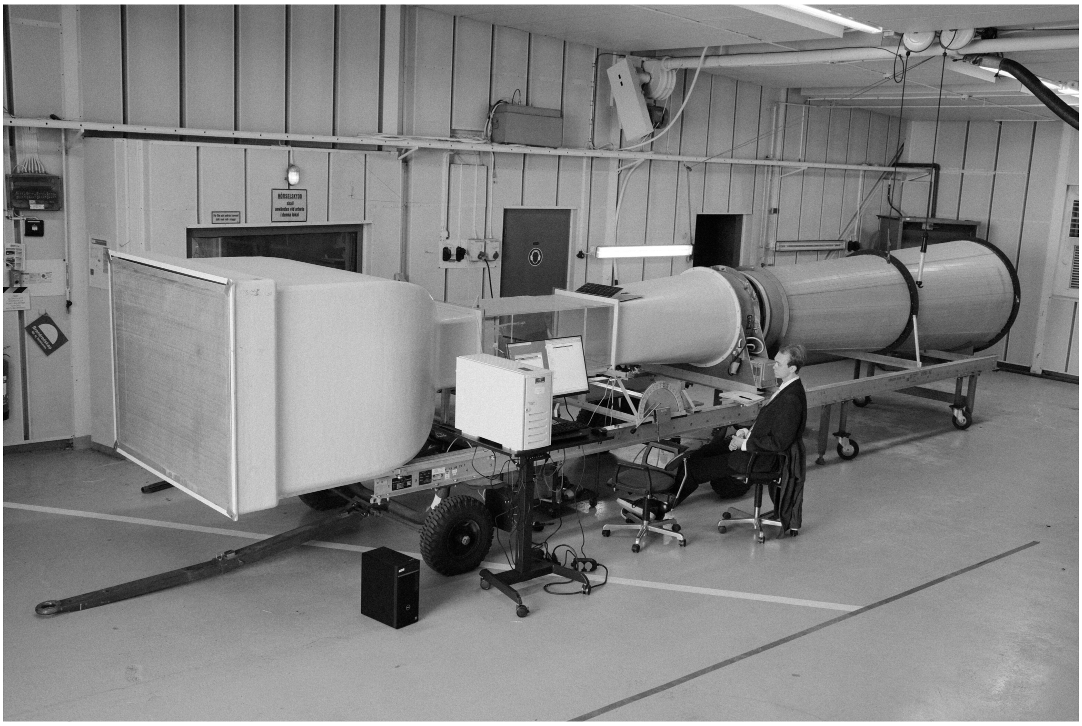

Figure 3.25 Complete Wind Tunnel Setup

To calibrate the wind speed, an external pitot tube connected to a micromanometer was deployed to measure the wind speeds by using Bernoulli's equation (2.31). This was mounted through an opening underneath the test object as can be seen in figure 3.26.

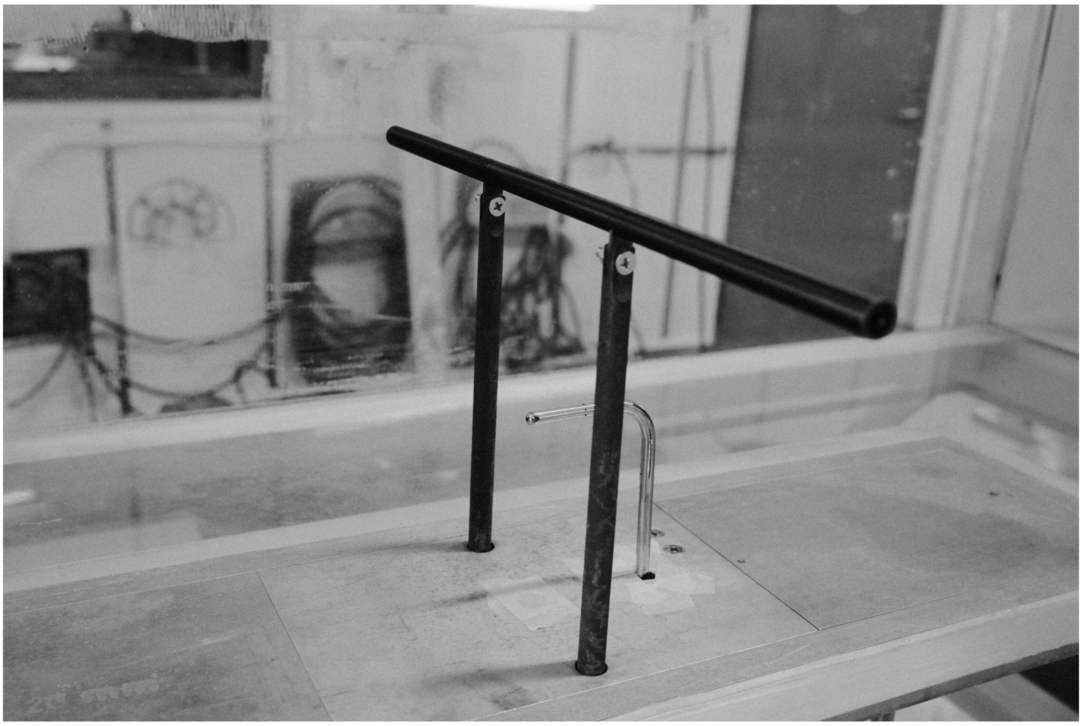

Figure 3.26 Pitot Tube Calibration with a 12 mm Cylinder Model Mounted

To calibrate the load cells measuring the drag forces, a pulley mounted setup was used, which can be seen in figure 3.27.

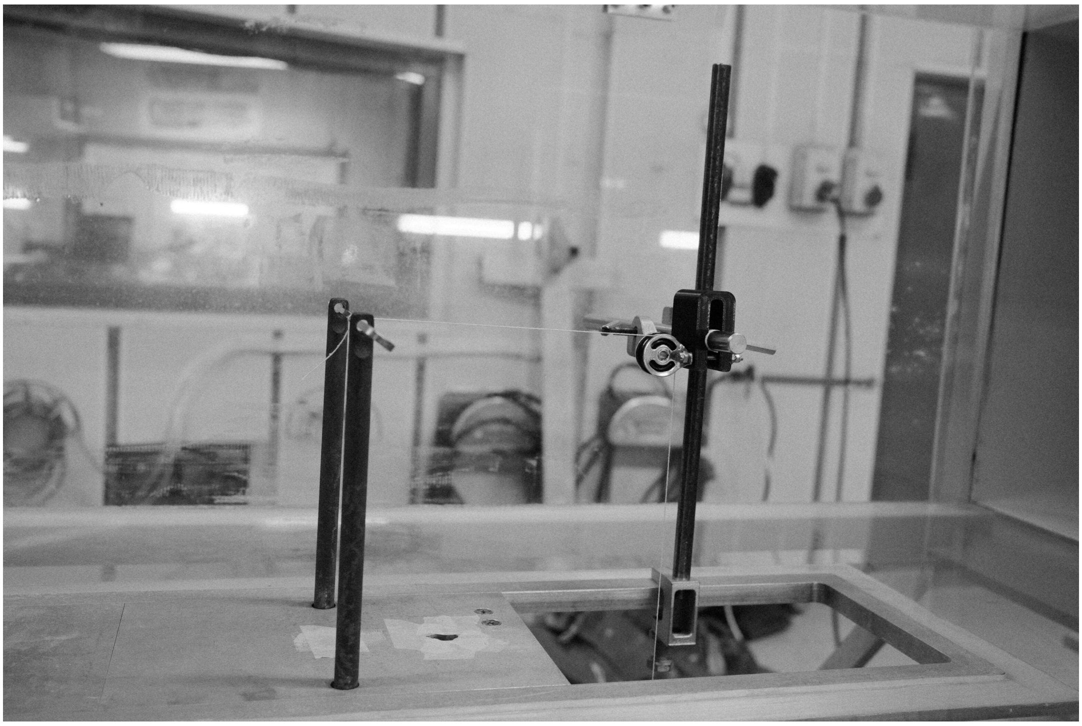

Figure 3.27 Load Cell Calibration with a Pulley System

The calibration results can be found in appendix under section A.

With the calibration complete, 3D-printed models of two cylinders (12/24 mm diameter), a clean contact wire and the iced contact wires under extreme conditions (see figure 4.2) was produced. The models was printed out in a 1:1 scale and with a total width of 400 mm which leaves a maximum blockage ratio of 3.61 % for the test cross-section. The available 3D-printers could not print out the entire length of 400 mm so the models had to be printed out in three segments and glued together. The models could then be mounted as seen in figure 3.26.

To ensure reliable readings where tip effects are not impacting the results, circular end-plates was laser cut from acrylic. The force and velocity data for the 12 mm cylinder and clean contact wire, both with and without the circular end-plates was then examined. See figures 3.28 and 3.29 for the schematic setup with end-plates.

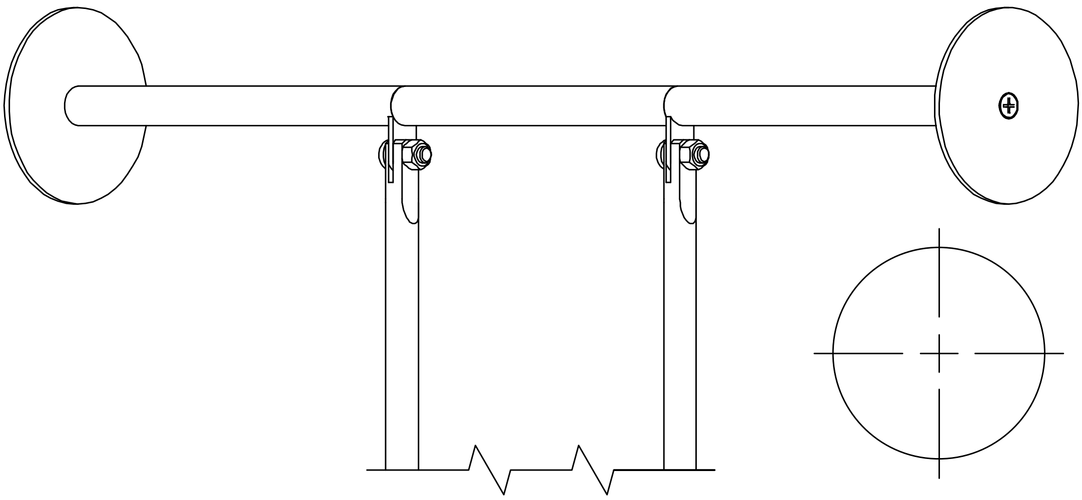

Figure 3.28 Schematic of the 12 mm Cylinder Setup with End-plates

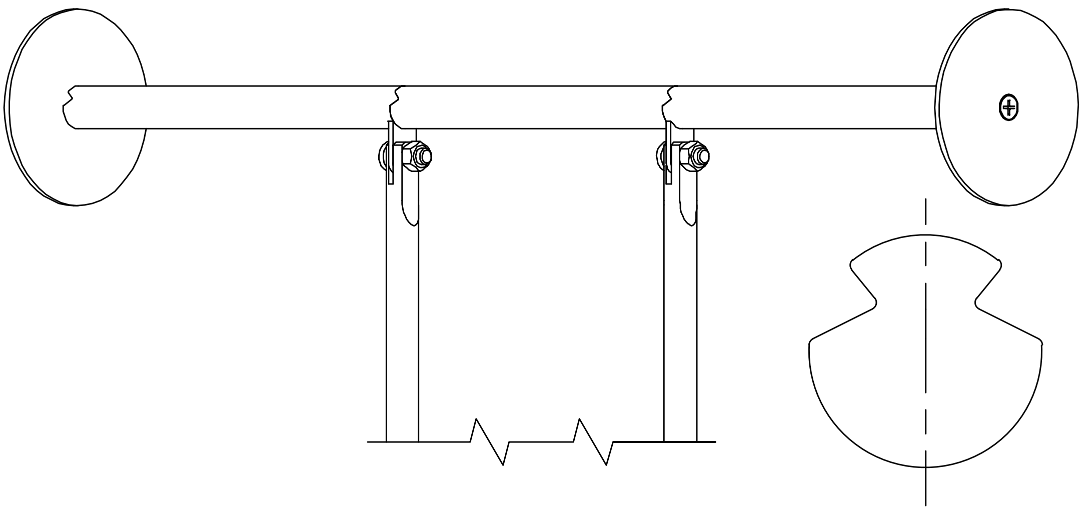

Figure 3.29 Schematic of the Clean Contact Wire Setup with End-plates

The results from the experiments can be seen in figure 3.30.

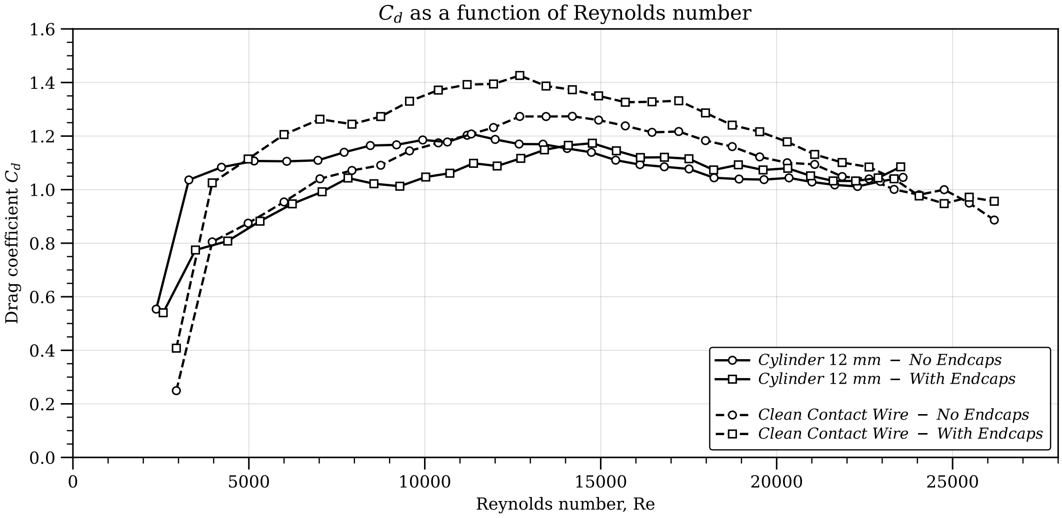

Figure 3.30 Wind Tunnel Drag Coefficient Plots for a 12 mm^2 Cylinder and Clean Contact Wire with and without End-plates.

It can be seen that the end-plates for the contact wire added to the force, most likely through the increased surface area. In the case for the cylinder however the end-plates reduced the force. This may mean that the end-plate reduced end effects for the cylinder but not the contact wire. This discrepancy raises the question whether or not to use end-plates. The final decision was that the upcoming experiments should be conducted without end-plates entirely as the additional force generated by the end-plates could not be estimated in a reliable way.

After the examination of tip effects, the force data was collected for all the 3D-printed models without end-caps for the full range of wind speeds. This was done by successively increasing the velocity and logging the drag force, and the results can be seen in section 4.1.

3.9 Meteorological Dependencies

As weather changes on hourly basis, if not more rapidly, it becomes difficult to establish if ice was created with certain constant parameters (velocity, temperature, MVD etc.). Especially when ice accretion can occur during periods of up to weeks and stay on wires for months if not artificially removed. It becomes even more difficult when wind gusts not related to the initial accretion can cause mechanical failure at a even later stage. A possible way to circumvent this problem is to separate the accretion mechanisms from the mechanical loading. In the methodology chapter, a great deal of work was carried out to determine what wind loading factors which could be expected from a certain cross-section of accreted ice. In the following section a method to approximate the amount of accreted ice is proposed.

From figure 3.31, maximal wind velocities as well as minimum temperatures ("Cold-loads") retrieved from the *Swedish Building Regulations* (BFS 2011:10) are shown [5]. These maps are issued by *Boverket*, the Swedish National Board of Housing, Building and Planning, and are used for the dimensioning of buildings and structures in Sweden. As can be seen from the maps, it is of great relevance that the geographical variations are taken into consideration. As there is a large variance within the country. If a conservative constant wind-load is assumed over the entire country, it could result in unnecessary costs in some parts of the country due to over-dimensioning. On the other hand, if an average is used, some structures could risk failure in other areas. In the following chapter a great deal of effort is conducted to estimate different parameter's dependencies on a set of key-parameters most relevant for ice accretion.

Research regarding under which meteorological parameters ice accreted at, is an active field, and subsequently it has been difficult to find good sources on how to approximate different values. This has been an attempt to quantify icing parameters, but further studies should be conducted to refine these models.

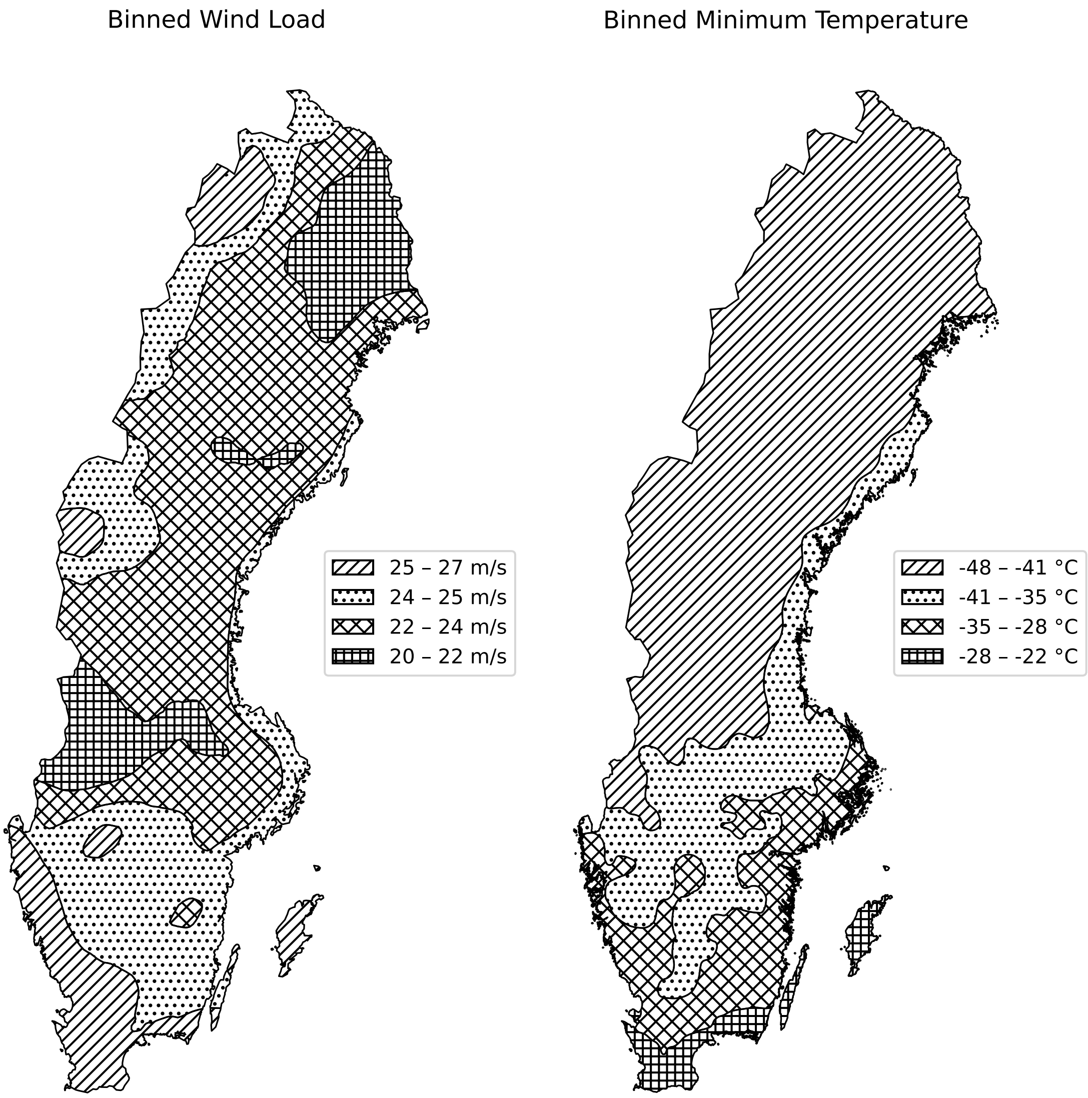

Figure 3.31 Maximum Wind Speeds and Minimum Ambient Temperatures in Sweden with a 50 Year Return Period [5]

.

Meteorological MVD & LWC dependencies

To determine how MVD and LWC varies with other meteorological parameters such as wind speed and temperature is no easy task, and a lot of recent articles on the field looks to describe these relationships in a local context. Often by using vast amounts of collected data together with machine learning algorithms [12]. As of today no established formula or algorithm of this kind exists, but research is ongoing and can for instance be found in IWAIS 2024 [14].

The next best meteorological studies for our use is focused towards the aviation industry, aimed to refine simulations and predictions of icing on airfoils and aviation structures. The data found in the "Aircraft Icing Handbook" [9], proposes a temperature dependence of both LWC, and MVD. In lack of better alternatives this data was used in our study.

However it should be revised if better, and more local measurements are made, intended to be used for ground structures.

The functions for LWC and MVD found in the "Aircraft Icing Handbook" [9] was fitted according to figure 3.32 and 3.33. The fitted function represents the envelope of gathered data, and subsequently gives an outline of the most extreme values. The raw data which is taken by eye from the source and the fitted function can be found in appendix in table A.2 & A.3.

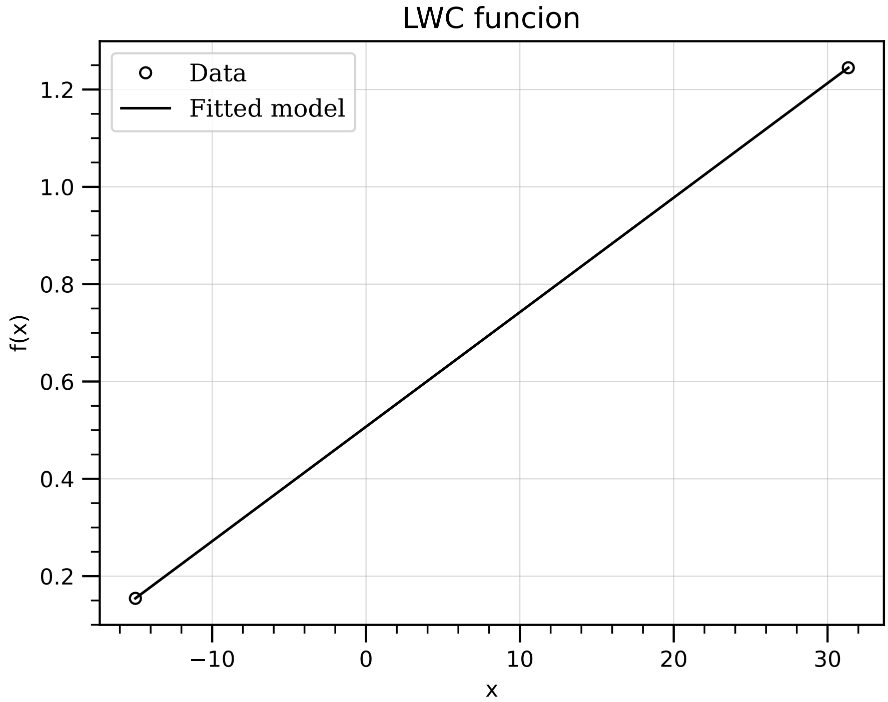

Figure 3.32 LWC Function Fitted from Data Found in Literature [9]

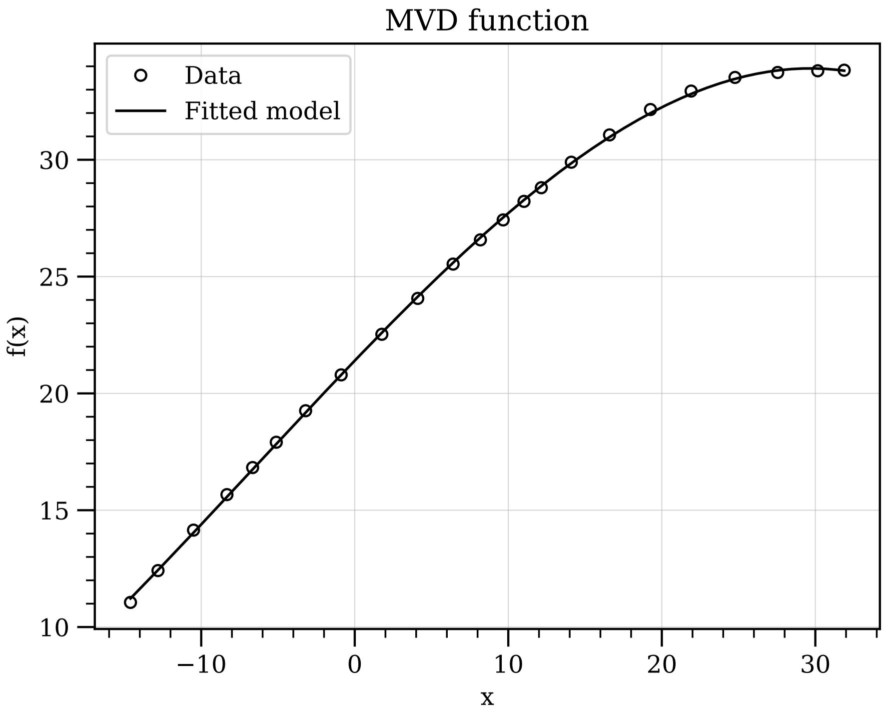

Figure 3.33 MVD Function Fitted from Data Found in Literature [9]

Ice density dependencies

The ice density can be described by Macklin's formula (2.15):

$$\rho_{ice} = 0.378 + 0.425 log_{10}(R_m) - 0.0823(log_{10}(R_m))^2$$

where R_m is the Macklin's parameter 2.16:

$$R_m = -\frac{v_0 d_m}{2T_s} \qquad \text{for } 0.2 < R_m < 170$$

The Macklin's parameter consists of the droplet impact velocity v_0 [m/s], the median volume droplet diameter d_m [μm] and the mean surface temperature of the ice deposit T_s [$^\circ C$]

The median volume droplet diameter d_m can now be described by the relationship found in figure 3.33 above. The mean surface temperature is assumed to have the same temperature as the ambient temperature.

The droplet impact velocity is in turn described by Blodgett & Langmuir's formula as shown in equation (3.1) [18]:

$$v_0 = \begin{cases} v\left(-0.174 + 1.464K_0 - 0.816K_0^2\right), & \text{if } K_0 \leq 0.55 \\ v\left(0.561 + 0.592\log_{10}(K_0) - 0.26\log_{10}(K_0)^2\right), & \text{if } K_0 > 0.55 \end{cases} \tag{3.1}$$

where

$$K_0 = \frac{K}{0.087 \cdot Re_d^{0.76\, Re_d^{-0.027}} + 1}, \tag{3.2}$$

and

$$K = \frac{\rho_w \, v \, d^2}{9 \mu D} \tag{3.3}$$

$$Re_d = \frac{\rho_a \, d \, v}{\mu} \tag{3.4}$$

Where the inertia parameter, K and the droplet Reynolds number, Re_d are defined by:

ρ_w is the density of water $[kg/m^3]$
ρ_a is the density of air $[kg/m^3]$
v is the free stream velocity $[m/s]$
d is the median volume droplet diameter $[\mu m]$
μ is the absolute viscosity of air $[Pa \cdot s]$
D is the characteristic length of the iced object $[m]$ [1]

If the air is humid (or contains ice particles) the density ρ_a is further dependent on the temperature and relative humidity, this can be derived by using Dalton's law (2.28) and the ideal gas law (2.27). The density of humid air can be written as:

$$\rho_{tot} = \frac{m_{tot}}{V} = \frac{m_a + m_w}{V} = \rho_a + \rho_w \tag{3.5}$$

By substituting ρ_{tot} and ρ_w with the ideal gas law (2.27), equation (3.5) can be rewritten as:

$$\rho_{tot} = \frac{p_a M_a}{RT} + \frac{p_w M_w}{RT} \tag{3.6}$$

The partial pressure of air in equation (3.6) can now be rewritten using Dalton's law (2.28) as:

$$\rho_{tot} = \frac{(p_{tot} - p_w) M_a}{RT} + \frac{p_w M_w}{RT}$$

which can be restructured as:

$$\rho_{\text{tot}} = \frac{p_{\text{tot}} M_a}{RT} \left(1 - \frac{p_w}{p_{\text{tot}}} \left(1 - \frac{M_w}{M_a}\right)\right) \tag{3.7}$$

[1] This variable should be updated depending on the amount of ice accreted. In this study it is however set to the nominal diameter.

And with the definition of relative humidity:

$$\phi = \frac{p_w}{p_{sat}} \tag{3.8}$$

Equation (3.7) can finally be written as:

$$\rho_{\text{tot}} = \frac{p_{\text{tot}} M_a}{RT} \left(1 - \frac{\phi p_{sat}}{p_{\text{tot}}} \left(1 - \frac{M_w}{M_a}\right)\right) \tag{3.9}$$

Then Theten's equation (2.29) can be used to approximate p_{sat} at different temperatures.

Furthermore, the absolute viscosity of air has a temperature dependence described by Sutherland's law (2.26) as:

$$\mu = \mu_0 \left(\frac{T}{T_0}\right)^{\frac{3}{2}} \frac{T_0 + S}{T + S}$$

Finally if everything is implemented together, the ice density ρ_{ice} can be calculated only from temperature, velocity and relative humidity, which then can be used to describe the volumetric ice accretion. Note: ρ_w is here assumed to be independent of temperature.

Collision efficiency dependency

To accurately predict the distribution and amount of ice accretion, the collision efficiency (CE) for a given geometry needs to be calculated using experiments or simulations. *DROP3D* in *FENSAP-ICE* has the ability to simulate the collision efficiency for an object. CE values are then extracted for the temperature and velocity range of interest. As a reference, the exported files contains values giving curves similar to figure 3.34.

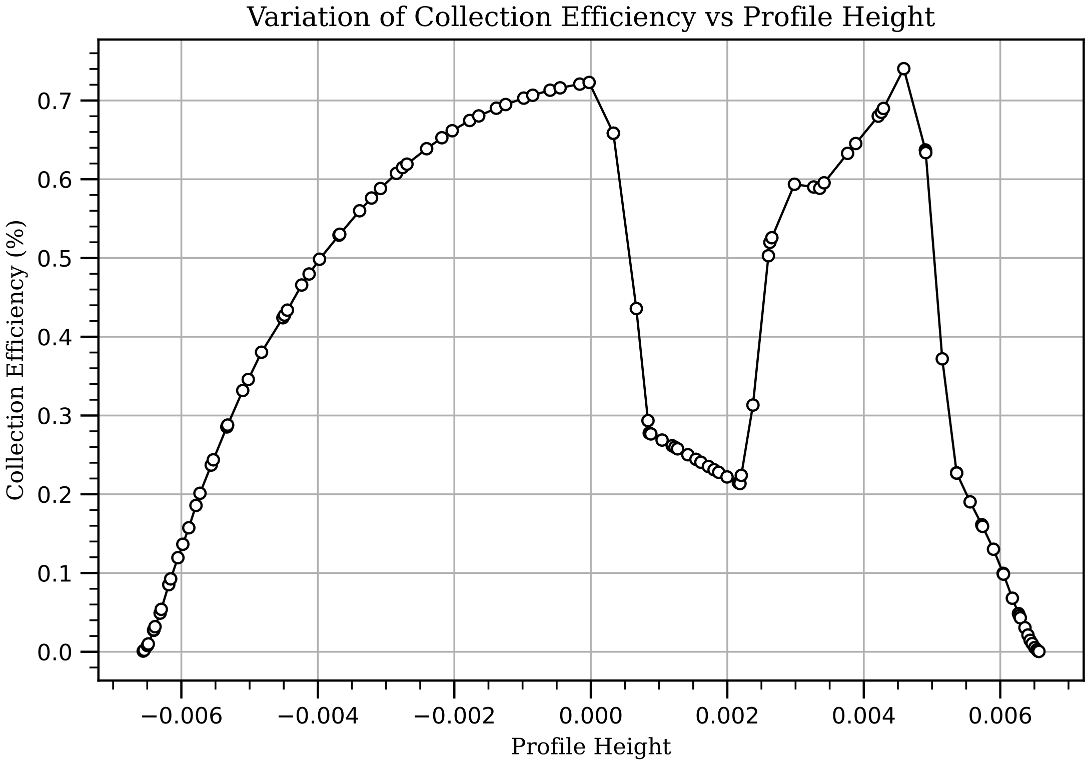

Figure 3.34 Collision Efficiency of a Iced Contact Wire

If the mean collision efficiencies are calculated for a temperature and velocity range of interest, a CE surface can be created. This surface can be found in the results chapter. Mean collision efficiency values for a range of velocities and temperatures can be found in appendix in table A.1.

Mass and volume accretion

According to Makkonen's formula (2.30) the icing rate can be described as:

$$\frac{dM}{dt} = \alpha_1 \cdot \alpha_2 \cdot \alpha_3 \cdot w \cdot v \cdot A$$

For rime ice, empirical observations show that $\alpha_2 = \alpha_3 = 1$ as all droplets freeze upon impact. With this assumption, the equation can be rewritten as:

$$\frac{dM}{dt} = \alpha_1 \cdot w \cdot v \cdot A$$

We have previously in the chapter been able to deduce that both α_1, and w (LWC) can be expressed as functions of the velocity and temperature. This leads to the following dependency:

$$\frac{dM}{dt} = F(\alpha_1, w, v, A) = \left\{ \begin{array}{l} \alpha_1 = F(v,T,MVD) \\ w = F(v,T) \\ MVD = F(v,T) \end{array} \right\} = F(v,T,A) \tag{3.10}$$

Now when the mass rate can be calculated, the volumetric rate of ice accretion can easily be calculated as:

$$\frac{dV}{dt} = \frac{dM}{dt} \cdot \rho^{-1} \tag{3.11}$$

And as the density can be described as a function of temperature, velocity and relative humidity ϕ, the volumetric icing rate can be described as a function of:

$$\frac{dV}{dt} = F\left(\frac{dM}{dt}, \rho\right) = \left\{ \begin{array}{l} \frac{dM}{dt} = F(v,T,A) \\ \rho = F(v,T,\phi) \end{array} \right\} = F(v,T,A,\phi) \tag{3.12}$$

With this relationship established, it is possible to calculate surfaces spanning over relevant ranges of temperatures and velocities for a given relative humidity, which in our case is set to 100% as this results in the most conservative value. The surfaces can be seen in figure 4.11 in the results section.

As can be seen in equation (3.12) a feedback loop is created as the volume depends on the area which in turn depends on the volume. This is accounted for in the later created accretion curves seen in the results.

Current proceedings

If the current proceedings are compiled in a similar manner as above. The wind load can be expressed as below, according to equation (2.4):

$$Q_{WC} = q_p(z) \cdot G_C \cdot d \cdot C_C \cdot \frac{L_1 + L_2}{2} \cdot \cos^2 \Phi$$

To make the equation comparable to our results, the product describing the length is set to 1, as to describe the wind load per meter wire. Similarly the structural response factor G_C is set to 1 as we assume static wires. With these changes the wind load can be described as a function of:

$$\begin{aligned} Q_{WC} = F\left(q_p(z), d, C_C\right) = \left\{ \begin{array}{l} q_p(z) = F(TC, v) \\ d = F(d_n, g_{IK}, \rho_I) \\ C_C = F(IC, C_{d,orig}) \end{array} \right\} = \\ = F\left(TC, IC, C_{d,orig}, v, d_n, m, \rho_{ice}\right) \end{aligned}$$

Where

TC is the terrain category as described in table 2.4 $[-]$

IC is the ice class as described in table 2.3 $[-]$

$C_{d,orig}$ is the reference C_d according to table 2.6 $[-]$
v is the velocity $[m/s]$
d_n is the nominal diameter $[m]$
g_{IK} is the characteristic ice load according to table 2.3 $[kg]$
ρ_{ice} is the ice density $[kg/m^3]$ [8]

3.10 Additional Surface Roughness Experiments

This section is devoted to the methodology regarding experiments that was conducted after the main-results was presented, but still is of interest to further studies.

Due to logistical reasons a sample of a contact wire was delivered late in the process so any actual readings with the wire could not be done before all simulations and experiments already were conducted.

However one experiment that was conducted was to measure the actual surface roughness of the contact wire and the 3D-printed models. To do this a focus stacking method with a digital microscope was used. The method works by obtaining focus on the lowest part of the surface. Then by slowly increasing the height of the microscope, and thus changing the point in focus, it takes multiple pictures until the highest point on the surface is in focus. By then stacking the taken pictures, a 3D rendering of the surface is made and its equivalent R_a value is calculated.

[8] How the density should be calculated for rime according to standard TSFS 2018 [43] is rather unclear, however in ISO 12494:2017 [39], accreted ice diameters for 300, 500, 700 & 900 kg/m^3 are tabulated which can be used as guidance.

4

Results

4.1 Drag Coefficient Plots

Cylinder simulations

In figure 4.1 drag coefficient plots for 12 mm^2 cylinders can be seen, when different turbulence models are considered. The figure includes analytical experimental data for a cylinder according to Sucker & Brauer [37], as well as the results from the wind tunnel experiments.

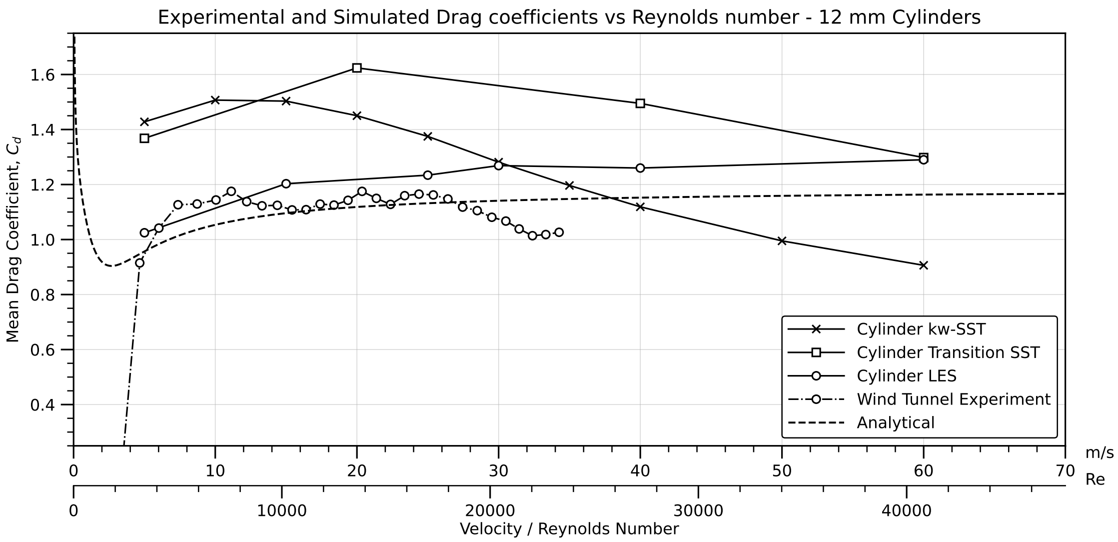

Figure 4.1 C_d as a Function of Velocity for a 12 mm Cylinder

It can be seen that a a great variation exists depending on the model used. For example, the graphs show that the LES method gives values closer to the analytical reference values. Additionally in figure 4.1 the experimental data conducted in the wind tunnel also seem to fit the analytical function in a certain range.

Contact wire simulations

In the following section, results from the ice accretion and fluid simulations on the contact wire are presented.

In table 4.1 and in figures 4.2 & 4.3 the new diameter (ice height) as well as a cross-sectional representation of the accreted ice and their corresponding C_d-plots can be seen. The icing condition used, were the *extreme icing conditions* presented in table 3.8.

Table 4.1 Ice Diameters (Heights) under Extreme Conditions Measured between the Largest and Smallest Y-value

Ice area	Height
20 mm^2	0.0132 m
50 mm^2	0.0142 m
100 mm^2	0.0164 m
190 mm^2	0.0206 m
290 mm^2	0.0244 m

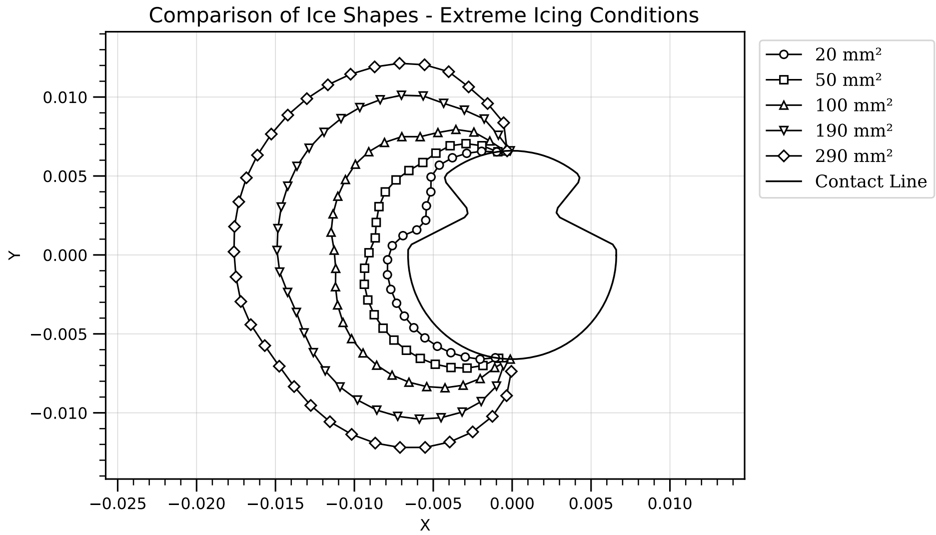

Figure 4.2 Cross-section of the Iced Contact Wire for Extreme Icing Conditions

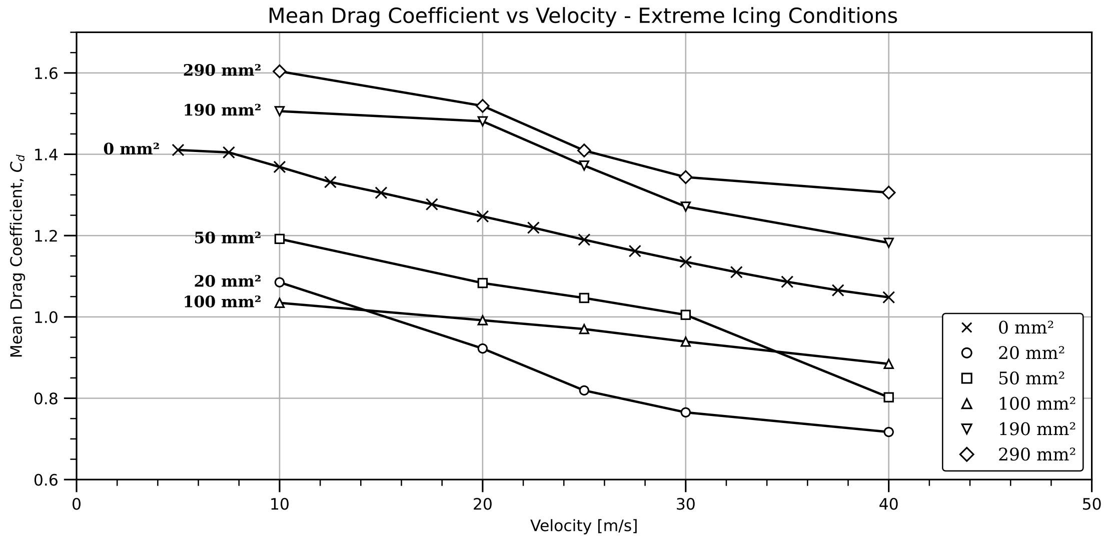

(a) C_d as a Function of Velocity for Extreme Icing Conditions - URANS

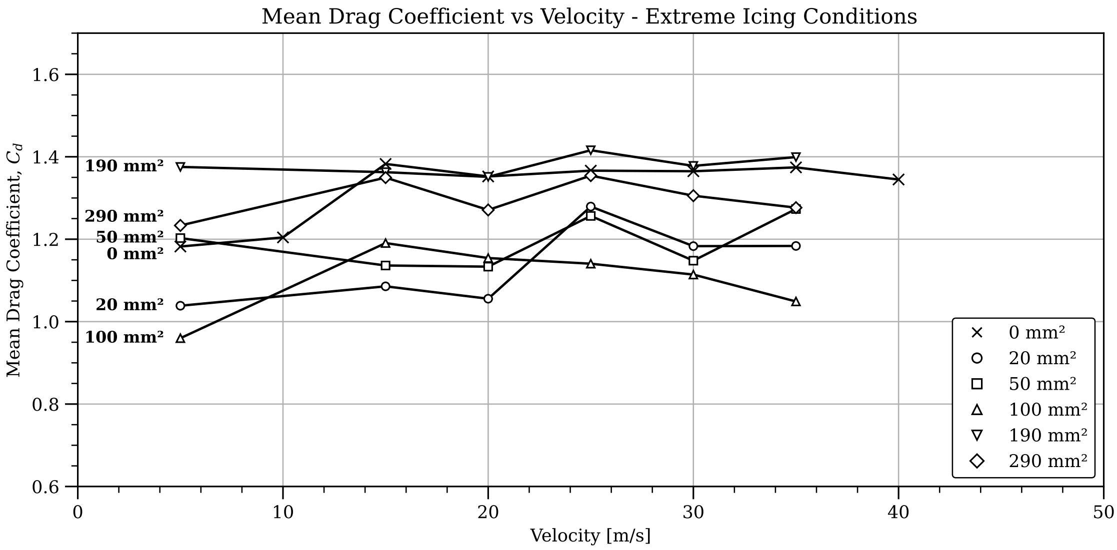

(b) C_d as a Function of Velocity for Extreme Icing Conditions - LES

Figure 4.3 Drag Coefficient Plots under Moderate Icing Conditions for (a) URANS Simulations & (b) LES

In the same manner, the new diameters, the accompanying cross-sections and their drag coefficients can be seen in table 4.2 and figures 4.4 & 4.5 for the moderate icing conditions, see table 3.8.

Table 4.2 Ice Diameters (Heights) under Moderate Conditions Measured between the Largest and Smallest Y-value

Ice area	Height
20 mm^2	0.0132 m
50 mm^2	0.0132 m
100 mm^2	0.0154 m
190 mm^2	0.0200 m
290 mm^2	0.0236 m

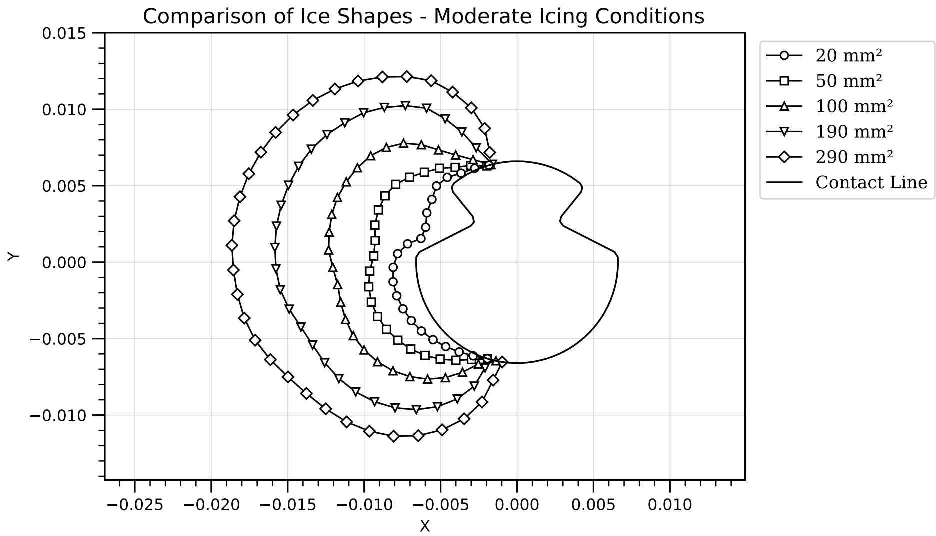

Figure 4.4 Cross-section of the Iced Contact Wire for Moderate Icing Conditions

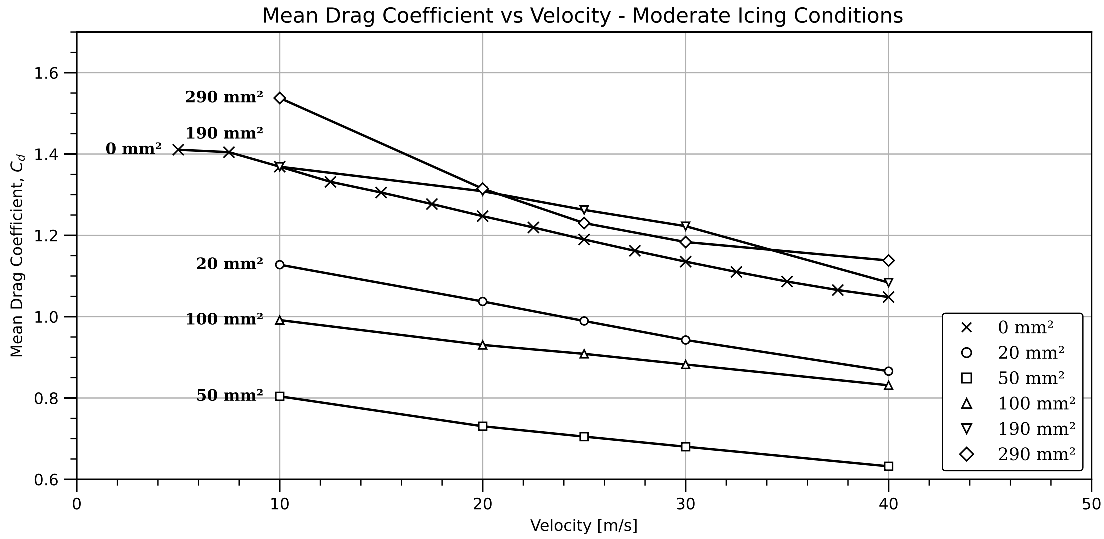

(a) C_d as a Function of Velocity for Moderate Icing Conditions - URANS

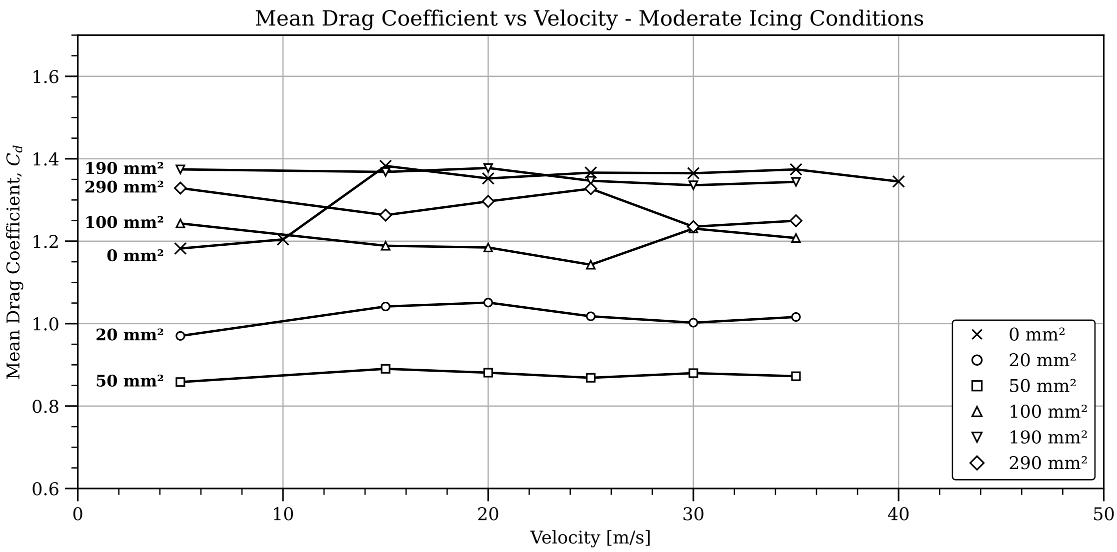

(b) C_d as a Function of Velocity for Moderate Icing Conditions - LES

Figure 4.5 Drag Coefficient Plots under Moderate Icing Conditions for (a) URANS Simulations & (b) LES

If the most conservative value for each ice area and velocity presented in figures 4.3b and 4.5b are combined, then a plot showing the dimensioning values for the drag coefficient can be made. This plot can be seen in figure 4.6.

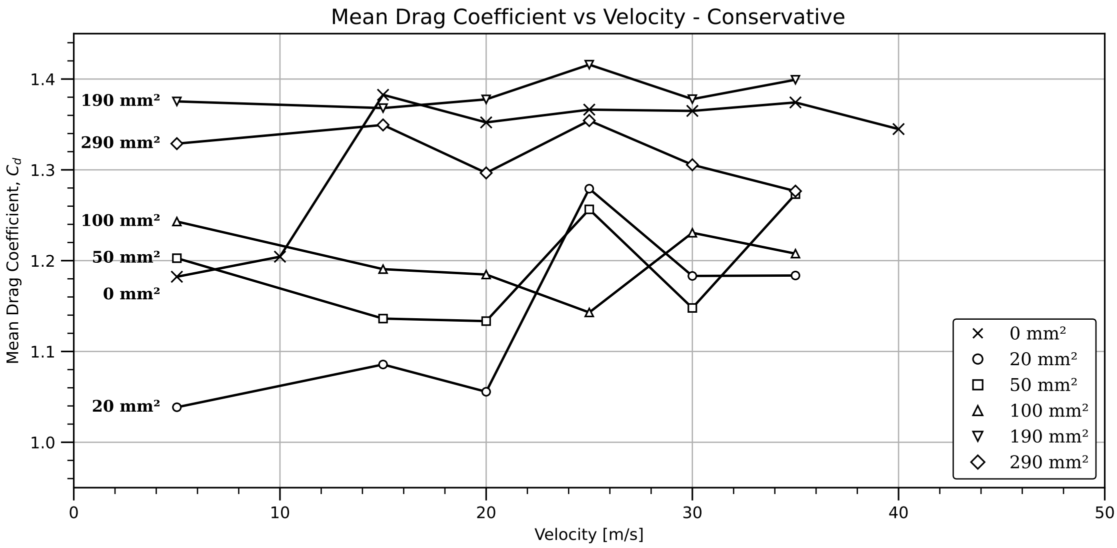

Figure 4.6 C_d as a Function of Velocity for Dimensioning Icing Conditions from LES

If figure 4.6 is expanded into the area-dimension, a surface showing the dimensioning C_d values for varying velocities and areas can be created. This surface can be seen in figure 4.7.

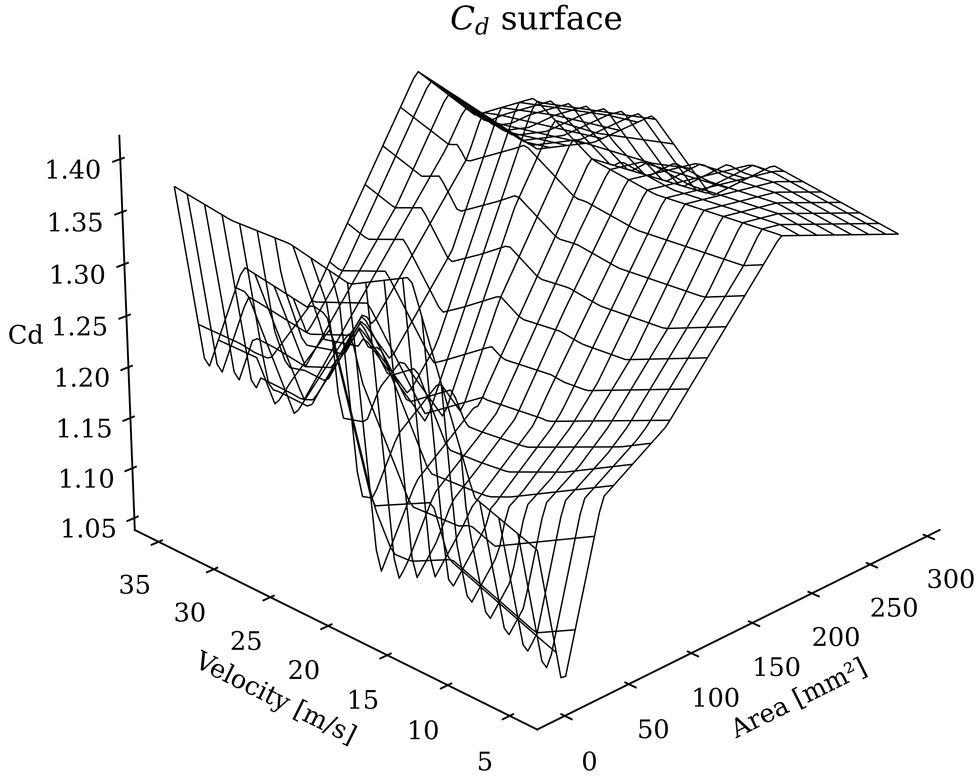

Figure 4.7 C_d-surface

In figure 4.7 it can be seen that the drag coefficient dips around a value between 20 mm^2 and 50mm ^{2}. The value then increases for an increased ice-accretion area, up until 190 mm^2 where it stagnates.

Experiments

The following section show the results from the wind tunnel experiments.

Figure 4.8 and 4.9 show the results from the wind tunnel which was collected in two sessions over two days. These two sessions will be referred to as *Run 1* and *Run 2* respectively.

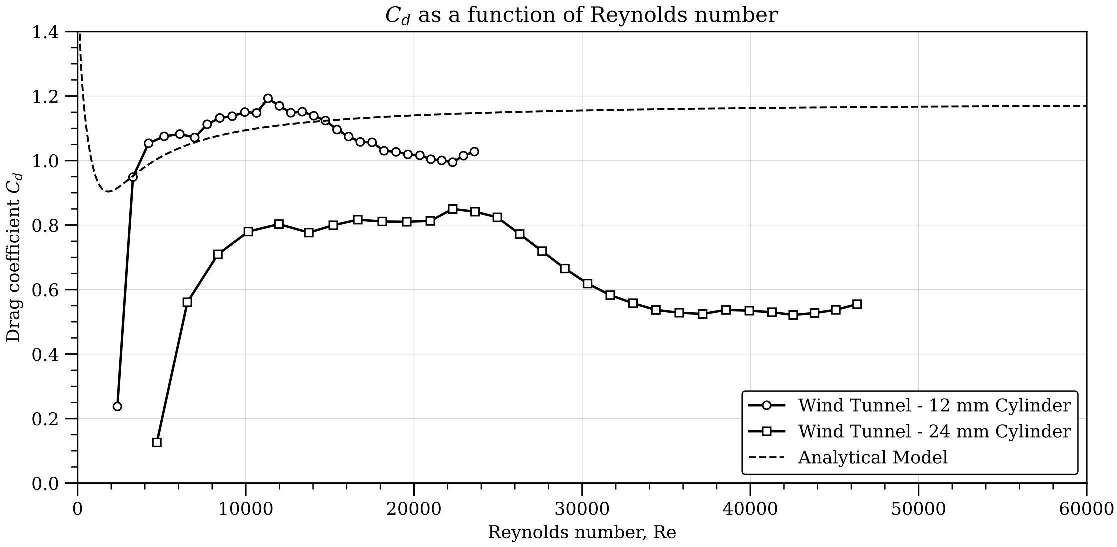

(a) Experimental C_d as a Function of Reynolds number for Cylinders - *Run 1*

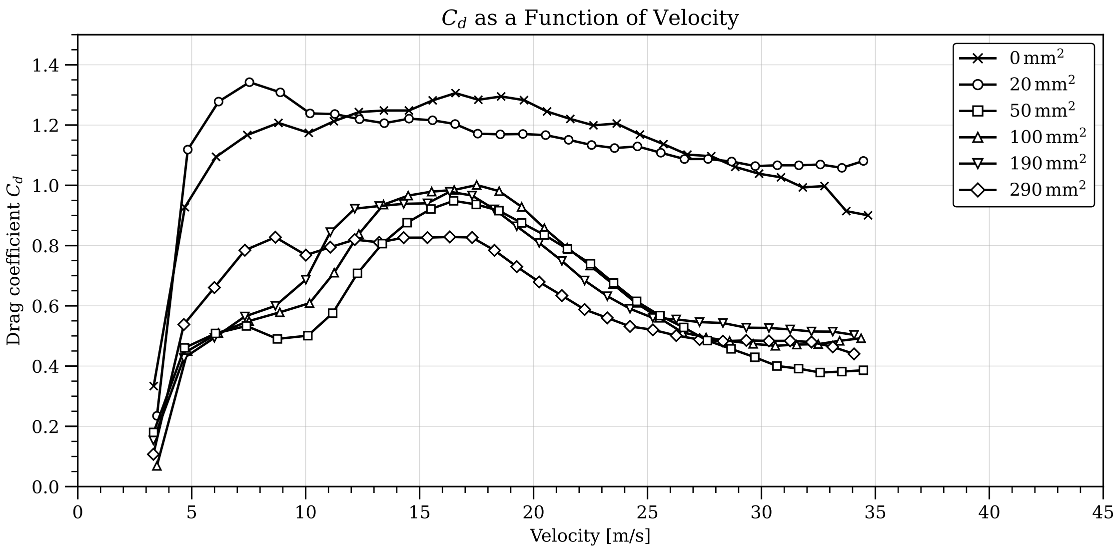

(b) Experimental C_d as a Function of Reynolds number for Contact Wire - *Run 1*

Figure 4.8 Experimental Drag Coefficient Comparisons From Wind Tunnel Experiments (*Run 1*).

When looking at figure 4.8a where experimental data for two different cylinders are examined, it can be seen that the drag coefficient varies greatly between the two cylinders. According to theory, the drag coefficient should, for a given Reynold's number, be the same independent of diameter.

Similarly, 4.8b shows a behavior where the two smallest models (the clean contact wire and the 20 mm^2 ice) have a higher drag coefficient than the models with more accreted ice.

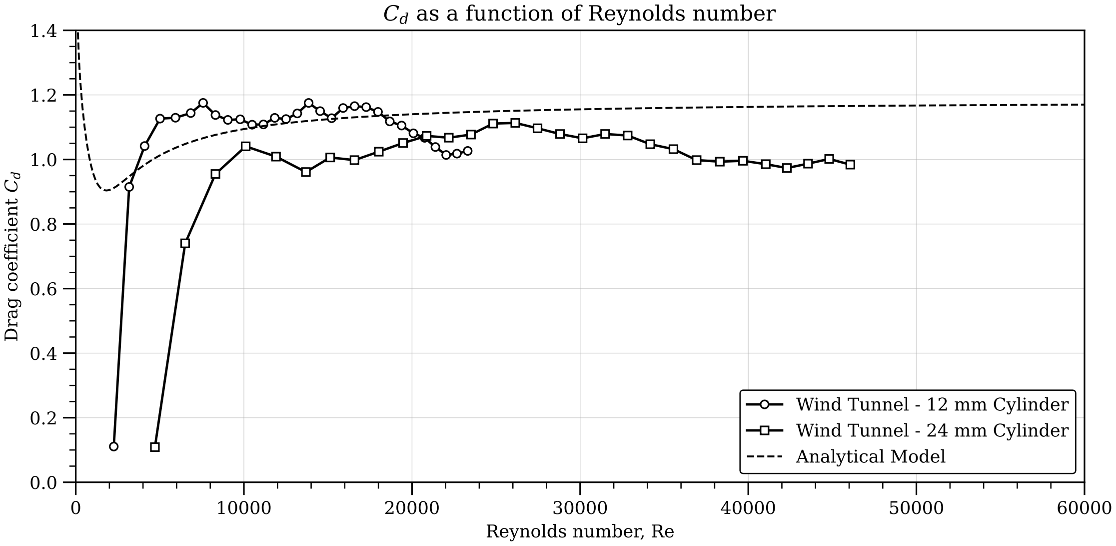

(a) Experimental C_d as a Function of Reynolds number for Cylinders - *Run 2*

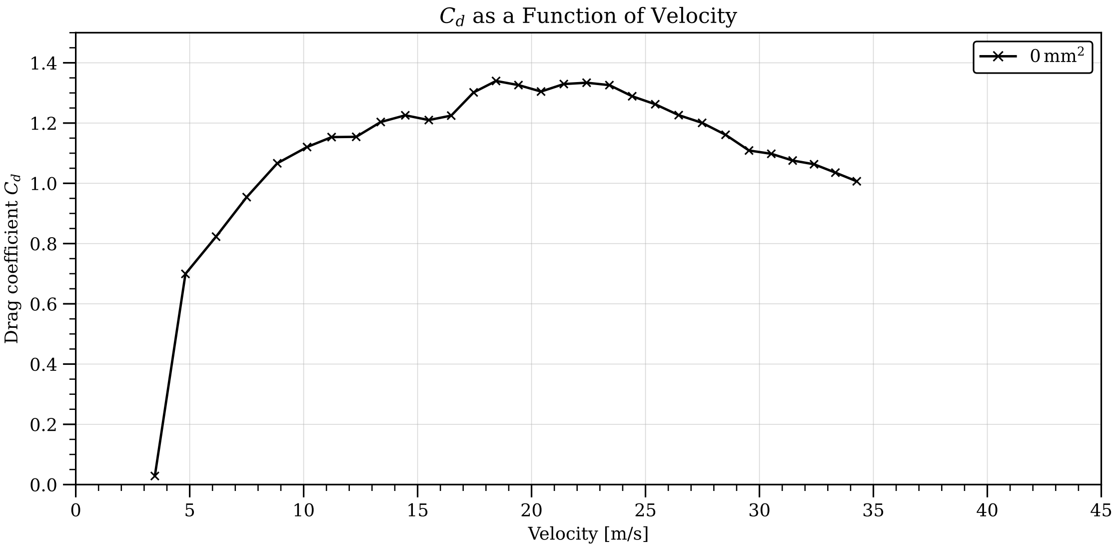

(b) Experimental C_d as a Function of Reynolds number for Contact Wire - *Run 2*

Figure 4.9 Experimental Drag Coefficient Comparisons From Wind Tunnel Experiments (*Run 2*).

For *Run 2* a different behavior for the two cylindrical models can be seen in figure 4.9a. Here the 12 mm cylinder still follows the analytical line like during *Run 1*, but so does the 24 mm cylinder as well, which better corresponds to the theory.

Figure 4.9b then shows the drag coefficient for the clean contact wire during *Run 2*, which differs slightly in shape from corresponding data in *Run 1*.

Simulation validation

In figure 4.10 a comparison between the simulated LES results and the experimental wind tunnel data from *Run 2* is made. Additionally an analytical reference model [37] for the cylinder drag coefficient can be seen.

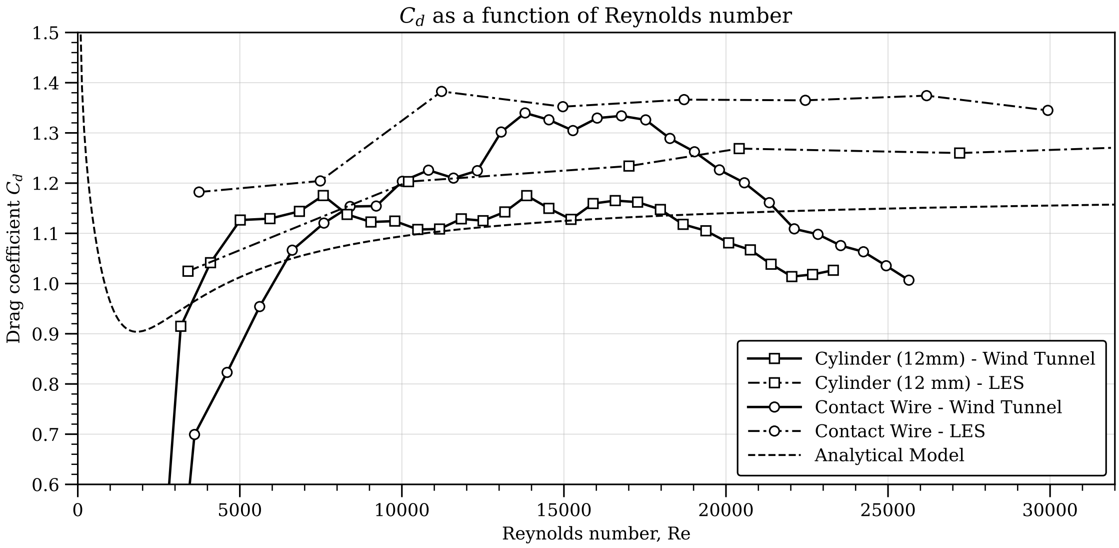

Figure 4.10 Experimental and Simulated C_d as a Function of Velocity for Cylinders and Clean Contact Wires

As can be seen in figure 4.10, the LES simulations, the experimental wind tunnel data, and the analytical model [37] all perform similarly in the range $7500 < Re < 17500$. The clean contact wire can be seen having a greater C_d than the cylinder for both simulations and experimental values for a Reynolds number $Re > 8500$. After $Re = 17500$ the experimental results starts to decline while the simulated values remain somewhat constant.

4.2 Volumetric Approximation

In figure 4.11 the empirical and simulated surfaces can be found for different meteorological parameters relevant for ice accretion. The surfaces are plotted for a temperature span of $-25 < T < 0$ and a wind velocity span of $0 < v < 25$. The relative humidity ϕ is set to 100%. The temperature-velocity area associated with glaze ice according to figure 2.4 is removed from the surfaces. The density is also capped at a lowest value of 200 kg/m^3 in accordance with the standard SS-ISO 12494:2017 [39] (table 2.7).

From figure 4.11 below, it can be seen that the highest ice accretion rate, both for mass and volume, is reached at a high temperature and wind velocity.

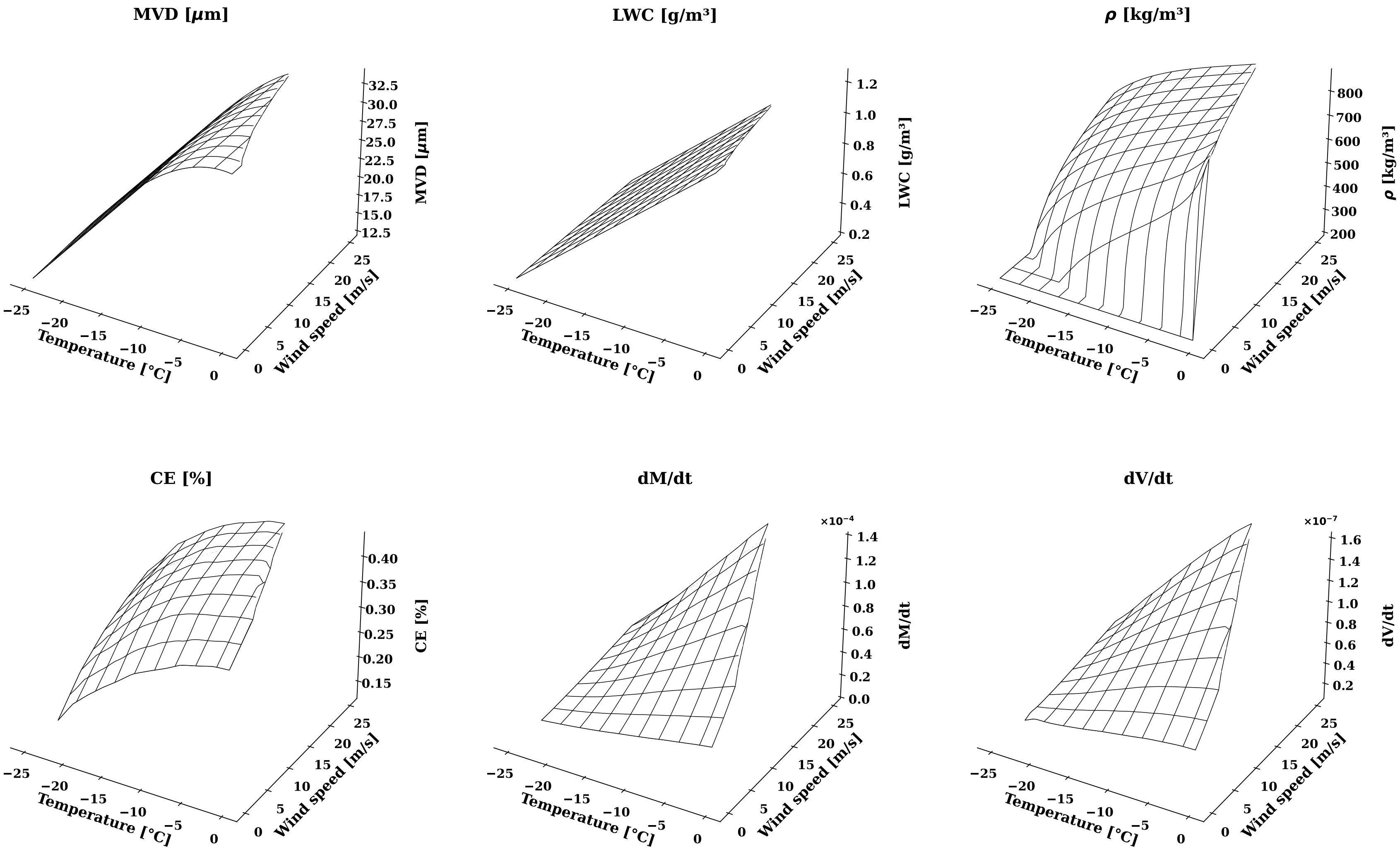

Figure 4.11 Ice Accretion Surfaces

4.3 Load Maps

If a drag coefficient value from figure 4.7 and the wind velocities from figure 3.31 is used, an approximation of the wind-loads, for a certain amount of ice accretion, over Sweden can be created as according to figure 4.12. The figure shows that the wind force, if an equal amount of icing is assumed (100 mm^2) over the whole country, may vary greatly.

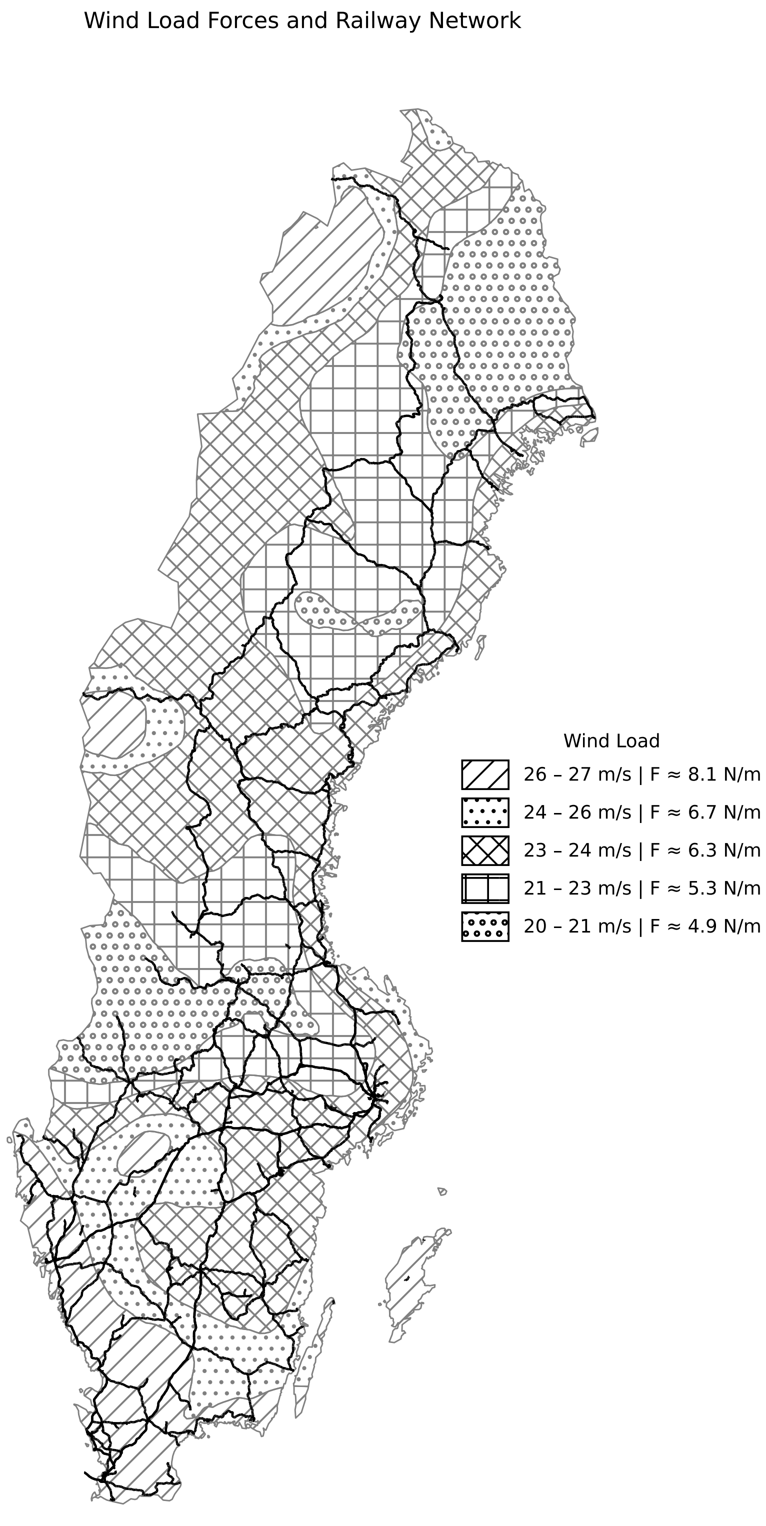

Figure 4.12 Wind Load Map (per meter cable) over Sweden for 100 mm^2 Ice Accretion, a 50 Year Return Period Maximum Wind Speeds. Plotted with the Swedish Railway (Electrified & Non-electrified) as Reference [5], [42].

If the meteorological parameters that affects ice accretion, which have been derived in section 3.9, are varied over time figure 4.13 can be created. Here velocity, temperature and relative humidity values has been set to an arbitrary sinusoidal wave to illustrate the time dependence of the parameters.

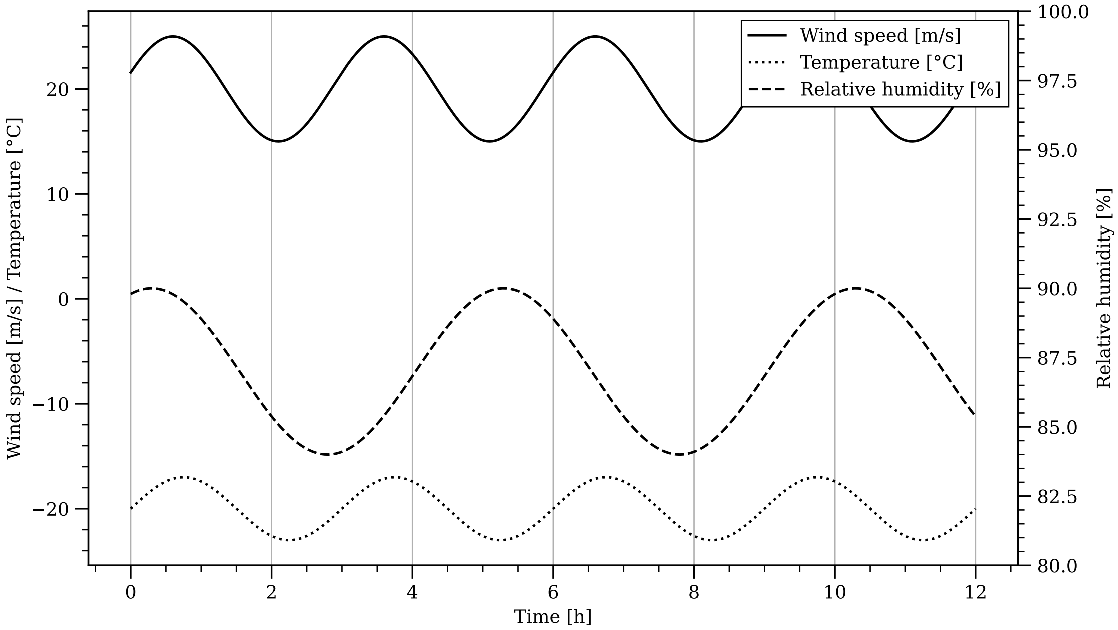

Figure 4.13 Environmental Conditions during Ice Accretion

The parameters in figure 4.13 can then be used to calculate the mass and volume for an icing event, as according to figure 4.14, which uses Makkonen's formula and the density dependency as shown in chapter 3.9. It can be seen that the two resulting metrics have inherited a sinusoidal behavior from the input parameters.

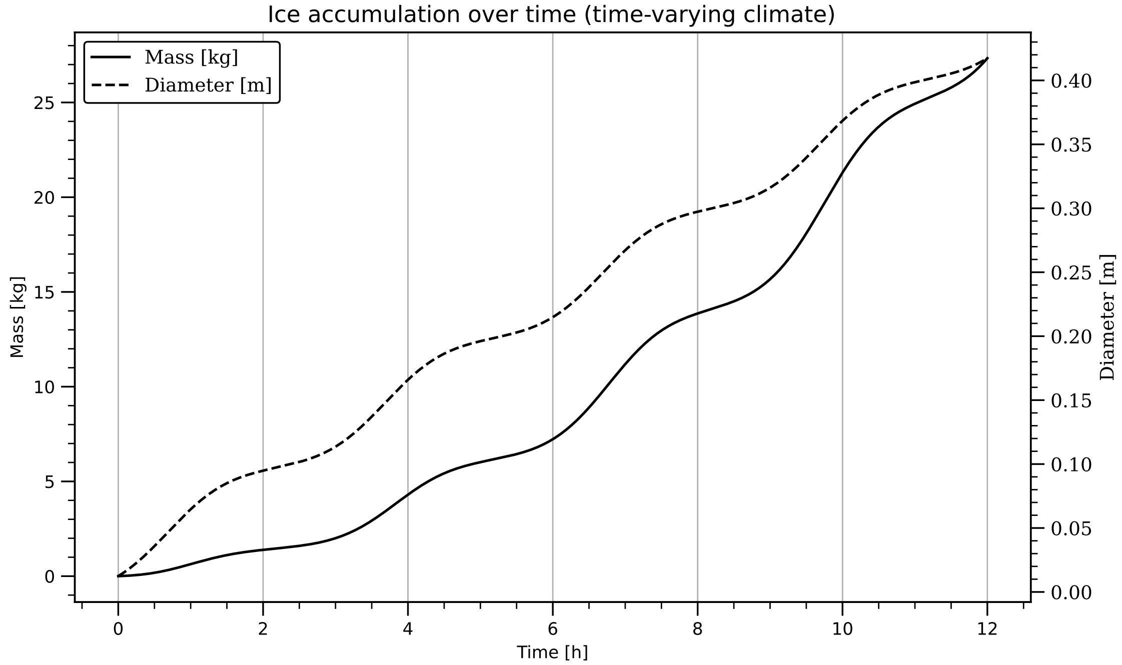

Figure 4.14 Volumetric and Mass accretion

With the values in figure 4.14 together with the C_d-surface (figure 4.7), the forces per meter wire can be calculated as a function of time. This can be seen in figure 4.15. It can be seen that the forces also adopts a sinusoidal behavior, showing that the underlying meteorological values have an impact on the final loads. The total load shown in figure 4.15 is calculated according to equation (4.1), as the wind and ice load forces are assumed to be perpendicular to each other.

$$F_{tot} = \sqrt{{F_{wind}}^2 + {F_{ice}}^2} \tag{4.1}$$

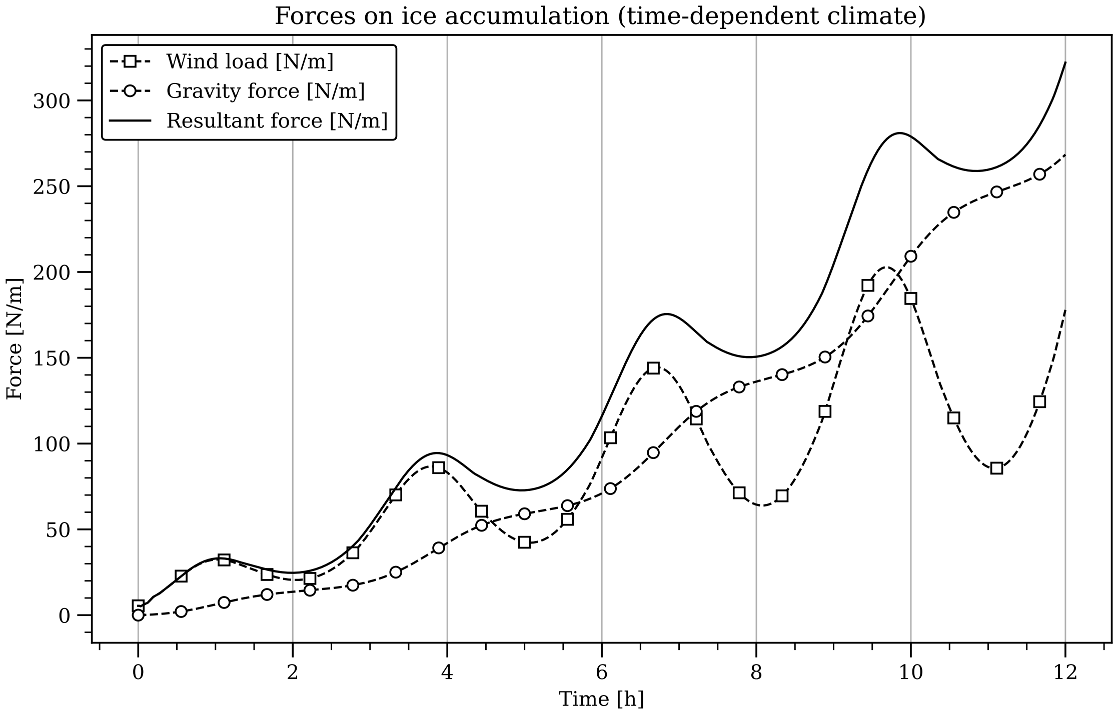

Figure 4.15 Wind Loads and Ice Loads during Ice Accretion

Comparison with current procedures

If the proposed wind and ice load model seen in figure 4.15 is combined with the current proceedings found in chapter 3, using the values found in table 4.3. Figure 4.16 & 4.17 can be created:

Table 4.3 Input parameters for current proceedings in figure 4.16 & 4.17

Input Parameter	Value
Velocity (Constant) [m/s]	25
Temperature (Constant) [$°C$]	258.15
$C_{d,orig}$ [-]	1.0
d_n [m]	0.0132
Terrain Category (TC) [-]	0
h [m]	10

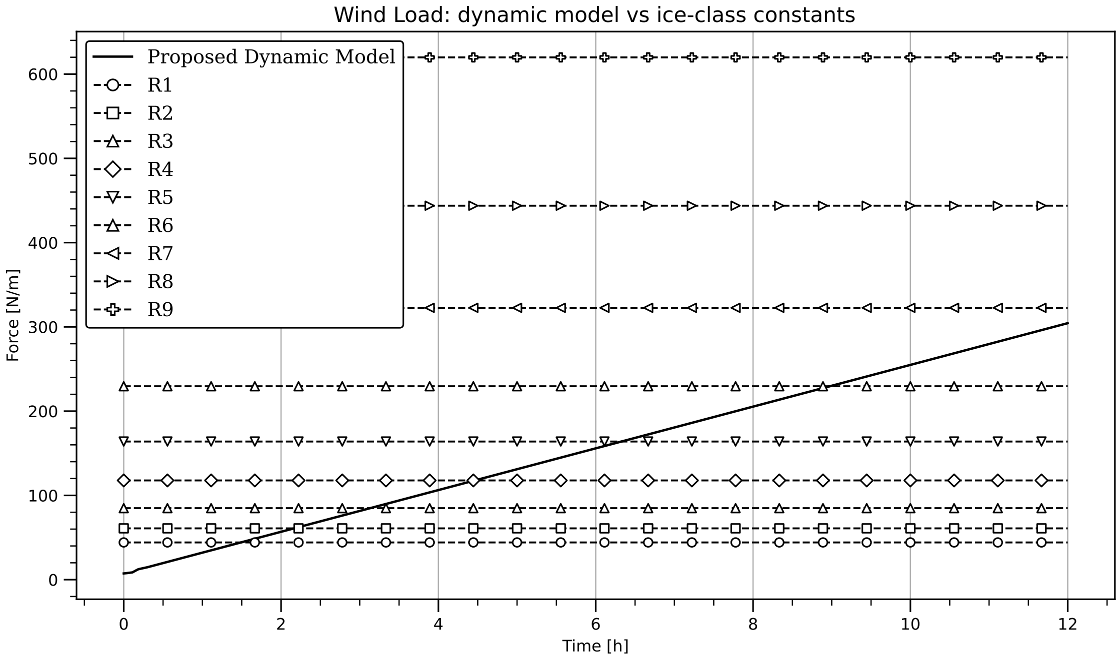

Figure 4.16 Wind Load Comparison - Proposed Dynamic Model vs Current Method

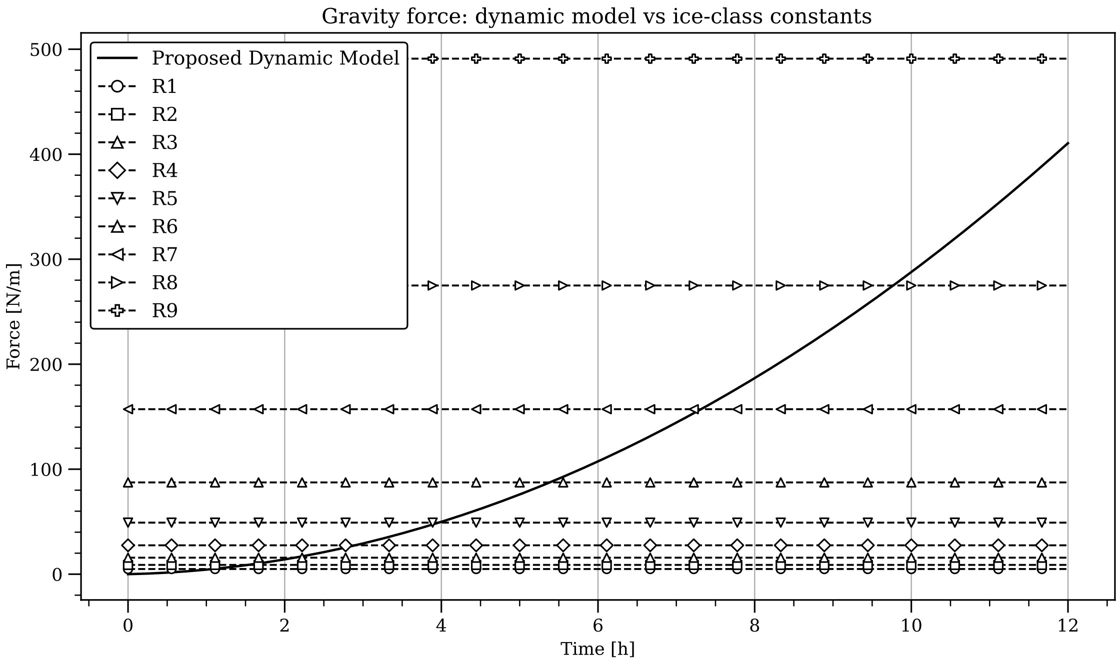

Figure 4.17 Ice Loads Comparison - Proposed Dynamic Model vs Current Method

In both figures it can be seen that the proposed model, depending on the amount of time the ice is allowed to accrete, will intersect multiple ice class loads.

4.4 Additional Surface Roughness Experiments

The results from the experimentally measured surface roughnesses (Ra) and its equivalent sand-grain roughness height (ϵ) according to [1] can be seen in table 4.4. The subscribt denotes in which direction the measurement is taken where x is in the axial direction, and y is along the circumferance of the profile. The presented value is furthermore the mean value of three measurements in the specified direction.

Table 4.4

Object	Ra_x [μm]	Ra_y [μm]	ϵ_x [μm]	ϵ_y [μm]
3D-Printed Model	12.51	1.84	73.35	10.79
Contact Wire	0.79	1.92	4.63	11.26

From tabel 4.4 it can be seen that the 3D-printed sample (and to some degree the contact wire) is highly anisotropic, meaning that the roughness is highly dependent on the direction of measurement. It can also be seen that the surface roughness in the circumferential direction is rather close to $10\mu m$ for the sand-grain roughness for both samples, meaning that the estimated values from Lundkvist [22] was a good prediction if the surface rougness in the flow direction (y) is considered.

Figures 4.18 & 4.19 show the surface captured and processed by the microscope.

In figure 4.18 the characteristic grooves, of a 3D-printed surface, originating from the plastic layers printed by the 3D-printer can be seen. Likewise in figure 4.19 the groves from the extrution process running in the axial direction can be noted.

In the figures 4.20 and 4.21, the measured surface height can be seen for one instace of the axial and circumferential mesurements for each sample.

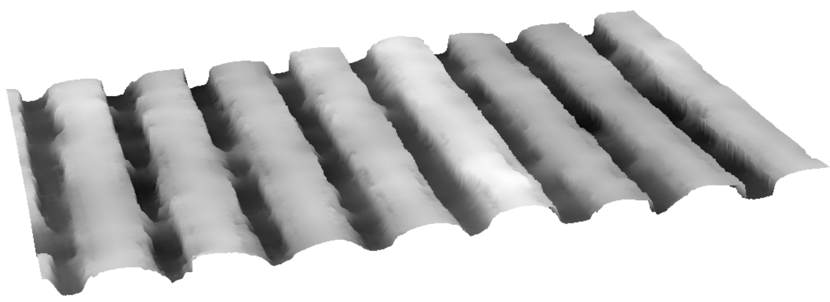

Figure 4.18 3D-printed Surface

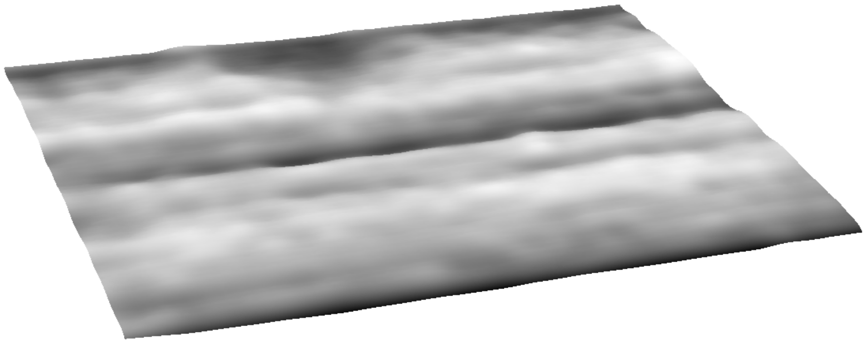

Figure 4.19 Contact Wire Surface

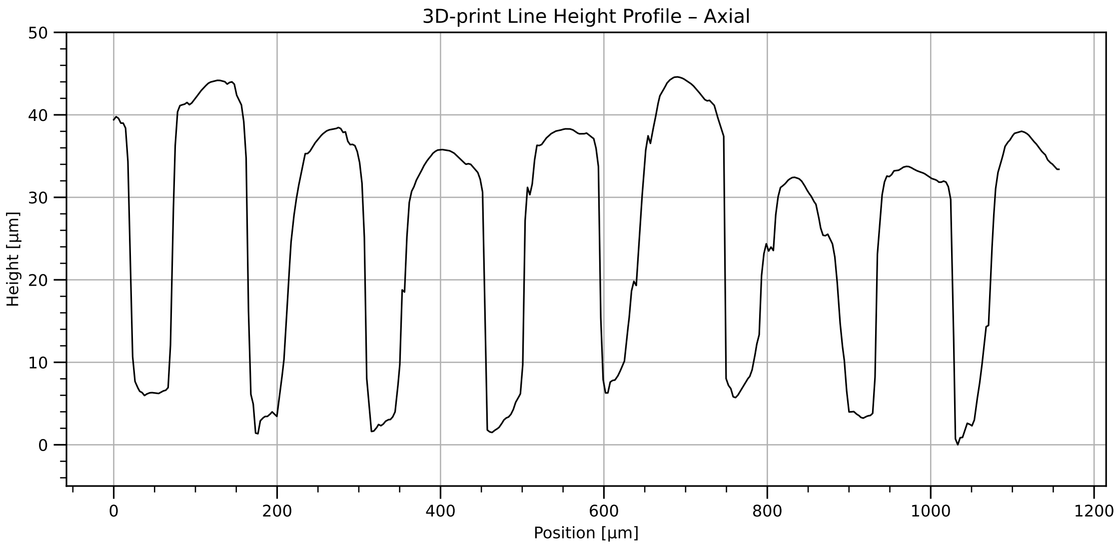

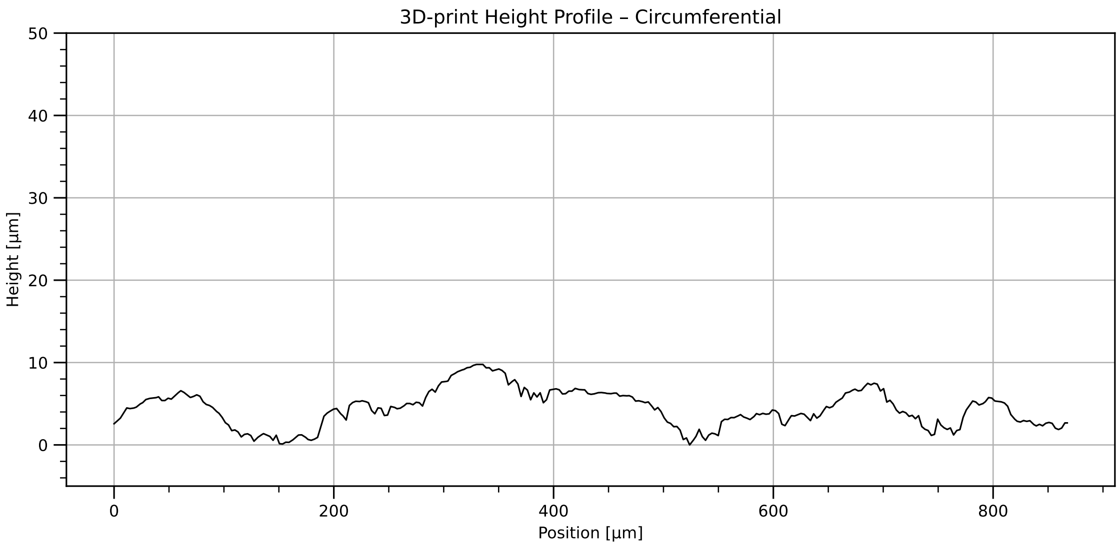

Figure 4.20 Surface Height Measurements from the 3D-printed Profile.

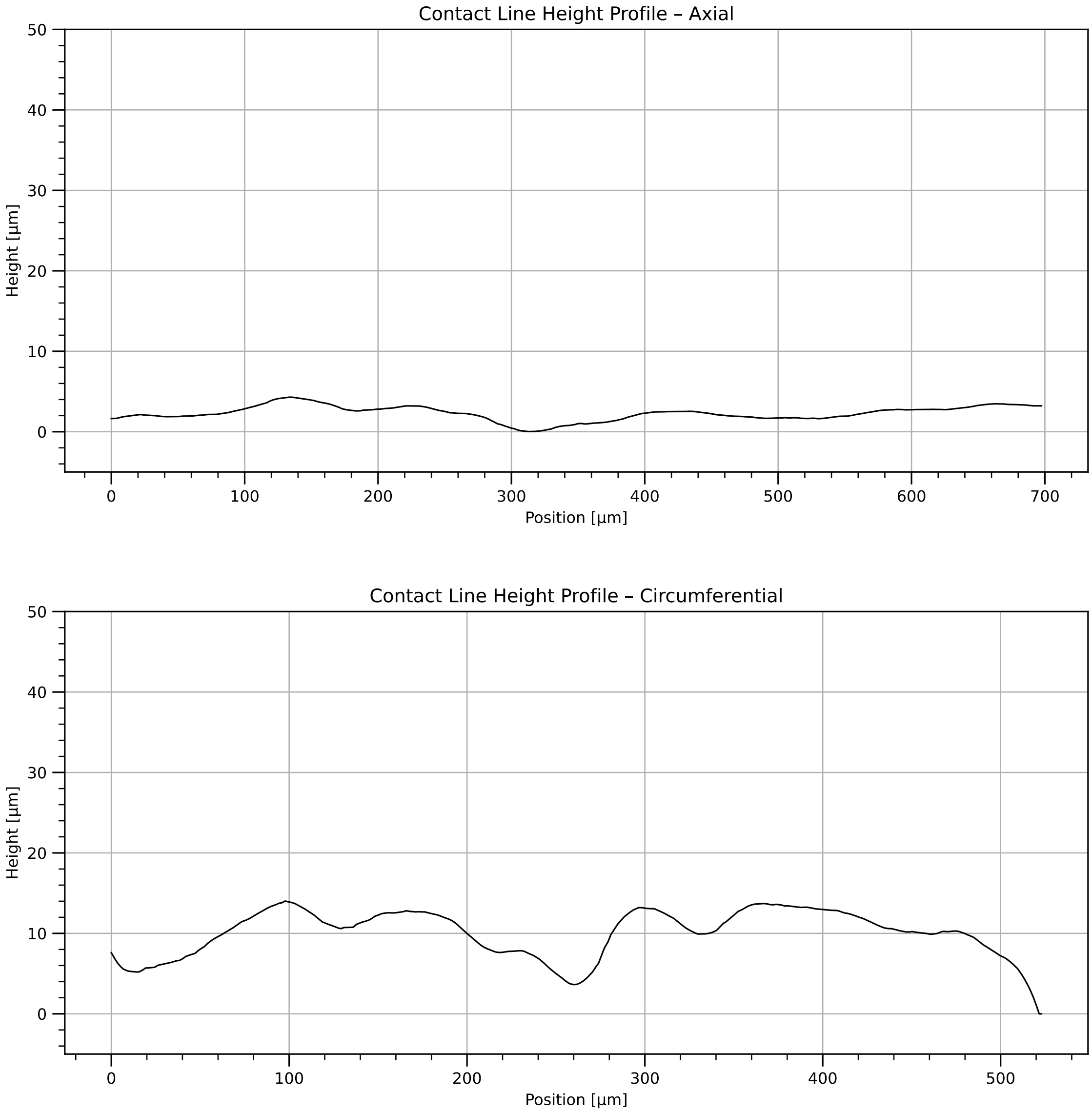

Figure 4.21 Surface Height Measurements from the Contact Wire.

5

Discussion

Methodology

Early in the project, a great deal of effort was put into finding a turbulence model and other settings which would provide an accurate drag coefficient for a cylinder. Some of this initial testing can be found in figures 3.1 to 3.4. Unfortunately a better alternative than a transient simulation with the k-ω-SST turbulence model could not be found. Hence all domain studies was carried out in this manner. Towards the end of the project, settings with LES was found to yield promising results as can be seen in figure 4.10. As a consequence the drag coefficient plots for the iced contact wires had to be re-simulated with LES. The large eddy simulations was then used for all final results, and proposed models. The initial URANS results are still left in the report as they still show the importance of appropriate modeling for accurate results.

Even though URANS was used, it is believed that the domain study still remains accurate. This is largely due to internal comparisons still holding true, even though the absolute values are off. For instance, when C_d stagnates for an increased domain radii in figure 3.7, this radius can still be seen converging the results, even though the result differs from the theoretical value.

Since *FENSAP-ICE* only accepts three dimensional models the chosen domain was extruded to a depth 0.01 meters. This was an arbitrarily picked value that was believed to sufficiently capture the 3D effects. In hindsight however, a depth study to ensure the results were independent from the depth should have been conducted in the same manner as with the domain radius and length.

A delimitation that has yet not been discussed is the assumption that the contact wire, the accreted ice and the ambient air is always at the same temperature. How realistic this assumption is can be debated since the electrical resistance in the contact wire will generate heat. Therefore the temperatures are set to be equal as to represent an event where the train traffic is stopped for a longer period of time. The assumption also fulfills the condition that the surface has to be below zero degrees Celsius for ice to grow. Additionally, an implementation of a heat flux would raise the question of ice melting on the wire surface, and eventual shedding of the accreted ice. While ice shedding is possible to model in *FENSAP-ICE*, it was chosen to be left out of this study.

It is also reasonable to argue that the highest ice loads would occur during weather where train traffic is canceled, as the mechanical forces on the wire during normal train traffic probably would prevent larger amount of accretion to take place.

Drag Coefficient Plots

Simulations

In figure 4.1, where the simulated drag coefficient for cylinders are shown, it can be seen that the resulting drag coefficient values from the LES method agrees with the analytical function better than either one of the URANS simulations. This is most likely the result of URANS not predicting the separation point of the flow accurately enough.

Even though many similar studies chose to use a RANS turbulence model, these results supports the notion that URANS models, for the given domain and mesh, missclaculates the drag forces for a cylindrical object. In contrast, a solution with the LES method results in forces much closer to the expected values and can be trusted to a greater extent. The drag coefficient plots where URANS modeling was applied (figures 4.3a and 4.5a) should therefore not be used in further calculations.

There are some results in the large eddy simulations that are questionable. If one compares the drag coefficients between the extreme icing conditions (figure 4.3b) and the moderate icing conditions (figure 4.5b) it is apparent that the drag coefficient for the cross-sections: 20, 50 and 100 mm^2 differs a lot between the two cases. While the different icing conditions will give rise to a small variation in shape, as proven in figure 3.22, it was not believed it would cause such a large change in drag coefficient for the same amount of accretion. The reason for this variation is still unclear, and should be studied further.

Looking along the area-axis on the C_d-surface in figure 4.7, it can be seen that initially there is a decrease in the drag coefficient followed by an increase until 190 mm^2 where it stagnates. The reason for the initial decrease in drag coefficient probably comes from the cross-section initially becoming more streamlined, without having an increased diameter. But as the diameter increases somewhere after 20-50 mm^2 so does the force.

Beyond the stagnated drag coefficient value of 1.4, after 190 mm^2 is reached, a transition to the drag coefficient associated with a circular cross-section for a given Reynold's number could perhaps be done. This is because large ice accretions tend to even out circularly in the upstream direction. This hypothesis should however be studied in detail before implementation.

The drag coefficients velocity dependence in figure 4.7 is rather unclear and seems to be area-specific. For instance the drag coefficient is rather constant for 290 mm^2 but varies greatly for smaller profiles.

A limitation that should be mentioned is how surface roughness was not accounted for during the LES simulations due to it not being compatible with *ANSYS FLUENT*. Under the theory and methodology sections it was argued that the impact of surface roughness should not be underestimated as the resulting forces might get skewed. Simulations should therefore be carried out where the roughness is modeled in other ways, to draw a conclusion on its effect on contact wires.

Experiments

For the experimental results during *Run 1* in figure 4.8 it is difficult to find a logical explanation to why the drag coefficient for the larger 24 mm cylinder is lower than for the 12 mm cylinder. A drop in C_d below the theoretical value could indicate some form of tip effects are present, but in that case the drag coefficient should be lower for both cylinders. Additionally as the end-plate testing, mentioned in 3.8, and *Run 2* did not show any indications of end effects the drop in the plot would most likely be due to a mistake in the setup. Before *Run 2* a somewhat loose screw was found which is believed to have caused the drop.

Even though the values of the clean wire and the 20 mm^2 iced wire looks promising, which would indicate the fault might have occurred after these two cases, the fact remains that the screw could have loosened anytime during *Run 1* and subsequently all results in figure 4.8b are compromised.

For *Run 2* in figure 4.9a it can be seen that the drag coefficient for the different cylinders now perform according to theory. Hence the results from the clean contact wire in 4.9b should be trusted more than its equivalent in *Run 1*. Unfortunately, due to time constraint, only data for the clean contact wire was gathered.

A recurring trend in all experiments, is that the measured drag coefficient at low velocities is way below the expected value. This can most likely be attributed to the strain gauges being less sensitive at low forces than what the pitot tube is at low velocities. The experimental results at low values should therefore be used with caution.

One further source of error in the experiments is the angle of attack for the mounted model. The aim was to have the AoA as close to 0° as possible, to validate the simulations. However, due to the lack of a proper way to measure the angle during mounting it was difficult to find a way to ensure an AoA of zero degrees, as the models were mounted by eye. But even if the models were placed at a small angle the effects are believed to be small.

Simulation Validation

From figure 4.10 it can be concluded that the large eddy simulations provides values that are compatible with experimental data for both the cylinder and the clean contact wire. The LES also provides greater values for the contact wire than for the cylinder which matches experimental results for $R_e > 8500$, which indicated that the conservative values in figure 4.6 can be trusted.

Figure 4.6, which would be the proposed drag coefficients to be used for dimensioning, shows different C_d values than the approximations used in the current procedure. The drag coefficient for a contact wire used in the current procedure is assumed to be 1.0, but the results show that this approximation may underestimate the forces with up to 40% for a clean wire. Since the current procedure includes safety factors when dimensioning, this underestimation has not led to any known issues. However, if more precise calculations are desired, a value closer to 1.35 or 1.4, taken from the LES, would be more correct as a general conservative value.

If a comparison between the results and the proposed corrected drag coefficients (for rime) in SS-ISO 12494:2017 is made (table 2.6), a discrepancy can be seen, where this study shows that the drag coefficient does not always increase with accreted ice. Instead the wire initially can take on a more streamlined shape, which reduce drag from the original contact wire. The ice classes for rime are however for extremely large ice accretion with a 50 year return period, which will not correspond to smaller accretions where the discussed streamlined behavior is present.

On the same topic, one similarity that can be found is that the corrected drag coefficients for rime, presented in table 2.6, seem to stagnate around 1.6. Even though these corrections are for rime accretion with perpendicular wind, the stagnation is also present in our results but around a value of 1.4 which can be seen in figure 4.7. The difference between the values could indicate that if larger ice accretions were to be studied the resulting drag coefficient value might continue to rise above 1.4. But the difference can also be explained by the perpendicular wind direction which is not studied in this report. For a more detailed conclusion, further investigations are required.

Volumetric Approximation

From figure 4.11 a few things can be noted:

The LWC surface's largest values are extreme, reaching 1.2 g/m^3 for high temperatures. This is most likely a result of the data being collected for aeronautic use, which acts in extreme conditions found in clouds. In-cloud icing can however momentarily reach these values at ground level, which is why it is kept in the calculations. However how common these values are and during what time periods they are present must be studied further.

Additionally for the fitted lines in figure 3.32 & 3.33, the lines represents the envelope of the collected data, so as to encompass all possible values. This in turn results in an extremely conservative fit, even in an aviation context. How well this data is transferred to ground level icing conditions should be considered, but was not possible in the framework of the current study.

The density plot follows the shape presented in current theory well (see figure 2.4), with densities close to the glaze area, having higher values than those closer to the soft rime area.

The collision efficiency surface was simulated for the shown temperatures and wind velocities only for a clean contact wire. In a real scenario as ice accretes the flow field around the object will change, and subsequently the collection efficiency surface will also be altered. The current way of using a static CE-surface for calculating the accretion rate is therefore limited and should be investigated further for other profiles.

Load Maps

The load map over Sweden seen in figure 4.12, gives an image of how the geographical sectioning should be done for dimensioning the railway system. The figure shows how the wind force per meter cable varies over the country with the different maximum wind speeds (with a 50 year return period) that exists. If the railway were to be dimensioned differently across Sweden, this figure gives an understanding of the distribution of the different forces that would have to be taken into account, as the electrified railway spans across all the different sections.

The current load map is generated for 100 mm^2 of accreted ice, this amount is arbitrarily picked, but it could be argued that smaller amounts of ice are more reasonable to be used in a national comparison. This is due to smaller amounts of ice probably being feasible over the whole country, whereas larger amounts of accretion reasonably would be more common in northern parts of the country, alternatively at sites with favorable local conditions. To section the load map more accurately further studies should be made.

In figure 4.15 it can be seen that both the wind load and ice load can be dominating the total load. For more precise calculations using the proposed method, the sinusoidal input data show in figure 4.13 should be exchanged for real time data and meteorological predictions. The strength in this method lies in its ability to, depending on the accuracy of the forecasted weather, make it possible to predict the total load on the contact wires, and foretell an eventual mechanical failure. Alternatively to begin logistical measures to quickly repair prognosticated failures.

When the proposed method is compared to the current proceedings it can be seen that the proposed method intersect many ice classes depending on the considered timescale. Another observation is that the time until the first intersection is rather large. Far exceeding the simulated cross sections in chapter 4.1. This could be a hint towards today's suspicions that the current proceedings may over-dimension the loads for typical icing events, which may be well shorter in time and below the rather conservative values used in figure 4.16 & 4.17.

Recommended Future work

The following section will cover limitations for the presented results and provide additional suggestions for further work in the area.

Contact wire considerations

The study only considers an unused, AC-120 CuETP contact wire, where no material has been worn down. In a realistic scenario the shape of the contact wire will be altered almost immediately as the bottom of the wire will be worn down out due to friction between the wire and the pantograph. This will most likely alter the flow field around the geometry and therefore influence both ice accretion and the subsequent forces.

Another limitation in the study, like many other studies in the field, is that only a pure copper wire was considered, meaning that the impact of identification grooves are neglected. Similarly, only the wire with a nominal size of 120 mm^2 was studied. Since the shape will be identical (if the same clamping grooves and materials are considered) for a smaller cross-section, it can be assumed that the presented results will apply for the smaller sized contact wires as well, only with minor adjustments. This should however be validated before concrete conclusions are drawn. The contact wire, in its actual applications, will also be subjected to other forms of damage and soiling, which may impact its surface roughness. This was also not considered in the study.

The OLE is also a dynamic system. When wind blows on the wire it may give rise to oscillations across the span. While a couple of CFD studies exists on the topic of galloping (wind induced oscillations), to mainly view the amplitude of the oscillations, it might be of interest to study further how this phenomenon can occur at different icing levels and what the effects might be.

Ice accretion estimation

For the estimated ice accretion some decisions could have been made differently. There are however two main changes that can be done on this subject to yield better results.

Firstly, this study only used *single-shot* simulations to estimate the ice accretion in *FENSAP-ICE*. This means that only one flow field around the clean object is simulated and used to determine the collision efficiency and surface roughness which leads to the final ice accretion. In contrast a *multi-shot* simulation, the accretion is simulated iteratively by continuously updating the geometry and mesh together with the flow field, so that the collision efficiency and surface roughness is dependent on the accreted ice for each time step. This better approximates how ice accretes in the real world and therefore would result in a more accurate final geometry. While this is the standard practice in ice simulations in aviation, it was not considered in this study due to time restraints and limited computational resources. An investigation of what impact multi-shot simulations can have on the results is however recommended as future work.

Secondly, as Trafikverket recently has not seen any failures due to combined wind and ice loads on the OCL system no data on where, when or how ice accretes on the actual contact wire exists. Additionally, LWC and MVD are parameters that are harder to measure in comparison to for example the ambient temperature as they require more specialized equipment. All this entales that the current study, where the entirety of Sweden is of interet, very braod assumptions of meteorological parameters, ice accretion time, maximum probable ice etc. has to be made. To solve this problem it would be of interest if companies in the field, like Trafikverket, were to start gathering data of icing events. Lasse Makkonen, a prominent researcher in the field stated that "In many cases, the relevant design load of a structure depends on the combination of extreme ice and extreme wind. It is not possible to estimate the probability of combined ice and wind loads over long periods without data on the recurrence of ice." [24].

Apart from the aforementioned improvements, the dynamic model would also have to incorporate some form of ice shedding mechanism to capture events where the ice is melting or detaching from the surface.

Topography and Geographical Parameters

In reality the wind loads acting on an object will be dependent on where the object is located, and its surrounding terrain. In the current proceedings the wind pressure is dependent on a terrain category according to 2.4. But the wind pressure will also be dependent on the height above ground level and nearby topology which may funnel the air and increase its velocity. All these parameters are not accounted for in the presented method, and should be evaluated before final implementation and usage.

Wind Tunnel

This section aims to aid future users of the wind tunnel in Ljungbyhed, owned and operated by the Lund University department School of Aviation.

The current setup has an angle of attack lever in the test section to attach the observed models to, in addition to the sensor levers. It was found that this lever, even though it is not directly connected to a strain gauge, impacts both the lift and drag sensor readings. Additionally is the pitch lever, which is used to change the AoA by raising or lowering the AoA lever, was both broken and seized in its casing. Due to these problems, the AoA lever was disconnected, which was possible as the small, slender models did not need the extra fixture. In our opinion, if the wind tunnel is to be used again without fixing these problems or disconnecting the lever, it is crucial for the user to find a precise way to measure the AoA externally and to carefully calibrate the effects the AoA lever might have on the sensor readings.

In the study the drag force was calibrated with a pulley mechanisms. While this method was efficient and gave reliable results, an even more precise method would be to measure the output voltages from the strain gauges directly. One can then calibrate the forces from the output values directly without having the connected data logger convert the signals in an unknown way.

Finally, it is our recommendation to invest in a new data logger that is compatible with both modern hardware and software, as the current setup requires an RS-232 port and drivers that are not standard on modern computers. In this case, an old computer with an RS-232 port and Windows 7 installed had to be brought from the university to be able to process the data.

6

Conclusion

The CFD simulations demonstrate how useful CFD can be as a tool for evaluating acting forces on an object, particularly when the geometry of the object influences the flow field in a way that is difficult to predict. In that sense it can be concluded that CFD is a good method to use together with international and national standards in order to further refine various approximations and calculations.

The ice accretion simulations in *FENSAP-ICE* showed a final shape dependency on the used icing parameters. Subsequently, the fluid simulations on the different ice shapes, due to different icing conditions, resulted in different values and trends for the drag coefficients.

Additionally, the resulting fluid simulations showed how the current way of calculating wind loads, for both a clean and iced contact wire, may underestimate the total force with up to 40% due to a low assumed drag coefficient. Moreover, the results showed how the drag coefficient will change with different levels of ice accretion. This means that the assumed constant values in the current way of calculating have to be reevaluated if more precise calculations are desired.

The simulations show a great deal of dependency on the setup where the choice regarding turbulence modeling had the largest impact. LES, in contrast to URANS, proved better predictions of the forces on a cylindrical object. This shows the importance of carefully validating the results, especially when using numerical simulations, as they might depend on a variety of factors.

To validate the forces, this study used a wind tunnel. While the experiments replicated the simulated results to a great extent, it also shows the importance of a complete setup and well calibrated equipment as it can have considerable impact on the final results.

It is believed that the proposed icing model and method works well and is capable of predicting ice accreation and forces. Since no other time dependent ice accretion model exists publicly or at Trafikverket, it can be of guidance during both dimensioning and operation. While the method contains assumptions that should be further evaluated, and neglects other forms of icing, like glaze ice or precipitation icing, it still shows that a dynamic model, if well validated, can achive more precise and geographically dependent results than the current static assumptions.

Finally, even though the model proves its usefulness with the discussed limitations. The most crucial step before an implementation of a dynamic system, is to start gathering in-situ data from observed icing events such as meteorological parameters, ice accreation time and ice loads. This is not only needed to validate the model but also to get a better estimate of what input values the model should use.

Bibliography

[1] T. Adams, C. Grant, and H. Watson. “A Simple Algorithm to Relate Measured Surface Roughness to Equivalent Sand-Grain Roughness”. *International Journal of Mechanical Engineering and Mechatronics* **1**:1 (2012), pp. 66–71. ISSN: 2929-2724. DOI: 10.11159/ijmem.2012.008.

[2] J. Anderson. *Fundamentals of Aerodynamics*. Sixth Edition. McGraw-Hill Education, New York, 2017. ISBN: 978-1-259-12991-9. URL: https://www.academia.edu/105626093/Fundamentals_of_Aerodynamics (visited on 2026-05-12).

[3] ANSYS. *Ansys FENSAP-ICE User Manual*. manual. ANSYS, Inc., 2025.

[4] ANSYS. *Ansys Fluent 2025 R2 Users Guide*. manual. ANSYS, Inc.

[5] Boverket. *API för Klimatdatabas*. Boverket. 2026. URL: https://www.boverket.se/sv/om-boverket/oppna-data/boverkets-klimatdatabas/ (visited on 2026-05-13).

[6] Y. A. Çengel, M. A. Boles, and M. Kanoğlu. *Thermodynamics An Engineering Approach*. Ninth Edition in SI Units. McGraw-Hill Education, 2020. ISBN: 978-1-259-82267-4.

[7] G. Chen, Y. Yang, Y. Yang, and P. Li. “Study on Galloping Oscillation of Iced Catenary System under Cross Winds”. *Shock and Vibration* **2017**:1 (2017). ISSN: 1875-9203. DOI: 10.1155/2017/1634292. URL: https://onlinelibrary.wiley.com/doi/abs/10.1155/2017/1634292 (visited on 2026-04-08).

[8] N. K. Delany and N. E. Sorensen. *Low-Speed Drag of Cylinders of Various Shapes*. 1, 1953. URL: https://ntrs.nasa.gov/citations/19930083675 (visited on 2026-03-23).

[9] FAA Technical Center. *Aircraft Iceing Handbook*. 1. 1991. URL: https://apps.dtic.mil/sti/pdfs/ADA238039.pdf (visited on 2026-04-01).

[10] P. Fu, M. Farzaneh, and G. Bouchard. “Two-Dimensional Modelling of the Ice Accretion Process on Transmission Line Wires and Conductors”. *Cold Regions Science and Technology* **46**:2 (1, 2006), pp. 132–146. ISSN: 0165-232X. DOI: 10.1016/j.coldregions.2006.06.004. URL: https://www.sciencedirect.com/science/article/pii/S0165232X06000723 (visited on 2026-03-23).

[11] R. Gent, N. Dart, and J. Cansdale. “Aircraft Icing”. *Philosophical Transactions of The Royal Society B Biological Sciences* **358** (1, 2000), p. 2873. DOI: 10.1098/rsta.2000.0689.

[12] X. Han, M. Virk, H. Asif, A. Mäkynen, H. Juttula, E. Molkoselkä, and V. A. Kaikkonen. "Atmospheric Icing Meteorological Parameter Study Using Field Experiments and Simulation". *Meteorological Applications* **31**:6 (2024), e70013. ISSN: 1350-4827, 1469-8080. DOI: 10.1002/met.70013. URL: https://rmets.onlinelibrary.wiley.com/doi/10.1002/met.70013 (visited on 2026-05-06).

[13] M. C. Homola, M. S. Virk, T. Wallenius, P. J. Nicklasson, and P. A. Sundsbø. "Effect of Atmospheric Temperature and Droplet Size Variation on Ice Accretion of Wind Turbine Blades". *Journal of Wind Engineering and Industrial Aerodynamics* **98**:12 (2010), pp. 724–729. ISSN: 0167-6105. DOI: 10.1016/j.jweia.2010.06.007. URL: https://www.sciencedirect.com/science/article/pii/S0167610510000693.

[14] "IWAIS 2024 - Proceeding". In: (The Arctic University of Norway). Narvik, Norway. ISBN: 978-82-7823-257-6. URL: https://en.uit.no/Content/854455/cache=20250801122810/IWAIS%202024%20-%20Proceeding.pdf (visited on 2026-03-25).

[15] Z. A. Janjua, B. Turnbull, S. Hibberd, and K.-S. Choi. "Mixed Ice Accretion on Aircraft Wings". *Physics of Fluids* **30**:2 (6, 2018), p. 027101. ISSN: 1070-6631. DOI: 10.1063/1.5007301. URL: https://doi.org/10.1063/1.5007301 (visited on 2026-03-24).

[16] J. Y. Jin and M. S. Virk. "Study of Ice Accretion along Symmetric and Asymmetric Airfoils". *Journal of Wind Engineering and Industrial Aerodynamics* **179** (1, 2018), pp. 240–249. ISSN: 0167-6105. DOI: 10.1016/j.jweia.2018.06.004. URL: https://www.sciencedirect.com/science/article/pii/S0167610518301740 (visited on 2026-03-23).

[17] G. Keenor. *Overhead Line Electrification for Railways*. 6th ed. 2021. URL: http://ocs4rail.com/.

[18] I. Langmuir and K. B. Blodgett. *Mathematical Investigation of Water Droplet Trajectories*. RL-224. 1944–1945.

[19] J. H. Lienhard. *Synopsis of Lift, Drag, and Vortex Frequency Data for Rigid Circular Cylinders*. Bulletin 300. Washington State University, College of Engineering, Research Division, Pullman, Washington, 1966.

[20] C. Liu, Y. Zhang, W. Ma, and Y. Song. "Numerical Simulation and Analysis of the Influencing Factors of Ice Formation on Electrified Railway Contact Lines". *Infrastructures* **10**:5 (2025), p. 121. DOI: 10.3390/infrastructures10050121.

[21] A. Lotfi, M. Virk, and J.-A. Pettersen. "Atmospheric Ice Accretion on Railway Overhead Powerline Conductors-A Numerical Case Study". *The International Journal of Multiphysics* **17** (18, 2023), p. 2023. DOI: 10.21152/1750-9548.17.3.253.

[22] B. Lundkvist. *Ritteknik*. 7th ed. Vol. 2014. Liber AB. ISBN: 978-91-47-01123-0.

[23] L. J. Makkonen and J. R. Stallabrass. *Ice Accretion on Cylinders and Wires*. National Research Council of Canada. Division of Mechanical Engineering, 1984. DOI: 10.4224/40002646.

[24] L. Makkonen. “Models for the Growth of Rime, Glaze, Icicles and Wet Snow on Structures”. *Philosophical Transactions of The Royal Society A: Mathematical, Physical and Engineering Sciences* **358** (15, 2000), pp. 2913–2939. doi: 10.1098/rsta.2000.0690.

[25] L. Makkonen, J. Zhang, T. Karlsson, and M. Tiihonen. “Modelling the Growth of Large Rime Ice Accretions”. *Cold Regions Science and Technology* **151** (1, 2018), pp. 133–137. issn: 0165-232X. doi: 10.1016/j.coldregions.2018.03.014. url: https://www.sciencedirect.com/science/article/pii/S0165232X17304913 (visited on 2026-03-24).

[26] F. Martini, L. Contreras, and A. Ilinca. “Review of Wind Turbine Icing Modelling Approaches”. *Energies* **14** (23, 2021), p. 5207. doi: 10.3390/en14165207.

[27] F. Martini, H. Ibrahim, L. Contreras, P. Rizk, and A. Ilinca. “Turbulence Modeling of Iced Wind Turbine Airfoils”. *Energies* **15** (8, 2022), p. 8325. doi: 10.3390/en15228325.

[28] M. Muhammed, D. Harvey, H. A. Khawaja, M. S. Virk, and G. Momen. “In-Cloud Ice Accretion and Performance Degradation of UAV Propellers in Forward Flight: An Experimental Study”. *Cold Regions Science and Technology* **239** (2025), p. 104599. doi: 10.1016/j.coldregions.2025.104599.

[29] F. W. Murray. “On the Computation of Saturation Vapor Pressure”. *Journal of Applied Meteorology and Climatology* **6**:1 (1, 1967), pp. 203–204. issn: 1520-0450. doi: 10.1175/1520-0450(1967)006<0203:OTCOSV>2.0.CO;2. url: https://journals.ametsoc.org/view/journals/apme/6/1/1520-0450_1967_006_0203_otcosv_2_0_co_2.xml (visited on 2026-03-27).

[30] A. S. Al-Obaidi and G. Madivaanan. “Investigation of the Blockage Correction to Improve the Accuracy of Taylor’s Low-Speed Wind Tunnel”. *Journal of Physics: Conference Series* **2222** (1, 2022), p. 012008. doi: 10.1088/1742-6596/2222/1/012008.

[31] SEK Svensk Elstandard. *Railway applications - Environmental conditions for equipment Part 2: Fixed electrical installations (SS-EN 50125-2)*. Version 1. 24, 2003. url: https://elstandard.se/standard/135701 (visited on 2026-05-05).

[32] SEK Svensk Elstandard. *Railway applications – Fixed installations – Electric traction – Copper and copper alloy grooved contact wires (SS-EN 50149)*. Version 2. 12, 2012. url: https://elstandard.se/standard/1073501 (visited on 2026-05-05).

[33] SEK Svensk Elstandard. *Railway applications – Fixed installations – Electric traction overhead contact lines (SS-EN 50119)*. Version 3. 13, 2020. url: https://elstandard.se/standard/2233101 (visited on 2026-05-06).

[34] J. Shin, B. Berkowitz, H. Chen, and T. Cebeci. “Prediction of Ice Shapes and Their Effect on Airfoil Performance”. In: *29th Aerospace Sciences Meeting*. 29th Aerospace Sciences Meeting. American Institute of Aeronautics and Astronautics, Reno,NV,U.S.A., 7, 1991. doi: 10.2514/6.1991-264. url: https://arc.aiaa.org/doi/10.2514/6.1991-264 (visited on 2026-03-23).

[35] J. Shin and T. H. Bond. “Experimental and Computational Ice Shapes and Resulting Drag Increase for a NACA 0012 Airfoil” (NASA Technical Memorandum 105743 1992).

[36] V. Strouhal. “Ueber Eine Besondere Art Der Tonerregung”. *Annalen der Physik* **241**:10 (1878), pp. 216–251. ISSN: 1521-3889. DOI: 10.1002/andp.18782411005. URL: https://onlinelibrary.wiley.com/doi/abs/10.1002/andp.18782411005 (visited on 2026-04-08).

[37] D. Sucker and H. Brauer. “Fluiddynamik bei quer angeströmten Zylindern”. *Wärme - und Stoffübertragung* **8**:3 (1, 1975), pp. 149–158. ISSN: 1432-1181. DOI: 10.1007/BF01681556. URL: https://doi.org/10.1007/BF01681556 (visited on 2026-04-10).

[38] W. Sutherland. “LII. The Viscosity of Gases and Molecular Force”. *The London, Edinburgh, and Dublin Philosophical Magazine and Journal of Science* **36**:223 (1, 1893), pp. 507–531. ISSN: 1941-5982. DOI: 10.1080/14786449308620508. URL: https://doi.org/10.1080/14786449308620508 (visited on 2026-03-27).

[39] Swedish Stadards Institute. *Atmospheric Icing of Structures (ISO 12494:2017, IDT)*. 2017. URL: https://www.sis.se/produkter/byggnadsmaterial-och-byggnader/eurokoder/isostandarder-for-barverksdimensionering/ss-iso-124942017/ (visited on 2026-03-23).

[40] Swedish Standards Institute. *Eurocode 1 — Actions on structures — Part 1-9: Atmospheric icing (SS-EN 1991-1-9:2025)*. 18, 2025. URL: https://www.sis.se/produkter/byggnadsmaterial-och-byggnader/eurokoder/eurokod-bro/ss-en-1991-1-92025/ (visited on 2026-05-06).

[41] Swedish Standards Institute. *Eurocode 1: Actions on structures – Part 1-4: General actions – Wind actions (SS-EN 1991-1-4:2005)*. URL: https://www.sis.se/produkter/byggnadsmaterial-och-byggnader/byggnadsindustrin/tekniska-aspekter/ssen19911420052/ (visited on 2026-05-06).

[42] Trafikverket. *Lastkajen – Sveriges Väg- Och Järnvägsdata*. Lastkajen. URL: https://lastkajen.trafikverket.se/ (visited on 2026-05-13).

[43] Transportstyrelsen. *Transportstyrelsens föreskrifter och allmänna råd om tillämpning av eurokoder (TSFS 2018:57)*. 12, 2018. URL: https://www.transportstyrelsen.se/sv/om-oss/dina-rattigheter-lagar-och-regler/forfattningssamling/ts-foreskrifter-i-nummerordning/2018/ (visited on 2026-05-17).

[44] H. Versteeg and W. Malalasekera. *An Introduction to Computational Fluid Dynamics*. Second Edition. Vol. 2007. Pearson Education Limited.

[45] F. Xu, D. Li, P. Gao, W. Zang, Z. Duan, and J. Ou. “Numerical Simulation of Two-Dimensional Transmission Line Icing and Analysis of Factors That Influence Icing”. *Journal of Fluids and Structures* **118** (2023), p. 103858. DOI: 10.1016/j.jfluidstructs.2023.103858.

[46] Y. F. Zhang, Y. Song, and Z. G. Liu. “Aerodynamic Characteristics and Galloping Stability of Iced Contact Lines in High-speed Railways: A Computational Fluid Dynamics and Experimental Study”. *Journal of Applied Fluid Mechanics* **19**:4 (5,

2026), pp. 903–919. ISSN: 1735-3572. DOI: 10.47176/jafm.19.4.3864. URL: https://www.jafmonline.net/article_2860.html (visited on 2026-04-08).

A

Extra Results

Velocity	Temperature	Collection Efficiency
5.0	-25.0	0.1192
5.0	-23.0	0.1615
5.0	-21.0	0.1893
5.0	-19.0	0.2139
5.0	-17.0	0.2359
5.0	-15.0	0.2599
5.0	-13.0	0.2746
5.0	-11.0	0.2885
5.0	-9.0	0.3048
5.0	-7.0	0.3123
5.0	-5.0	0.3206
5.0	-3.0	0.3225
10.0	-25.0	0.1811
10.0	-23.0	0.2189
10.0	-21.0	0.2448
10.0	-19.0	0.2748
10.0	-17.0	0.3030
10.0	-15.0	0.3226
10.0	-13.0	0.3431
10.0	-11.0	0.3548
10.0	-3.0	0.3788
10.0	-5.0	0.3745
10.0	-7.0	0.3673
10.0	-9.0	0.3620
15.0	-25.0	0.2223
15.0	-23.0	0.2563
15.0	-21.0	0.2894
15.0	-19.0	0.3182

Velocity	Temperature	Collection Efficiency
15.0	-17.0	0.3434
15.0	-15.0	0.3642
15.0	-13.0	0.3770
15.0	-11.0	0.3885
15.0	-9.0	0.4007
15.0	-7.0	0.4093
15.0	-5.0	0.4157
20.0	-25.0	0.2508
20.0	-23.0	0.2874
20.0	-21.0	0.3205
20.0	-19.0	0.3469
20.0	-17.0	0.3668
20.0	-15.0	0.3890
20.0	-13.0	0.4035
20.0	-11.0	0.4100
20.0	-9.0	0.4211
20.0	-7.0	0.4289
25.0	-25.0	0.2728
25.0	-23.0	0.3052
25.0	-21.0	0.3439
25.0	-19.0	0.3656
25.0	-17.0	0.3876
25.0	-15.0	0.4052
25.0	-13.0	0.4184
25.0	-11.0	0.4271
25.0	-7.0	0.4404
25.0	-9.0	0.4377

Table A.1 Mean Collection Efficiency Sectioned by Temperature and Velocity

Fitted Curves

Table A.2 Linear model parameters and data points

x	$f(x)$
−14.992	0.15435
31.347	1.24478

Model: Linear	
$f(x)$	$0.02353x + 0.50714$
R^2	1.00000

Table A.3 Cubic model parameters and data points

x	$f(x)$
−14.607	11.055
−12.815	12.417
−10.502	14.148
−8.324	15.668
−6.652	16.826
−5.111	17.909
−3.201	19.258
−0.884	20.793
1.765	22.530
4.104	24.066
6.406	25.535
8.184	26.572

x	$f(x)$
9.667	27.426
11.024	28.219
12.152	28.804
14.106	29.895
16.594	31.064
19.261	32.150
21.909	32.940
24.768	33.524
27.548	33.736
30.159	33.809
31.880	33.834

Model: Cubic	
$f(x)$	$-0.00018x^3 - 0.00350x^2 + 0.68439x + 21.40356$
R^2	0.99985

Calibration Results

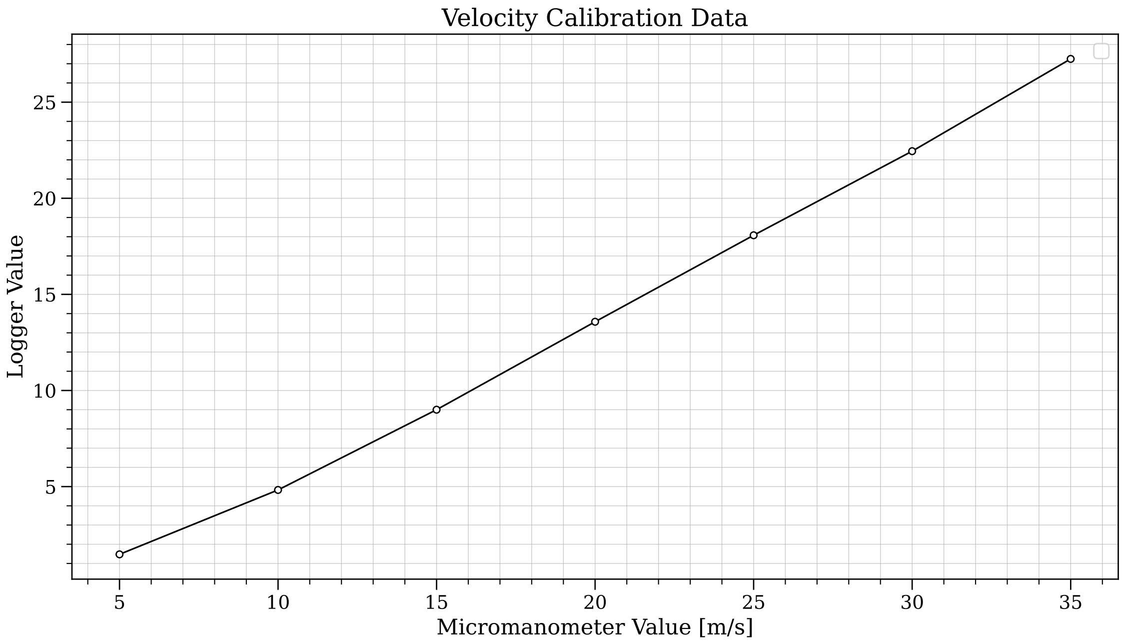

Figure A.1 Wind Tunnel Velocity Calibration

Table A.4 Velocity calibration data

Micromano velocity [m/s]	Logger value [-]
5	1.475
10	4.825
15	9.000
20	13.575
25	18.075
30	22.45
35	27.25

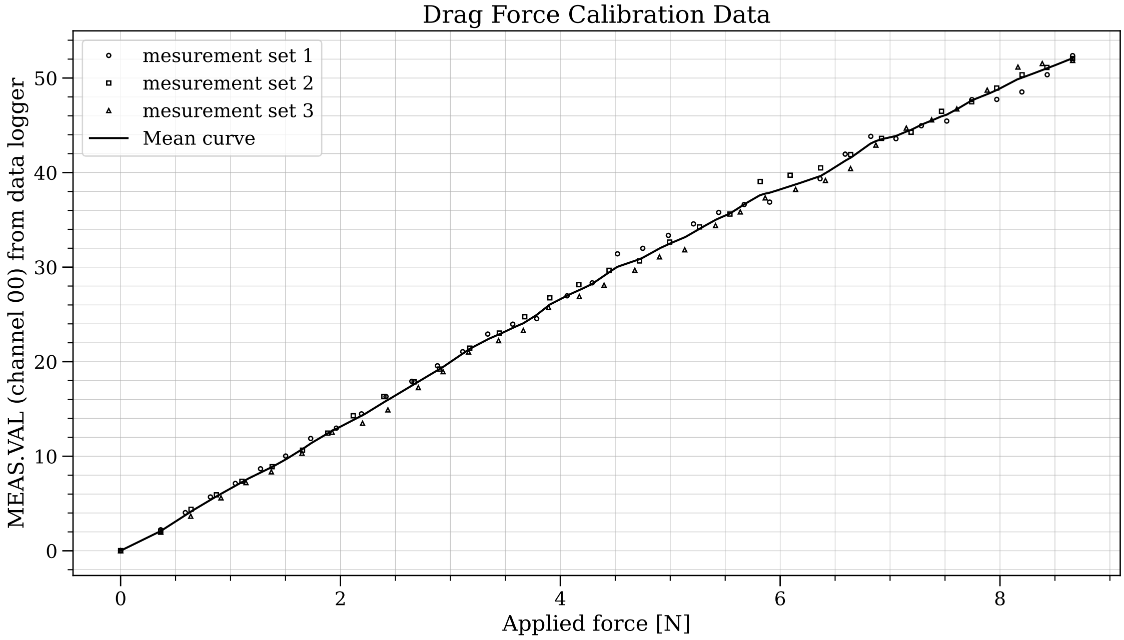

Figure A.2 Wind Tunnel Force Calibration

Table A.5 Binned calibration data (40 bins)

Applied force [N]	Logger value [-]	Applied force [N]	Logger value [-]
1.041×10^{-1}	6.034×10^{-1}	4.434	29.375
3.211×10^{-1}	1.856	4.651	30.565
5.380×10^{-1}	3.396	4.868	31.751
7.550×10^{-1}	4.957	5.085	32.941
9.719×10^{-1}	6.410	5.302	34.287
1.189	7.789	5.519	35.591
1.406	9.054	5.736	37.062
1.623	10.537	5.953	38.058
1.840	12.111	6.170	38.859
2.057	13.465	6.387	39.827
2.274	14.847	6.604	41.329
2.491	16.370	6.821	42.964
2.708	17.884	7.038	43.874
2.924	19.396	7.255	44.878
3.141	21.059	7.472	45.955
3.358	22.445	7.689	47.243
3.575	23.610	7.906	48.404
3.792	25.062	8.123	49.620
4.009	26.669	8.340	50.637
4.226	27.878	8.548	51.572